論文 / 著書情報
Article / Book Information

題目(和文)	Precise measurement of neutrino mixing angle θ13 using the Double Chooz detector
Title(English)	Double Chooz実験におけるニュートリノ混合角θ13の精密測定
著者(和文)	阿部陽介
Author(English)	Yosuke Abe
出典(和文)	学位:博士（理学）, 学位授与機関:東京工業大学, 報告番号:甲第9703号, 授与年月日:2015年3月26日, 学位の種別:課程博士, 審査員:久世　正弘,柴田　利明,陣内　修,中村　隆司,岡　眞
Citation(English)	Degree:, Conferring organization: Tokyo Institute of Technology, Report number:甲第9703号, Conferred date:2015/3/26, Degree Type:Course doctor, Examiner:,,,,
学位種別(和文)	博士論文
Type(English)	Doctoral Thesis

Precise measurement of neutrino mixing angle θ_{13} using the Double Chooz detector

Yosuke Abe

2015

Abstract

A measurement of neutrino mixing angle θ_{13} using the Double Chooz detector is presented in this thesis. θ_{13} is a parameter to describe the mixing of neutrino flavor eigenstates and mass eigenstates. Double Chooz experiment uses nuclear reactors as a neutrino source which is located at Chooz nuclear power plant in France. The neutrino detection is realized by a detector located at 1 km from the reactors. The θ_{13} is measured by a deficit of electron antineutrino at the detector place compared with Monte-Carlo simulation. Double Chooz has been taking data since April 2011, and a result of the measurement with 460 days of live-time is shown in this thesis.

The neutrino signal is detected by inverse beta decay (IBD) reaction: $\bar{\nu_e} + p \rightarrow e^+ + n$. The detection is carried out by observing the two signals of the positron and neutron by the detector filled with gadolinium doped liquid scintillator. The positron signal and the neutron signal are called prompt signal, and delayed signal respectively. The delayed signal happens about 30 μs after the prompt signal due to neutron capture on gadolinium nuclei.

Since most of the neutrino energy is transferred into the prompt event, the neutrino energy can be measured from energy of the prompt signal. In this thesis, not only neutrino rate but also neutrino energy spectrum is used for the measurement of θ_{13}, so the precision of the energy measurement is important. Precise measurement of the neutrino energy is enabled by energy calibration, which is described in detail in this thesis.

Most of background is suppressed by requiring both of the prompt and delayed signals. Remaining backgrounds are cosmogenic background, correlated background, and accidental background. These backgrounds are further reduced by techniques described in this thesis, and their rates and energy spectra are estimated.

The measurement of neutrino mixing angle θ_{13} is carried out by comparing the observed energy spectrum with the Monte-Carlo simulation. Systematic uncertainties due to the detector response, flux prediction, background estimation, and efficiency is included in the analysis. From the 460 days of data, the neutrino mixing angle is measured to be: $\sin^2 2\theta_{13} = 0.105 \pm 0.030$. Thus, evidence of non-zero value θ_{13} is found.

Contents

Chapter 1

Introduction

The research of neutrinos began with studies of nuclear beta decay. Beta decay is a reaction in which a neutron is transformed into a proton with a beta particle that is electron, and a neutrino. In those days when the neutrino had not yet been detected, there was a mystery that it seemed the energy conservation law did not stand for the reaction. The emitted electron was found to have a continuous energy spectrum, on the contrary to the expectation that it should have a constant energy due to the momentum conservation law if the reaction is a two-body decay. In 1930, Wolfgang Pauli argued the continuous spectrum can be explained by postulating, that a particle with no charge and spin 1/2 is emitted by the beta decay [1]. Now the particle is called neutrino (or more precisely, anti-electron neutrino).

In 1956, neutrinos were first observed in the experiment led by Clyde L. Cowan and Frederick Reines [2]. In the experiment, a nuclear reactor was used as the neutrino source. The products from inverse beta decay:

$$\bar{\nu_e} + p \rightarrow e^+ + n \tag{1.1}$$

were used for observing the neutrinos. The neutrino detector consisted of target tanks and scintillation detectors. The target tank was filled with Cadmium doped water. A positron annhilates with electron in the water and emits gamma rays. After about 3 μsec, neutron is absorbed by the Cadmium and then gamma rays are emitted. Gamma rays are then turned into scintillation light in the scintillation detector. The photons are observed with the equipped photomultiplier tubes (PMTs). From the result, cross section for reaction in Eq. (1.1) 1 of $6.3 \times 10^{-44}\mathrm{cm}^2$ was measured, which was within 5 % agreement with their prediction. After the discovery of electron neutrino [2] as mentioned above, muon neutrino was discovered in 1962 [3], and tau neutrino was discovered in 2000 [4].

In 1989, the number of neutrino flavors was measured to be 3 by the CERN Large Electron Positron collider (LEP) [5]. In the experiment, Z to $\nu_\alpha \bar{\nu_\alpha}$ contributions to the Z decay width was measured. The result was consistent with three neutrino flavors.

In the Standard Model, neutrino mass is assumed to be zero. However, the discovery of neutrino oscillation led to a conclusion that neutrinos have mass.

In this thesis, precise measurement of neutrino mixing angle θ_{13} in Double Chooz is described. The analysis is carried out by using 460.67 live days of data which is about twice as much as the data in the publication in 2012 [6]. Also, the analysis contains several methods newly developed, which are aimed to improve such as background reduction and precision improvement of energy reconstruction. Since Double Chooz uses the shape of the neutrino energy spectrum, so the precision of energy is important for the θ_{13} measurement. Author of this thesis developed the energy calibration techniques, and the method contributed to improve the sensitivity of the θ_{13} measurement.

This thesis consists of chapters, the contents are below:

Chapter 2 Neutrino oscillation as well as experiments to understand the neutrino oscillation are explained.

Chapter 3 This Chapter describes about the Double Chooz detector, how to measure neutrinos from reactors, and the data acquisition system.

Chapter 4 Output from the data acquisition system must be reconstructed to suitable information for the neutrino oscillation analysis. Three reconstruction methods: pulse reconstruction, vertex reconstruction, and muon reconstruction are described.

Chapter 5 This chapter describes about calibration systems, which are used for energy estimation of neutrino signals.

Chapter 6 Calibration methods for precise measurement of neutrino signals are described.

Chapter 7 Neutrino oscillation analysis is carried out by comparing the measured data with Monte-Carlo simulation. This chapter describes how to estimate neutrino signals in the Double Chooz detector.

Chapter 8 This chapter explains about how to discriminate neutrino signals from background signals.

Chapter 9 Efficiency of the neutrino measurement is estimated.

Chapter 10 Backgrounds rates and energy spectra are estimated.

Chapter 11 This chapter describes about the neutrino oscillation analysis, and neutrino mixing angle θ_{13} is estimated.

Chapter 12 Conclusion of this thesis.

Chapter 2

Neutrino oscillation

Periodical neutrino flavor transition is predicted from neutrino oscillation. It happens as a result of non-zero mass of neutrinos and the mixing between flavor eigenstates and mass eigenstates of neutrinos. Neutrino mixing is characterized by three parameters called neutrino mixing angles which take a role as associating the three flavor eigenstates with the three mass eigenstates as written below [7].

$$\begin{pmatrix} \nu_e \\ \nu_\mu \\ \nu_\tau \end{pmatrix} = U_{PMNS} \begin{pmatrix} \nu_1 \\ \nu_2 \\ \nu_3 \end{pmatrix} \tag{2.1}$$

$$\begin{aligned} U_{PMNS} &= \begin{pmatrix} 1 & 0 & 0 \\ 0 & c_{23} & s_{23} \\ 0 & -s_{23} & c_{23} \end{pmatrix} \begin{pmatrix} c_{13} & 0 & s_{13}e^{-i\delta} \\ 0 & 1 & 0 \\ -s_{13}e^{i\delta} & 0 & c_{13} \end{pmatrix} \begin{pmatrix} c_{12} & s_{12} & 0 \\ -s_{12} & c_{12} & 0 \\ 0 & 0 & 1 \end{pmatrix} \\ &= \begin{pmatrix} c_{12}c_{13} & s_{12}c_{13} & s_{13}e^{-i\delta} \\ -s_{13}c_{23} - c_{12}s_{13}s_{23}e^{i\delta} & c_{12}c_{23} - s_{12}s_{13}s_{23}e^{i\delta} & c_{13}s_{23} \\ s_{12}s_{23} - c_{12}s_{13}c_{23}e^{i\delta} & -c_{12}s_{23} - s_{12}s_{13}c_{23}e^{i\delta} & c_{13}c_{23} \end{pmatrix} \end{aligned} \tag{2.2}$$

The matrix is called Pontecorvo-Maki-Nakagawa-Sakata (PMNS) matrix. Here, ν_e, ν_μ and ν_τ are the flavor eigenstates and ν_1, ν_2 and ν_3 are the mass eigenstates. s_{ij} and c_{ij} mean $\sin\theta_{ij}$ and $\cos\theta_{ij}$ respectively and θ_{ij} is neutrino mixing angle between mass eigenstates i and j. δ is a phase complex. δ has non-zero value if CP symmetry is violated in neutrino sector.

Wave function of neutrino flavor transition with respect to time is described as below:

$$\nu_\alpha(t) = \sum_i U_{\alpha i}\nu_i e^{-iE_i t/\hbar}, \tag{2.3}$$

where, α and i represent the flavor and mass eigenstate, respectively. Travel speed of neutrinos is almost speed of light, so the probability is represented with respect to the

travel distance L,

$$\nu_\alpha(L) = \sum_i U_{\alpha i}\nu_i e^{-iE_iL/c\hbar}. \tag{2.4}$$

From this, probability of the transition from ν_α to ν_β is written by:

$$P\left(\nu_\alpha \to \nu_\beta\right) = \sum_i \sum_j U_{\alpha i}U^*_{\beta i}U^*_{\alpha j}U_{\beta j}e^{-i(E_i-E_j)L/c\hbar}. \tag{2.5}$$

Double Chooz measures a deficit of electron antineutrino, characterized by a survival probability of electron antineutrino. The survival probability $P\left(\nu_e \to \nu_e\right)$ is calculated as the following equation:

$$\begin{aligned} P\left(\nu_e \to \nu_e\right) &= \left|\left(\sum_i U_{ei}e^{-iE_iL/c\hbar}U^*_{ie}\right)\right|^2 \\ &= c_{13}^4c_{12}^4 + c_{13}^4s_{12}^4 + s_{13}^4 + 2c_{13}^4c_{12}^2s_{12}^2\cos\left(\frac{E_1-E_2}{c\hbar}L\right) \\ &\quad + 2c_{13}^2c_{12}^2s_{13}^2\cos\left(\frac{E_1-E_3}{c\hbar}L\right) + 2c_{13}^2s_{12}^2s_{13}^2\cos\left(\frac{E_2-E_3}{c\hbar}L\right) \end{aligned} \tag{2.6}$$

Here, difference of the energy $E_i - E_j$ is approximated by:

$$\begin{aligned} E_i - E_j &= \sqrt{p^2c^2 + m_i^2c^4} - \sqrt{p^2c^2 + m_j^2c^4} \\ &\approx pc + \frac{m_i^2c^4}{2pc} - pc - \frac{m_j^2c^4}{2pc} = \frac{\left(m_i^2 - m_j^2\right)c^4}{2E} \end{aligned} \tag{2.7}$$

Therefore,

$$\begin{aligned} P\left(\nu_e \to \nu_e\right) &= c_{13}^4c_{12}^4 + c_{13}^4s_{12}^4 + s_{13}^4 + 2c_{13}^4c_{12}^2s_{12}^2\cos\left(\frac{m_1^2-m_2^2}{2E\hbar}c^3L\right) \\ &\quad + 2c_{13}^2c_{12}^2s_{13}^2\cos\left(\frac{m_1^2-m_3^2}{2E\hbar}c^3L\right) + 2c_{13}^2s_{12}^2s_{13}^2\cos\left(\frac{m_2^2-m_3^2}{2E\hbar}c^3L\right) \end{aligned} \tag{2.8}$$

In the equation, substituting a term like:

$$\begin{aligned} \cos\left(\frac{m_i^2-m_j^2}{2E\hbar}c^3L\right) &= 1 - 2\sin^2\left(\frac{m_i^2-m_j^2}{4E\hbar}c^3L\right) \\ &= 1 - 2\sin^2\Delta_{ij} \end{aligned} \tag{2.9}$$

where

$$\Delta_{ij} \equiv \frac{\Delta m_{ij}^2}{4E\hbar}c^3L = \frac{m_i^2-m_j^2}{4E\hbar}c^3L \tag{2.10}$$

and

$$s_{ij}^2c_{ij}^2 = \frac{\sin^2(2\theta_{ij})}{4}, \tag{2.11}$$

In Eq. (2.10), $\Delta m^2_{ij} = m^2_i - m^2_j$. Then, the equation becomes:

$$P(\nu_e \to \nu_e) = 1 - c^4_{13}\sin^2(2\theta_{12})\sin^2\Delta_{12} - c^2_{12}\sin^2(2\theta_{13})\sin^2\Delta_{13} - s^2_{12}\sin^2(2\theta_{13})\sin^2\Delta_{23}. \tag{2.12}$$

Currently, measured values of Δm^2_{ij} are [8]:

$$\Delta m^2_{21} = (7.53 \pm 0.18) \times 10^{-5}\ \text{eV}^2$$
$$\Delta m^2_{32} = (2.44 \pm 0.06) \times 10^{-3}\ \text{eV}^2\ \text{(normal mass hierarchy)}$$
$$\Delta m^2_{32} = (2.52 \pm 0.07) \times 10^{-3}\ \text{eV}^2\ \text{(inverted mass hierarchy)}$$

The normal mass hierarchy means the order of mass for the mass eigenstates is $m_1 < m_2 < m_3$, while the inverted mass hierarchy means $m_3 < m_1 < m_2$. Whether the mass hierarchy is normal or inverted is not yet known.

When the distance is short enough, the survival probability $P(\nu_e \to \nu_e)$ can be approximated. Using the parameters measured in the past: $\Delta_{12} \sim 0.05$ and $\Delta_{23} = \Delta_{13} - \Delta_{12} \sim \Delta_{13}$, the survival probability $P(\nu_e \to \nu_e)$ can be written by:

$$P(\bar{\nu_e} \to \bar{\nu_e}) = 1 - \sin^2(2\theta_{13})\sin^2\left(1.267 \times \frac{\Delta m^2_{31}[\text{eV}^2] \times L[\text{m}]}{E[\text{MeV}]}\right) + O\left(10^{-3}\right). \tag{2.13}$$

2.1 Experiments to observe neutrino oscillation

Observations of neutrino oscillation were made using several neutrino sources. Firstly in late 1960s, Ray Davis et al. observed a deficit of solar neutrino flux with respect to the standard solar model prediction [9]. This deficit had not long been explained, and it was known as the solar neutrino problem. In 1998, the evidence of neutrino oscillation was presented from observation of atmospheric neutrino by Super Kamiokande experiment [10].

Beam neutrinos produced by accelerators are also used for the measurement of the neutrino oscillation.

Nuclear reactor is also a good source of neutrinos. Electron antineutrinos are produced by the beta decay in the nuclear chain reaction. The Double Chooz experiment uses nuclear reactors for the precise measurement of neutrino oscillation.

In this section, the history of experiments to measure the oscillation is described.

2.1.1 Solar neutrino experiments

The indication of the neutrino oscillation is first obtained from experiments to measure solar neutrinos. The neutrino flux from the sun is calculated by the standard solar model

(SSM) [11]. Most of the neutrinos are produced by *pp* (proton-proton) chain reaction and Carbon-Nitrogen-Oxygen (CNO) cycle. These are the reactions from which hydrogen is converted into helium. The *pp* reaction is the most dominant reaction to produce energy in the Sun, by which hydrogen is converted into helinum. The most dominant chain reactions is:

- $\mathrm{p} + \mathrm{p} \rightarrow {}^{2}\mathrm{H} + \mathrm{e}^{+} + \nu_{\mathrm{e}}$
- ${}^{2}\mathrm{He} + \mathrm{p} \rightarrow {}^{3}\mathrm{He} + \mathrm{e}^{+}\gamma$
- ${}^{3}\mathrm{He} + {}^{3}\mathrm{He} \rightarrow {}^{4}\mathrm{He} + 2\mathrm{p}$

The CNO cycle is a sequence of reactions. Typically the reaction consists of the following reactions:

- ${}^{12}\mathrm{C} + {}^{1}\mathrm{H} \rightarrow {}^{13}\mathrm{N} + \gamma$
- ${}^{13}\mathrm{N} \rightarrow {}^{13}\mathrm{C} + \mathrm{e}^{+} + \nu_{\mathrm{e}}$
- ${}^{13}\mathrm{C} + {}^{1}\mathrm{H} \rightarrow {}^{14}\mathrm{N} + \gamma$
- ${}^{14}\mathrm{N} + {}^{1}\mathrm{H} \rightarrow {}^{15}\mathrm{O} + \gamma$
- ${}^{15}\mathrm{N} + {}^{1}\mathrm{H} \rightarrow {}^{12}\mathrm{C} + {}^{4}\mathrm{He}$

The energy of neutrinos by these reactions are shown in Figure 2.1.

As mentioned before, the first experiment which succeeded to observe the solar neutrino is Homestake experiment in South Dakota, USA in the 1960s [13]. In the experiment, neutrinos are detected using radiochemical reaction:

$$\nu_{\mathrm{e}} + {}^{37}\mathrm{Cl} \rightarrow {}^{37}\mathrm{Ar} + \mathrm{e}^{-} \tag{2.14}$$

Energy threshold for this reaction is 814 keV. Neutrinos from pp chain reaction above the threshold energy are observed. In the experiment, neutrinos are successfully observed. However, measured neutrino capture rate was 2.56 ± 0.16 SNU, and the SSM prediction was 9.3 ± 1.3 SNU [13] [1]. Therefore, the number of observed neutrinos was only about 30 % for the prediction by the SSM. The deficit was known as "solar neutrino problem". Similar experiments (SAGE [14], GALLEX [15], and GNO [16]) were carried out which use $\nu_e + {}^{71}\mathrm{Ga} \rightarrow \mathrm{e}^{-} + {}^{71}\mathrm{Ge}$ reaction, and approximately 50 % of neutrinos of the SSM were observed from these experiments (for example, SAGE observed 79 SNU (solar neutrino units), at 90 % C.L. while the prediction is 132 SNU).

The Super Kamiokande experiment [17] also measured energy spectrum of solar neutrino originating from reactions of ${}^{8}\mathrm{B}$. The Super Kamiokande detector consists of a large

[1] SNU is a unit, which corresponds to the neutrino flux producing 10^{-36} captures per target atom per second

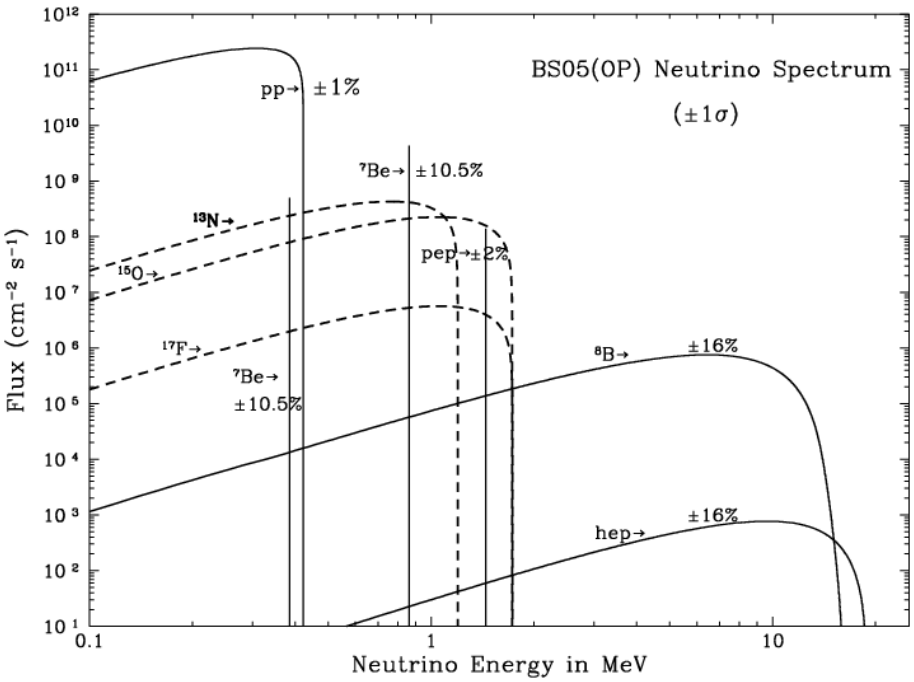

Figure 2.1: Solar neutrino energy spectrum. BS05(OP) is a solar model. [12]

cylinder filled with 50 kiloton of purified water. On the wall of the detector, 11,146 of 50 cm diameter photomultiplier tubes are attached to observe water Čherenkov light by neutrino reactions. The neutrinos are detected via elastic scattering interaction which is expressed by the following formula:

$$\nu_x + e^- \rightarrow \nu_x + e^- \tag{2.15}$$

The observed neutrino flux, as well as the SSM prediction are:

$$\Phi_{\text{obs}} = 2.35 \pm 0.02(\text{stat}) \pm 0.08(\text{syst}) \times 10^6 \text{ cm}^{-2}\text{sec}^{-1} \tag{2.16}$$

$$\Phi_{\text{pred}} = 5.82 \left(1.00^{+0.23}_{-0.23}\right) \times 10^6 \text{ cm}^{-2}\text{sec}^{-1} \tag{2.17}$$

Thus, large discrepancy between the SSM prediction and observation is ascertained.

Sudbury Neutrino Observatory (SNO) experiment measured the neutrino flux [18]. In 2002, the result is published which confirmed the evidence of the neutrino oscillation. SNO experiment also observes Čherenkov light. The detector consists of 12m diameter spherical transparent acrylic vessel filled with pure heavy water. The Čherenkov light signal is detected by 9,500 photomultiplier tubes surrounding the vessel. The SNO experiment was capable to detect three types of signals generated via charged current, neutral current,

and elastic scattering reaction as written below respectively:

$$\nu_{\rm e} + {\rm d} \rightarrow {\rm e}^- + {\rm p} + {\rm p} \quad \text{(charged current)} \tag{2.18}$$

$$\nu_{\rm x} + {\rm d} \rightarrow {\rm p} + {\rm n} + \nu_{\rm x} \quad \text{(neutral current)} \tag{2.19}$$

$$\nu_{\rm x} + {\rm e}^- \rightarrow \nu_{\rm x} + {\rm e}^- \quad \text{(elastic scattering)} \tag{2.20}$$

The charged current interaction is only for electron neutrinos, while the neutral current and elastic scattering interactions are sensitive to all kinds of neutrinos: $\nu_{\rm e}$, ν_μ, and ν_τ. Occurrence of neutral current interaction is same for all kinds of neutrinos, however, the occurrence of elastic scattering interaction is larger for electron neutrinos than the other types. The flux for each reaction is shown in Figure 2.2, and measured to be:

$$\Phi_{\rm CC} = \left(1.76^{0.06}_{-0.05}({\rm stat})^{+0.09}_{-0.09}({\rm syst})\right) \times 10^6 {\rm cm}^{-2}{\rm s}^{-1} \tag{2.21}$$

$$\Phi_{\rm NC} = \left(5.09^{+0.44}_{-0.43}({\rm stat})^{+0.46}_{-0.43}({\rm syst})\right) \times 10^6 {\rm cm}^{-2}{\rm s}^{-1} \tag{2.22}$$

$$\Phi_{\rm ES} = \left(2.39^{+0.24}_{-0.23}({\rm stat})^{+0.12}_{-0.12}({\rm syst})\right) \times 10^6 {\rm cm}^{-2}{\rm s}^{-1} \tag{2.23}$$

This is transformed to number of estimated flux of $\nu_{\rm e}$ and ν_μ and/or ν_τ:

$$\Phi_{\rm e} = 1.76^{+0.05}_{-0.05}({\rm stat})^{+0.09}_{-0.09}({\rm syst}) \times 10^6 \ {\rm cm}^{-2}{\rm s}^{-1} \tag{2.24}$$

$$\Phi_\mu + \Phi_\tau = 3.41^{+0.45}_{-0.45}({\rm stat})^{+0.48}_{-0.45}({\rm syst}) \times 10^6 \ {\rm cm}^{-2}{\rm s}^{-1}. \tag{2.25}$$

Thus, non-zero flux of ν_μ and/or ν_τ is observed, and it indicates that neutrino flavor is transformed at more than 5σ level.

2.1.2 Atmospheric neutrino experiments

Pions and kaons are produced from interactions of primary cosmic rays (protons and nuclei) with nuclei in the atmosphere, and neutrinos are produced as decay products. The primary decay mode of a pion is written below, with probability of 99.9 %.

$$\pi^+ \rightarrow \mu^+ + \nu_\mu \tag{2.26}$$

$$\pi^- \rightarrow \mu^- + \bar{\nu_\mu} \tag{2.27}$$

In addition, the produced muon decays to produce neutrinos:

$$\mu^+ \rightarrow {\rm e}^+ + \nu_{\rm e} + \bar{\nu_\mu} \tag{2.28}$$

$$\mu^- \rightarrow e^- + \bar{\nu_e} + \nu_\mu \tag{2.29}$$

Atmospheric neutrinos below a few GeV are coming from these reactions. Therefore, about one third of the atmospheric neutrinos are expected to be $\nu_{\rm e}$ or $\bar{\nu_{\rm e}}$, and two thirds are ν_μ or $\bar{\nu_\mu}$. However, high energy muons have effectively longer lifetime, therefore arrive

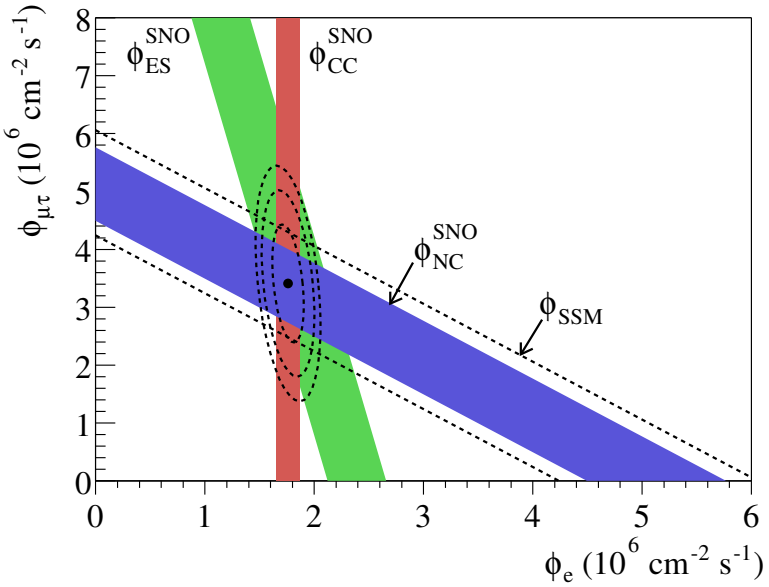

Figure 2.2: Flux of ^{8}B solar neutrinos. The X-axis is the flux of electron flavor, and the Y-axis is μ or τ flavor. The three bands are the measurements of the CC, ES, and NC rates with one standard deviations. [18]

at the earth's ground. It makes the fraction of muon neutrino flux larger at high energy above a few GeV.

Atmospheric neutrinos are observed by experiments such as Kamiokande [19], MACRO [20], and IMB [21] in 1990s. The Kamiokande and IMB experiment used water Čherenkov to detect the neutrinos, while the MACRO experiment used scintillator counters to detect energy distribution of neutrinos. These experiments indicated the neutrino oscillation.

In 1998, Super Kamiokande experiment [10] observed the first evidence of neutrino oscillation (the detector is explained in section 2.1.1). In the experiment, zenith angle distribution of the electron-like and muon-like neutrinos are measured. Since the range of neutrinos coming from just overhead and from beneath the ground are different, it is possible to measure the fraction of neutrino flavor transitions with respect to the distance by the measurement of the zenith angle distribution. The measured result is shown in Figure 2.3. In the figure, the measured data as well as Monte-Carlo prediction with no oscillation and the best fit with neutrino oscillation are shown. It is clearly seen that the deficit of muon-neutrino-like signals between the data and no oscillation model. From the best fit, the parameters Δm^2 and $\sin^2 2\theta$ are measured at 90 % confidence level:

$$\sin^2 2\theta > 0.82 \tag{2.30}$$

$$5 \times 10^{-4} < \Delta m^2 < 6 \times 10^{-3} \text{ eV}^2 \tag{2.31}$$

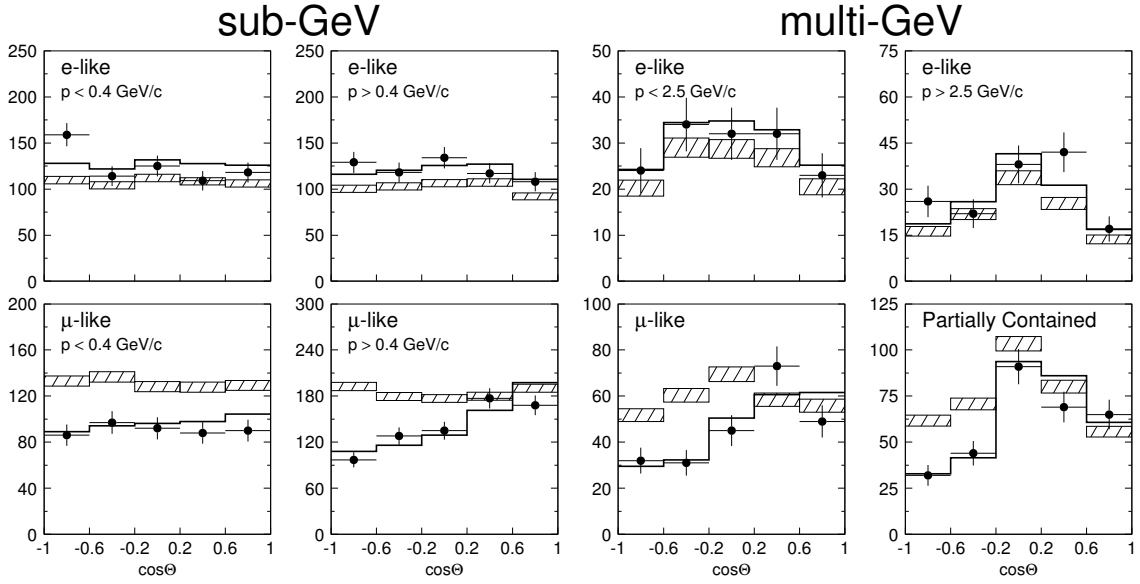

Figure 2.3: Zenith angle distribution of electron-neutrino-like events and muon-neutrino-like events [10]. The events are divided into sub-GeV ($E_{\rm vis} < 1330$MeV) and multi-GeV ($\mathrm{E_{vis}} > 1330$ MeV) regions (for historical reason connected with proton decay search). The Θ stands for the zenith angle. The events are divided with respect to momentum p. For the sub-GeV region is shown with $p < 400$ MeV/c and $p > 400$ GeV/c, while for the multi-GeV region is shown with $p < 2.5$ GeV/c and $p > 2.5$ GeV. When $\cos\Theta < 0$, the neutrinos are upward going while when $\cos\Theta > 0$, the neutrinos are downward going. The black points are measured data, and the hatched region indicates the Monte-Carlo prediction with no neutrino oscillation scenario, and the bold line is the best fit including neutrino oscillation.

2.1.3 Accelerator neutrino experiments

Measurement of neutrino oscillation can be carried out by using neutrinos produced by accelerators. Muon neutrinos are generated by pion decay which is produced when accelerated protons hit on a target:

$$\pi^+ \to \mu^+ + \nu_\mu \tag{2.32}$$

The K2K experiment [22] is one of the accelerator neutrino experiments in Japan, which first observed the neutrino oscillation by measuring the accelerator neutrinos. In the experiment, an accelerator at KEK shoots neutrino beam toward the detector at Kamioka. The neutrinos are generated by 12 GeV proton beam, and the energies of neutrinos are between few hundreds MeV to few GeV. The detector is the Super Kamiokande detector which is 250 km far from the accelerator. In addition, detectors including water Čherenkov detector are built at a distance of 300 m from the target to measure the neutrino flux before the transition happens. They observed that the deficit of ν_μ flux by the Super Kamiokande in comparison with the flux measured at short distance. From the result, the null oscillation assumption is excluded by 4.3σ.

The Main Injector Neutrino Oscillation Search (MINOS) experiment [23] is the long baseline neutrino experiment which measures the ν_μ generated by the accelerator in Fermilab, USA. By the accelerator, neutrinos with energy of 1 GeV to 5 GeV are produced. Two detectors are used in the experiment. They are at 1 km and 735 km from the accelerator, and called near detector and far detector respectively. Both of the detectors are steel and scintillator tracking calorimeters. The far detector was 5400 tons, and the near detector was 980 tons. The neutrino oscillation is confirmed from a deficit of muon neutrinos. In the experiment, ν_μ disappearance is observed at the far detector. The measured values of neutrino oscillation parameters are:

$$|\Delta m^2_{32}| = 2.39^{+0.09}_{-0.10} \times 10^{-3}\ \mathrm{eV}^2 \tag{2.33}$$

$$\sin^2(2\theta_{23}) = 0.957^{+0.035}_{-0.036} \tag{2.34}$$

Moreover, several accelerator neutrino experiments are running currently. Tōkai to Kamioka (T2K) experiment [24] observes neutrinos at the Super Kamiokande detector which is 295 km far from the neutrino facility, J-PARC at Tōkai-mura, Japan. The experiment also measures the θ_{13}. In the analysis, ν_e like events are compared with the predictions. From the experiment, 28 electron-like events were observed. If normal hierarchy is assumed, the measured value of θ_{13} was:

$$\sin^2 2\theta_{13} = 0.140^{+0.038}_{-0.032} \tag{2.35}$$

If inverted hierarchy is assumed,

$$\sin^2 2\theta_{13} = 0.170^{+0.045}_{-0.037} \tag{2.36}$$

In this analysis, $\delta_{\mathrm{CP}} = 0$, $\sin^2 2\theta_{23} = 1$ and $\Delta m^2_{32} = 2.4 \times 10^{-3}\mathrm{eV}^2$ are assumed.

2.1.4 Reactor neutrino experiment

Nuclear reactor produces electron antineutrinos in the reactor core via beta decay of nuclear fission products. The details of the neutrino production in reactors will be explained in section 7.1.

All reactor neutrino experiments use inverse beta decay to observe neutrinos. By the inverse beta decay reaction, a positron and neutron are emitted. Neutrinos can be measured by detecting signals from those emitted particles.

In 1997, the CHOOZ experiment [25] started to measure the reactor neutrinos from nuclear power plant located in Chooz, France. There are two reactors in the power plant. The detector was filled with gadolinium doped liquid scintillator, and placed at 1 km from the reactors. Gadolinium was doped for neutron detection, since neutrons are captured on gadolinium nuclei and emit total 8 MeV gamma rays which is well above the gammas from natural radioactivities and therefore easily distinguished. The positron and gamma rays are detected by the liquid scintillator and photo-multiplier tubes attached inside the detector. The experiment measured the deficit of electron antineutrino flux. Only an upper limit to θ_{13} was obtained by the CHOOZ experiment as:

$$\sin^2 2\theta_{13} < 0.15 \text{ at } \left|\Delta m^2_{32}\right| = 2.5 \times 10^{-3} \text{ eV}^2 \tag{2.37}$$

Currently, experiments based on similar idea to the CHOOZ experiment are running for measuring the θ_{13}: Double Chooz, Daya Bay [26], and RENO [27]. Uncertainty on the neutrino flux estimation was relatively large with the CHOOZ experiment, so these three experiments designed to construct multiple detectors for reduction of the neutrino flux uncertainty. Double Chooz is designed to construct two detectors, one (near detector) is located at 400 m from the reactors, and the other one is located at 1 km from the reactors. The effect of the neutrino oscillation is negligible at the near detector, so the deficit at the far detector is measured in comparison of the measurements by the two detectors. The first result was published in March 2012 [28], which is $\sin^2 2\theta_{13} = 0.086 \pm 0.041(stat) \pm 0.030(syst)$. From the result, non-zero θ_{13} was indicated. The data taking started in April 2011 only with the far detector. The Daya Bay experiment is running at the Daya Bay nuclear complex which is located in China. There are six reactors, and six detectors. Three detectors are near detectors located at 350 m to 500 m from the reactors, and the other three detectors are the far detectors located at 1500 m to 1900 m from the reactors. The experiment started in December 2011. They published the first result of neutrino mixing angle measurement as: $\sin^2 2\theta_{13} = 0.092 \pm 0.016(stat) \pm 0.005(syst)$ in 2012. The precision is improved in the latest publication as $\sin^2 2\theta_{13} = 0.090^{+0.008}_{-0.009}$ published in October 2014 [29].

RENO (Reactor Experiment for Neutrino Oscillation) is also the reactor neutrino experiment, which is located at Yonggwang Nuclear Power Plant in Korea. Six reactors, and two detectors are used. Average distance between the reactors and the near detector

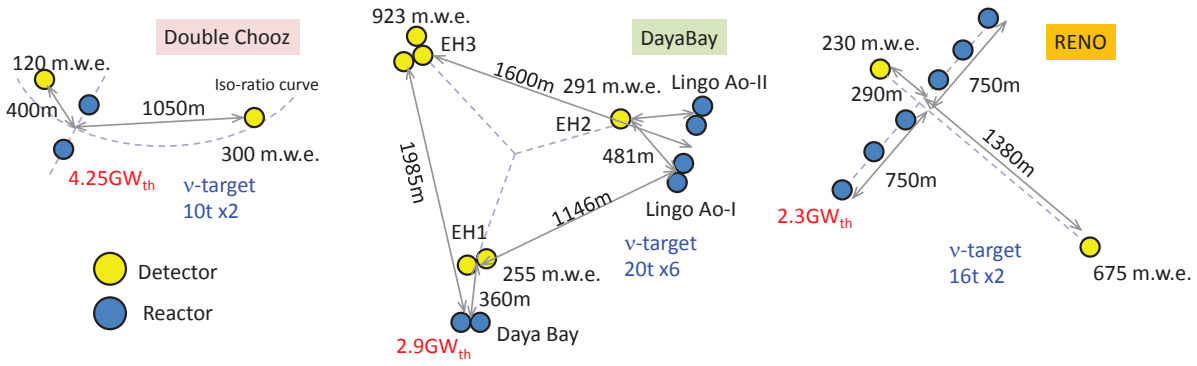

Figure 2.4: Layout of reactors and detectors for Double Chooz, Daya Bay, and RENO experiments.

is 294 m, while it is 1383 m between the reactors and the far detector. The experiment started in August 2011, and published the first result in May 2012. The result is $\sin^2 2\theta_{13} = 0.113 \pm 0.013(stat) \pm 0.019(syst)$.

The layouts of the reactors and detectors for these experiments are shown in figure 2.4.

2.2 Summary of current measurements and future prospect on neutrino oscillation

In this section, summary of the current measurements about neutrinos, what is measured and what is not measured, and future prospect is described. At the end, we will show why it is important to measure θ_{13} in Double Chooz for the understanding of neutrinos, and physics.

From the solar, atmospheric, accelerator, and reactor neutrino experiments, the existence of the neutrino flavor and mass eigenstates mixing in a three flavor framework was revealed. The mixing is characterized as three mixing angles, and one phase δ, and mass differences between their mass eigenstates. From the measurement of neutrino oscillation, neutrinos are found to have finite mass, otherwise, the neutrino oscillation cannot happen. However, absolute mass of each mass eigenstate has not been measured because of their small values. Only their mass differences are measured. The parameters are summarized in table 2.1 [8].

Still, there are unknown properties in the property of neutrinos. For example, following questions are remaining:

- Neutrino mass hierarchy problem: The problem is that ordering of neutrino masses is not determined. Namely, it is not known that if $m_1 < m_3$ (normal hierarchy) or

Table 2.1: Parameters related with neutrino oscillation [8].

Parameter	Value
$\sin^2 2\theta_{12}$	0.846 ± 0.021
Δm^2_{21}	$(7.53 \pm 0.18) \times 10^{-5}$ eV^2
$\sin^2 2\theta_{23}$	$0.999^{+0.001}_{-0.0018}$ (normal mass hierarchy)
$\sin^2 2\theta_{23}$	$1.000^{+0.000}_{-0.017}$ (inverted mass hierarchy)
Δm^2_{32}	$(2.44 \pm 0.06) \times 10^{-3}$ eV^2 (normal mass hierarchy)
Δm^2_{32}	$(2.52 \pm 0.07) \times 10^{-3}$ eV^2 (inverted mass hierarchy)
$\sin^2 2\theta_{13}$	$(9.3 \pm 0.8) \times 10^{-2}$

$m_1 > m_3$ (inverted mass hierarchy).

- Octant of θ_{23} determination: It is a question whether the θ_{23} is larger or smaller than $\pi/4$.
- Measurement of CP violation phase $\delta_{\rm CP}$.
- Whether neutrinos are Dirac or Majorana particle.

Sensitivities to the mass hierarchy determination, and other parameters such as CP violating phase depend on the mixing angles including θ_{13}. Therefore, precise measurement of θ_{13} is important for further understanding of the neutrino nature by future experiments.

Here, we will show the impact of θ_{13} to the neutrino research. For the measurement of $\delta_{\rm CP}$, precise measurement of θ_{13} is important. There are several experiments to measure θ_{13} using reactor neutrinos and accelerator neutrinos. Benefit of the reactor neutrino experiments is that precise measurement of θ_{13} is possible, since it is not affected by the uncertainties from other neutrino oscillation parameters. On the other hand, accelerator based experiments such as the NOvA [30] and Hyper-Kamiokande [31] are sensitive not only to θ_{13}, but also the other parameters such as δ, θ_{23} octant, and mass hierarchy. Therefore, accelerator based experiments and reactor neutrino experiments are complementary to each other. Figures 2.5, 2.6, and 2.7 show allowed regions of $\sin^2 2\theta_{13}$ and $\delta_{\rm CP}$, assuming $\sin^2 2\theta_{13} = 0.08$ and $\delta_{\rm CP} = \pi/2$, for the neutrino beam experiment, reactor experiment, and combined result respectively [32]. Thus, it is beneficial to use θ_{13} by the reactor experiments for the measurement of $\delta_{\rm CP}$.

Double Chooz is unique that the detector's contamination level is very low. It results in low accidental background rate. Moreover, layout of the detectors and reactors (Figure 2.4) of Double Chooz is favorable for reducing reactor flux uncertainty [33]. The flux at the detector is proportional to $1/r^2$, where r is distance between the reactor core and the detector. In Double Chooz, the ratio of $1/r^2$ between the near and far detectors are close for two reactor cores. Therefore, most of systematic uncertainties on the flux

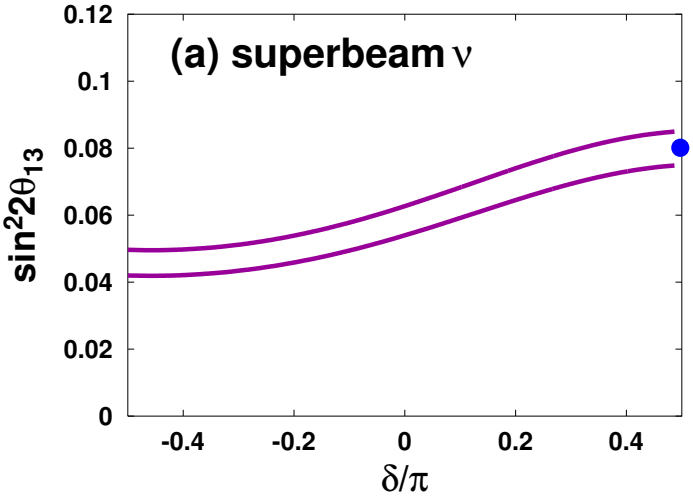

Figure 2.5: Allowed region of $\sin^2 2\theta_{13}$ and δ in the accelerator neutrino experiments. $\sin^2 2\theta_{13}$ and δ are assumed to be 0.08 and $\pi/2$, respectively [32].

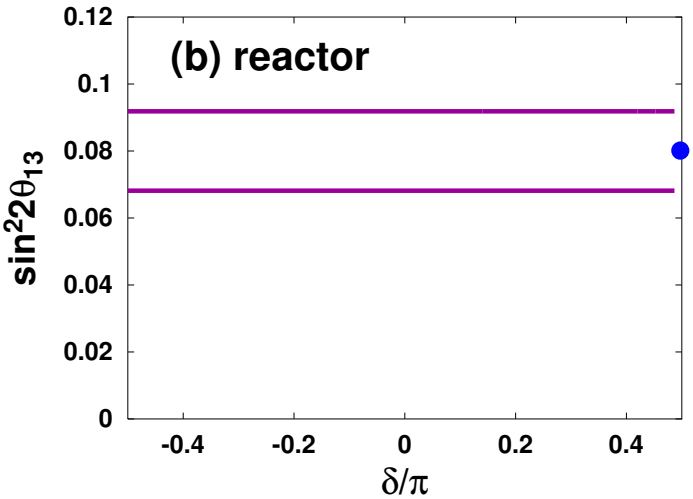

Figure 2.6: Allowed region of $\sin^2 2\theta_{13}$ and δ in the reactor neutrino experiments [32].

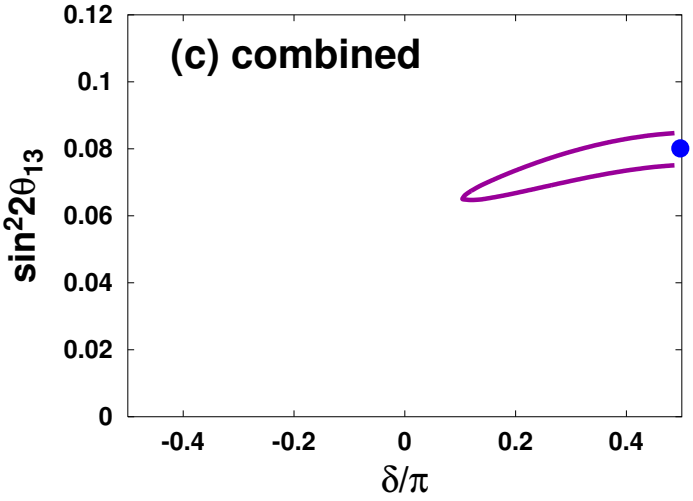

Figure 2.7: Allowed region of $\sin^2 2\theta_{13}$ and δ in a combination of the reactor and accelerator neutrino experiments [32].

prediction are canceled in comparison of the measurements by two detectors. The other experiments, for example, Daya Bay experiment is unique to low cosmogenic background, since the detector is located in deep underground. Signal and background rates in Double Chooz, Daya Bay, and RENO are summarized in table 2.2. In Double Chooz, the low IBD rate can be mitigated by using neutron captures on hydrogen nuclei as delayed events [34]. More than twice of IBD events can be expected by a combination of the gadolinium and hydrogen analyses. Since neutron captures on hydrogen nuclei has low energy and long capture time, accidental background is getting more dominant. Double Chooz has advantageous among the experiments for the hydrogen analysis, because of its low accidental rate. As time passes, uncertainties on θ_{13} becomes more systematic dominant. It means the cross validation from the different experiments is important.

In addition, it is possible to measure Δm^2_{31} by energy spectrum distortion and baseline between the reactors and detectors. By freeing both parameters $\sin^2 2\theta_{13}$ and Δm^2_{31}, $\Delta m^2_{31} = 2.95^{+0.42}_{-0.62} \times 10^{-3}$ eV^2 and $\sin^2 2\theta_{13} = 0.099^{+0.016}_{-0.012}$ were obtained from a combination the reactor experiments [35]. Figure 2.8 shows the reactor $\bar{\nu_e}$ survival probabilities with respect to baseline by the three experiments: Double Chooz, Daya Bay, and RENO [36].

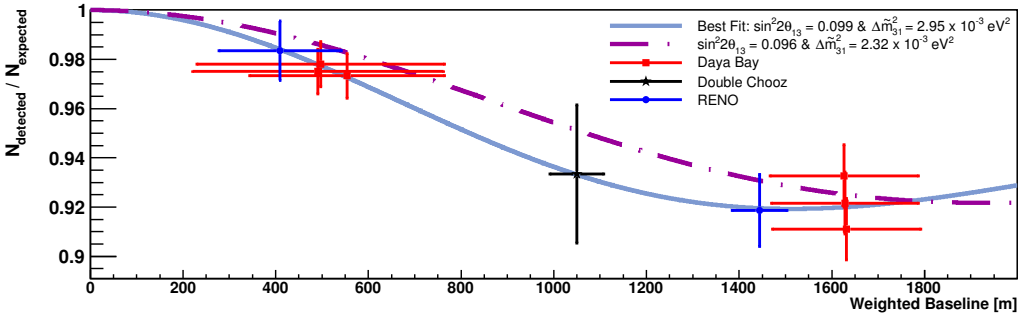

Figure 2.8: reactor $\bar{\nu}_e$ survival probabilities with respect to baseline [36].

Table 2.2: Signal and background rate (per day) in three experiments: Double Chooz [37], Daya Bay [29], and RENO [27].

Setup	IBD	^{9}Li/^{8}He	FN / SM	Accidentals
Double Chooz				
Far	37.7 ± 0.69	$0.97^{+0.41}_{-0.16}$	0.604 ± 0.051	0.070 ± 0.003
Daya Bay				
AD1 (EH1)	653.30 ± 2.31	2.40 ± 0.86	0.92 ± 0.46	9.54 ± 0.03
AD2 (EH1)	664.15 ± 2.33	2.40 ± 0.86	0.92 ± 0.46	9.36 ± 0.03
AD3 (EH2)	581.97 ± 2.07	1.20 ± 0.63	0.62 ± 0.31	7.44 ± 0.02
AD4 (EH3)	73.31 ± 0.66	1.20 ± 0.63	0.62 ± 0.31	2.96 ± 0.01
AD5 (EH3)	73.03 ± 0.66	0.22 ± 0.06	0.04 ± 0.02	2.92 ± 0.01
AD6 (EH3)	72.20 ± 0.66	0.22 ± 0.06	0.04 ± 0.02	2.87 ± 0.01
RENO				
Far	72.78 ± 0.95	2.59 ± 0.75	0.97 ± 0.06	0.68 ± 0.03
Near	779.05 ± 6.26	12.45 ± 5.93	5.00 ± 0.13	4.30 ± 0.06

Chapter 3

The Double Chooz detector

3.1 Overview

3.1.1 Setup

The Double Chooz experiment uses reactors in a nuclear power plant as neutrino sources. The plant is located in Chooz, France. The location is shown in Figure 3.1 marked with a red circle. Figure 3.2 shows the locations of reactors and detectors.

Up to now, the Double Chooz uses only one detector to measure the neutrinos from two reactor cores in the Chooz power plant. In addition, another detector is under construction. The currently running detector is named far detector (FD), which is located 998 m and 1115 m from the reactor cores. The other detector named near detector (ND) is planed to be located at 351 m and 465 m from the reactors. The location of the FD is favored based on equation (2.13), at which the electron antineutrino survival probability is close to the minimum value, i.e. $L \sim 1\,\mathrm{km}$ with the value $\Delta m^2_{31} = 2.32^{+0.12}_{-0.08}\,\mathrm{eV}^2$ measured from the MINOS experiment [23]. However, with the distance of FD from the reactors, the survival probability is slightly off from the minimum, because FD of Double Chooz reuses the experimental hall of the former CHOOZ experiment, which had already existed. The ND is located where the effect of neutrino oscillation is considered to be negligible. In order to reduce the cosmic muon backgrounds, detectors are placed underground with overburden of about 300 m.w.e. (110 m underground) for the FD and about 115 m.w.e. (40 m underground) for the ND.

A Double Chooz detector consists of an Inner Detector (ID), an Inner Veto (IV), and an Outer Veto (OV) as shown in Figure 3.3. The ID is used for detection of neutrinos while the IV and OV are equipped for identification of comic muons. The ID and IV compose multilayer concentric cylindrical tanks having chimneys in the center at the top of each tank. The OV is placed above the shielding of the main detector. Each of these subdetectors will be described in detail in later sections.

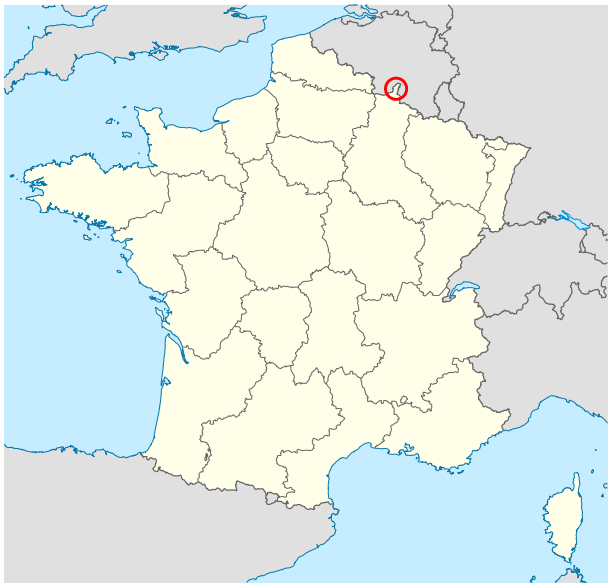

Figure 3.1: Double Chooz is an experiment in Chooz, Ardennes, France. Its location is north of France, marked with a red circle.

Figure 3.2: A picture of the Chooz reactor complex. The locations of the two reactors as well as the two detectors are shown.

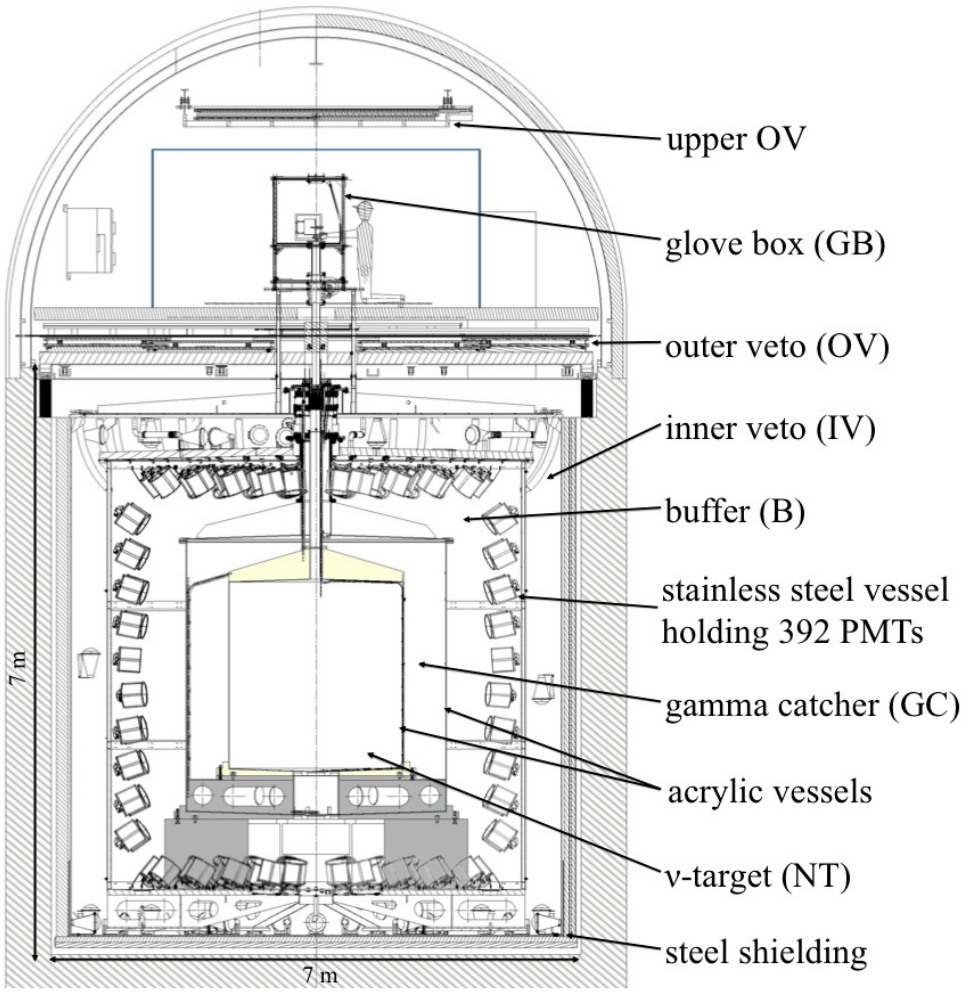

Figure 3.3: A cross-sectional view of the Double Chooz detector.

3.1.2 Principle of neutrino detection

Neutrinos from the reactors are observed by detecting signals of inverse beta decay (IBD) reaction in the detector. The IBD interaction is:

$$\bar{\nu_e} + p \rightarrow e^+ + n. \tag{3.1}$$

The electron antineutrino interacts with a free proton in the detector to produce a positron and a neutron. These two products emit signals, and they are used for the neutrino detection in the experiment. The positron signal and neutron capture signal are called "prompt signal" and "delayed signal", respectively, because the reaction of positron annihilation happens instantaneously after the IBD reaction while the neutron loses its energy by thermalization and finally captured on nuclei in the detector, which happens in average 30 μs after the prompt signal. The neutron capture energy peak is 8 MeV if the neutron is captured on gadolinium nuclei which is doped in the detector ($\mathrm{Gd}^* \rightarrow \mathrm{Gd} + \gamma'\mathrm{s}$), while the peak is 2.2 MeV if captured on hydrogen nuclei ($\mathrm{n} + \mathrm{p} \rightarrow \mathrm{d} + \gamma$). Coincidence of the prompt and delayed signals are used for the neutrino identification. In the Double Chooz, gadolinium events are designed to be used for the neutrino oscillation measurement, however, the signals of neutron capture on hydrogen nuclei are also used in published papers [38, 6] from the Double Chooz collaboration. In this paper, neutron captures on gadolinium nuclei events are used for the neutrino selection, since the energy of 8 MeV is much higher than the energy of natural radioactivities. Therefore, backgrounds from the random coincidence can be suppressed by using the signals of neutron captures on gadolinium nuclei. It also serves for accurately defining the target volume without fiducial cuts.

Both prompt and delayed signals emit γ rays. The positron reaction in the detector is ionization and electron-positron annihilation, and γ rays are emitted. The neutron is captured on gadolinium nuclei and it emits γ rays as well. The γ rays interact with scintillator, and longer wavelength light is emitted.

Energy threshold of the inverse beta decay reaction is calculated from the equation below:

$$E_{\bar{\nu}}^{\mathrm{th}} = \frac{(m_n + m_e)^2 - m_p^2}{2m_p} = 1.806 \text{ MeV} \tag{3.2}$$

where, m_n, m_e, and m_p are masses of neutron, electron, and proton, respectively.

Neutrino energy is measured from the prompt signals using relationship between the energy of neutrino and prompt signal, which is represented by following formula:

$$E_{\bar{\nu}} = \frac{2m_p E_{e^+} + m_n^2 - m_p^2 - m_e^2}{2\left(m_p - E_{e^+} + \sqrt{E_{e^+}^2 - m_e^2}\cos\theta\right)} \tag{3.3}$$

Where $E_{\bar{\nu}}$, E_{e^+} are the energies of electron antineutrino and positron respectively. θ is an angle between incident neutrino and emitted positron. Since the mass of the electron

is much smaller than that of a proton or neutron, so the equation is approximated by the following equation:

$$E_{\bar{\nu_e}} \sim E_{e^+} + m_n - m_p. \tag{3.4}$$

Therefore, the visible (or observed) energy is measured by the prompt signal like:

$$E_{\rm vis} = E_{\rm e^+} + m_{\rm e} \sim E_{\bar{\nu_e}} - m_n + m_p + m_e \sim E_{\bar{\nu_e}} - 0.78 \text{ MeV}. \tag{3.5}$$

Since the energy threshold of the inverse beta decay reaction is 1.8 MeV, the minimum energy is 1.02 MeV. Double Chooz detector is able to measure the 1 MeV energy with close to 100 % efficiency.

3.1.3 Dominant backgrounds

There are three kinds of dominant backgrounds in the Double Chooz experiment: 1) accidental backgrounds, 2) correlated backgrounds (fast neutrons and stopping muons), and 3) cosmogenic isotopes (^{9}Li and ^{8}He). These backgrounds are briefly introduced here for better understanding of the Double Chooz detector. Detail of the backgrounds are described in chapter 10.

Accidental background is an accidental coincidence of two independent signals. The origin of the prompt signal is mainly γ rays from the detector materials produced from natural radioactivity, and the delayed signal is such as recoil proton by fast neutron and muon-induced spallation neutron capture on gadolinium nuclei.

So-called fast neutron and stopping muon are categorized as the correlated background. Fast neutron is produced by spallation interaction by cosmic muons in the rocks surrounding the detector, which enters into the detector and reacts with protons in the detector. Stopping muon is a muon which enters into the detector, then stops and decays into an electron in the detector. These reactions are origins of backgrounds.

Finally, cosmogenic isotopes such as ^{9}Li and ^{8}He are created in the detector by an incident cosmic muon. These isotopes emit neutron in association with its β decay, and become backgrounds with lifetimes of 257.2 ms and 172 ms, respectively. These are found to be the largest background in Double Chooz.

3.2 Inner Detector

The ID consists of three cylindrical vessels, called Neutrino Target (NT), Gamma Catcher (GC), and Buffer from inside to outside. The vessels of the ID and GC are made of transparent acrylic material. It is transparent to UV and visible light when wavelength is more than 400 nm. The three components will be described one by one below.

3.2.1 Neutrino Target

The NT consists of a 2.30 m diameter, 2.46 m height 8 mm thick transparent acrylic vessel. The NT is filled with 10.3 m^3 gadolinium loaded liquid scintillator. The concentration of gadolinium is 1 g/l. The scintillator was newly developed for the Double Chooz experiment. The requirements of the liquids for the NT were: 1) Gd solubility, 2) optical transparency, 3) radio purity, and 4) chemical stability. Especially, the chemical stability of gadolinium-loaded scintillator was taken measures in view of the CHOOZ experiment, in which the scintillator was optically unstable due to an effect of gadolinium, that limited sensitivity to the θ_{13} measurement [25]. To satisfy these requirements, as well as technical requirements and safety considerations, the following compounds were chosen [40]:

- 20% ortho-phenylxylylethane (PXE),
- 80% n-dodecane,
- 0.007 g/cm^3 2,5-diphenyloxazole (PPO),
- 20 mg/cm^3 4-bis-(2-methylstyryl)benzene (bis-MSB)

The PXE and the n-dodecane are scintillator solvent. By mixing dodecane, the light yield reduces as shown in the figure 3.4, however, it was needed for improving the chemical compatibility with the acrylic. The PPO is a fluor. The bis-MSB is a wavelength shifter, added for shifting the wavelength of the scintillation light to more transparent region. Since metal gadolinium does not dissolve in the liquids, a metal-organic complex metal-β-diketone, $Gd(thd)_3$, Gd(III)-tris-(2,2,6,6-tetramethyl-heptane-3,5-dionate) is formed for solubility. These complexes are known for their stability and high vapor pressure, which allowed to purify the material by sublimation, reducing radio impurities U, Th and K. Optical stability was measured by dedicated setup at Max-Planck-Institut für Kernphysik (MPIK), Germany before the installation as shown in Figure 3.5. Stability of the light yield in the Double Chooz detector is monitored using neutron capture peaks as described in section 5.1.

3.2.2 Gamma Catcher

The GC is a 3.39 m inner diameter and 3.55 m inner height cylindrical vessel having a 21.5 m^3 volume filled with liquid scintillator. However, unlike the NT, it does not contain gadolinium.

The purpose of GC is to detect the escaping gamma rays from the NT produced by neutrinos via inverse beta decay. It enables to avoid the fiducial volume cut, which can be a cause of systematic uncertainty on the number of target protons.

The mixture of the liquids is similar to that of the NT, because the similar material compatibility, density and optical properties are required. The light yield of the gamma

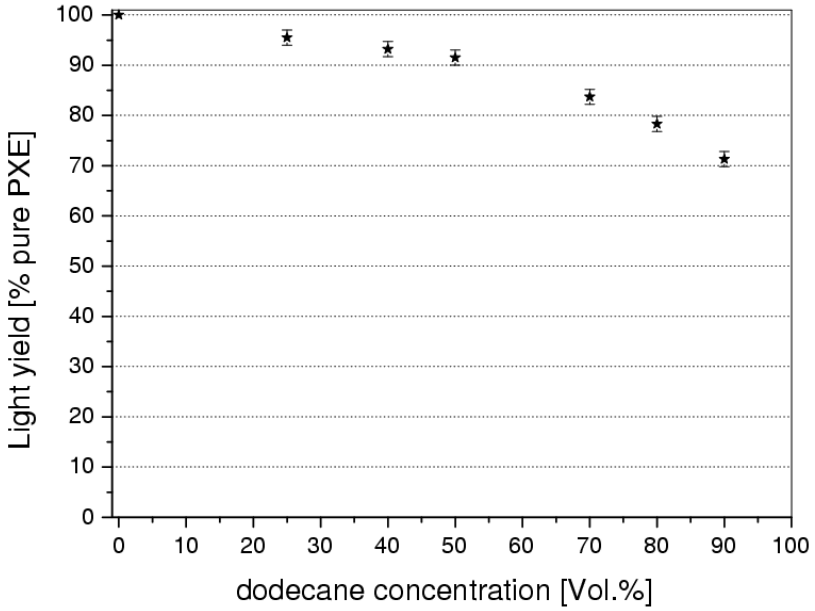

Figure 3.4: Scintillation light yield of PXE/dodecane mixture with respect to dodecane concentration [41]. In this study, the PPO concentration was kept at 6 g/l.

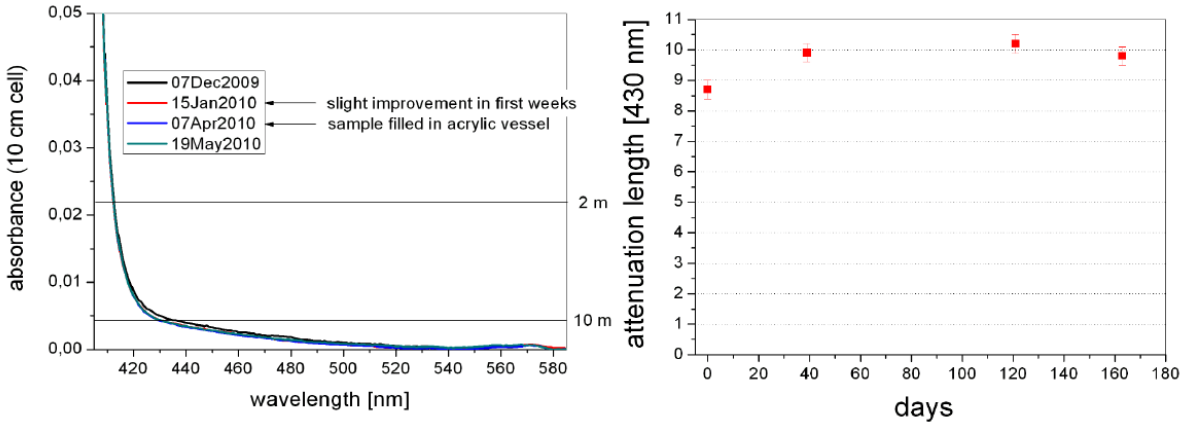

Figure 3.5: Left plot shows the absorbance of liquid scintillator with respect to wavelength. Right plot shows the stability of attenuation length with 430 nm wavelength light.

catcher was adjusted to provide the same photoelectron per energy as that of the NT. Since the gadolinium loaded scintillator has stronger quench effects, than that of in the GC, GC scintillator has 10 - 20 % higher light yield. To take measures on the effect, non-scintillating mineral oil was mixed in the GC liquids to suppress the light yield. In addition, density of the GC liquid scintillator must be the same as that of the NT to keep the same pressure to the acrylic vessel. To satisfy the requirements of density and light yield, the following mixture was chosen:

- 30% dodecane,
- 66% Ondina 909 (mineral oil),
- 4% PXE,
- 2 g/l PPO,
- 20×10^{-3} mg/L bis-MSB.

3.2.3 Buffer

The buffer is formed by a cylindrical vessel 5.516 m in diameter and 5.674 m in height, having about 100 m^3 volume filled with non-scintillation liquid. It shields the GC and the NT from radioactivity e.g. gamma rays emitted by the photomultipliers.

The requirements of liquids in the buffer is to have a similar density to that of the GC, because of the thin acrylic vessel between them. Also, material compatibility with acrylic vessel and the photomultipliers, and transparency in the scintillator emission wavelength region are required. Mixture of 46 % n-alkanes and 54 % mineral oil was chosen as liquids for this purpose.

On the inner wall of the buffer, 390 10-inch photomultiplier tubes (PMTs) are attached for detecting photons from the scintillation emissions. The details of the PMTs are described in the next section.

3.2.4 Inner detector photomultiplier tubes

Double Chooz uses 390 10-inch diameter photomultiplier tubes (PMTs). The PMTs are based on Hamamatsu R7081 [42, 43]. The specification is shown in Table 3.1 and the cross-section view is shown in Figure 3.6.

The PMTs are specially developed for the Double Chooz experiment. The photomultiplier glass is formed in platinum coated glass furnace to reduce radioactive contamination. The radioactivities of ^{238}U, ^{232}Th and ^{40}K were measured to be 13 ppb, 61 ppb and 3.3 ppb respectively on the wall of the glass furnace[44].

The side of the PMTs are surrounded by cylindrical μ metal to shield the geo-magnetic field. The shield is 315 mm in diameter, and 325 mm in height. The magnetic field is reduced by one to tenth.

The base circuit of the photomultiplier tube is shown in Figure 3.7. 10 box-and-line structure dynodes are used in the PMT. The box-and-line structure has advantages in good collection efficiency and good uniformity. Since muon signal has large energy, it affects the waveform of the PMT for relatively long time. The back termination 49.9 Ω resistance (which is indicated with R24 in Figure 3.7) is equipped to damp reflections of signals which is caused by impedance mis-matching from muon signal. It is beneficial for reducing dead time to observe neutrinos.

The gain is an important property of the PMTs. It is defined by the following formula:

$$g = a^n \left(\frac{V}{n+1} \right)^{kn}. \tag{3.6}$$

Where g is the gain, V is the voltage, a is a constant parameter, n is the number of dynodes and k is a constant that depends on material of the dynodes. By defining α and β as

$$\begin{aligned} \alpha &= \frac{a^n}{(n+1)^{kn}}, \\ \beta &= kn, \end{aligned} \tag{3.7}$$

we can express the gain by the following formula:

$$g = \alpha V^{\beta}. \tag{3.8}$$

800 PMTs for both the FD and the ND including the spares were tested before carrying to Chooz village [44]. Half of PMTs were purchased in Japan, and the other half were purchased in Germany. The tests were done in the following steps. 1) First, the prototype PMTs were tested before the mass production, and their performance were evaluated. The feedback was sent to the manufacturer. 2) After the mass production was completed, all PMTs were with 'step-1' evaluation system which confirms the basic functionality and measure various specifications one by one. 3) When the step-1 evaluation was completed, the PMT was sent to Max-Planck-Institut für Kernphysik (MPIK), Germany The step-1 test were carried out in Japan for the half PMTs while the other half were tested in MPIK. Then, all PMTs were tested again with 'step-2' evaluation system in MPIK to check if there is damage during the transportation. The step-1 and step-2 tests were started in May 2008, which finished in November 2008, took six months in total.

In the step-1 and step-2 evaluations, the following characteristics were examined:

- PMT gain (step-1, step-2)
- Peak to valley ratio (P/V ratio) (step-1, step-2)

- Dark count rate (step-1, step-2)
- Transit time spread (TTS) (step-1)
- Quantum efficiency × collection efficiency (QE × CE) and its uniformity (step-1)

Evaluation systems were specially developed for testing the items listed. Both step-1 and step-2 systems use LED to inject light into the PMTs.

The PMT gain is defined as a number of electrons collected at the anode to a number of photoelectrons at the cathode. The gain can be measured using the following equation:

$$g = \frac{2 \times Q_{\text{count}} \times G_{\text{gain}}}{G_{\text{amp}} \times e}. \tag{3.9}$$

In this definition, Q_{count} is the ADC count of a single photoelectron peak after pedestal subtraction. The pedestal is measured as an averaged ADC count in absence of signals. G_{gain} is a gain of ADC electronics system defined as a ratio of charge to ADC count. G_{amp} is the gain of an amplifier which was used for adjusting the signal to be in the ADC dynamic range. e is charge of an electron. Back-termination effect of the base circuit is taken into account by the multiplication by 2.

P/V ratio is related to the ability of separation of single photoelectron (p.e.) signal against the noise. The value is defined as a ratio of the maximum height of single p.e. peak to the minimum height between the pedestal and single photo electron peak (figure 3.9). The larger P/V ratio means the PMT has better ability to separate the 1 p.e. signals from the pedestal.

Dark count rate is measured without light. There are number of causes for it. For example, thermal electrons from photocathode and dynodes, ionization in the PMT, and so on. In the test, it was measured with a threshold of 0.25 PE. Typically, a neutrino signal is measured with single photoelectron level with the Double Chooz detector. So it is important to ensure that the dark count rate is low enough, because the dark count can be identified as a background.

Transit time is a time difference between the time of light injection on the photocathode and the time of signal output. The transit time spread (TTS) is the spread of samples of the transit time. In the test, the transit time was measured with 1 photoelectron level signal with 0.25 PE threshold, and the TTS was defined as a full width at half maximum (FWHM) of the distribution. The lower TTS value indicates the better time resolution. Especially it is important for the performance of position reconstruction.

The term quantum efficiency (QE) is a ratio of incident photon to photoelectron at the cathode of the PMT. Collection efficiency (CE) is the probability that a photoelectron arriving to the effective area of the first dynode in the PMT. QE × CE indicates how effectively the incident photon can be converted into photoelectrons.

Finally, the result is summarized in Table 3.2. Almost all of the PMTs satisfied the specification shown in Table 3.1. Only few PMTs did not satisfy the specification from

Table 3.1: Specification of the ID PMT R7081 [42]

Property	Value
Wavelength region	300 nm - 650 nm
Photo cathode	Bialkali
Peak wavelength	420 nm
Diameter	ϕ 253 mm
Number of dynodes	10
Glass weight	1150 g

Table 3.2: Specification and the results of step-1 and step-2 tests

Item	Spec		Step-1		Step-2	
	Min.	Max	Min.	Max.	Min.	Max.
HV obtaining 10^7 gain	1150	1650	1210	1610	1190	1590
P/V ratio	2.5	-	3.0	5.5	3.4	5.6
Dark count rate (Hz)	-	8000	2100	9000	700	2600
TTS (FWHM) (ns)	-	4.4	2.3	4.1	-	-
QE $\times$ CE (%)	20.8	-	20.3	26.7	-	-

the step-1 evaluation, and the products were replaced by Hamamatsu Photonics K.K.. Ten PMTs were chosen as spares. They have relatively low QE $\times$ CE, unstable dark count rate or large gain non-linearity over the position of photocathode.

3.3 Inner Veto

The Inner Veto (IV) is used to identify cosmic muons and protecting the ID from fast neutrons produced in surrounding rock by muons.

The IV is a cylindrical vessel having radius of 3.3 m height of 6.8 m, and it surrounds the ID. It is filled with liquid scintillator (48.4 % LAB (linear alkyl benzene), 51.6 % Cobersol C70 (n-alkanes), 2 g/l PPO and 20 mg/l bis-MSB). The wall of the ID is made of stainless steel, therefore the ID and the IV are optically separated.

On the wall of the IV, 78 8-inch PMTs are attached. The IV PMTs are Hamamatsu R1048 previously used in the IMB experiment. The PMTs were tested and modified for Double Chooz [39]. The number and arrangement of the PMTs were decided using Monte-Carlo simulation to achieve more than 99% rejection efficiency for muons which penetrate the detector. The layout is summarized in Table 3.3 and figure 3.10.

Cosmic muon background and muon induced background can be reduced by eliminat-

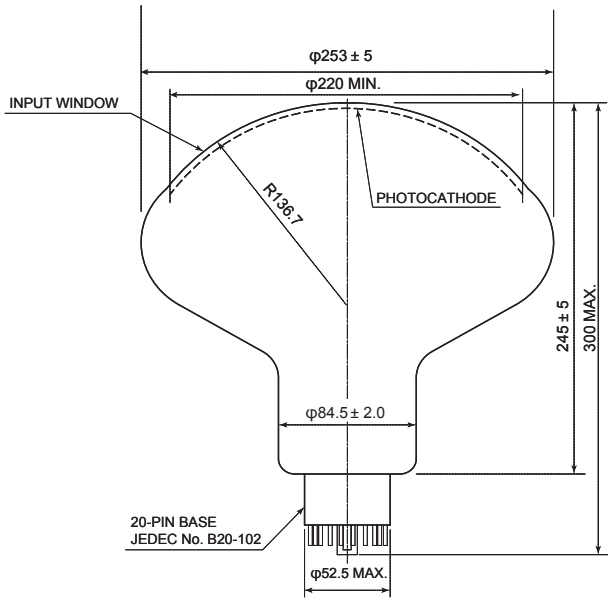

Figure 3.6: A cross-sectional view of the inner detector 10-inch PMT Hamamatsu R7081 [44].

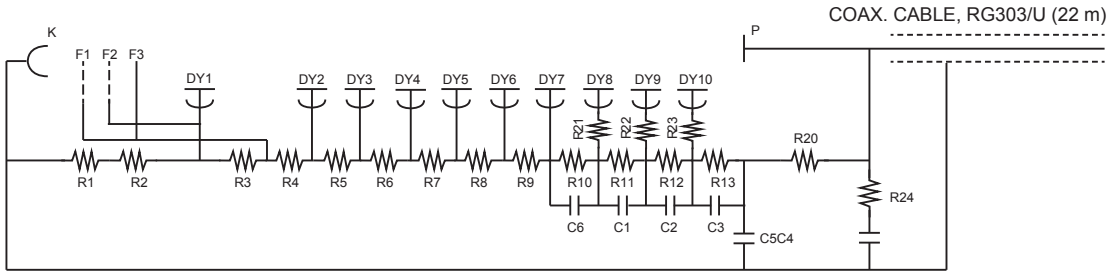

Figure 3.7: The base circuit of the PMT R7081 [44].

Table 3.3: The layout of the IV PMTs.

Ring location	# of PMTs	Direction
Top of the buffer vessel	12	Horizontal, alternating inward and outward
Side wall 30 cm below the lid	12	Pointing alternatively inward and outward
Side wall in the center	12	Pointing alternatively inward and down
Bottom of the veto	24	Pointing alternatively inward and up
Bottom of the veto	18	Pointing alternatively inward and outward

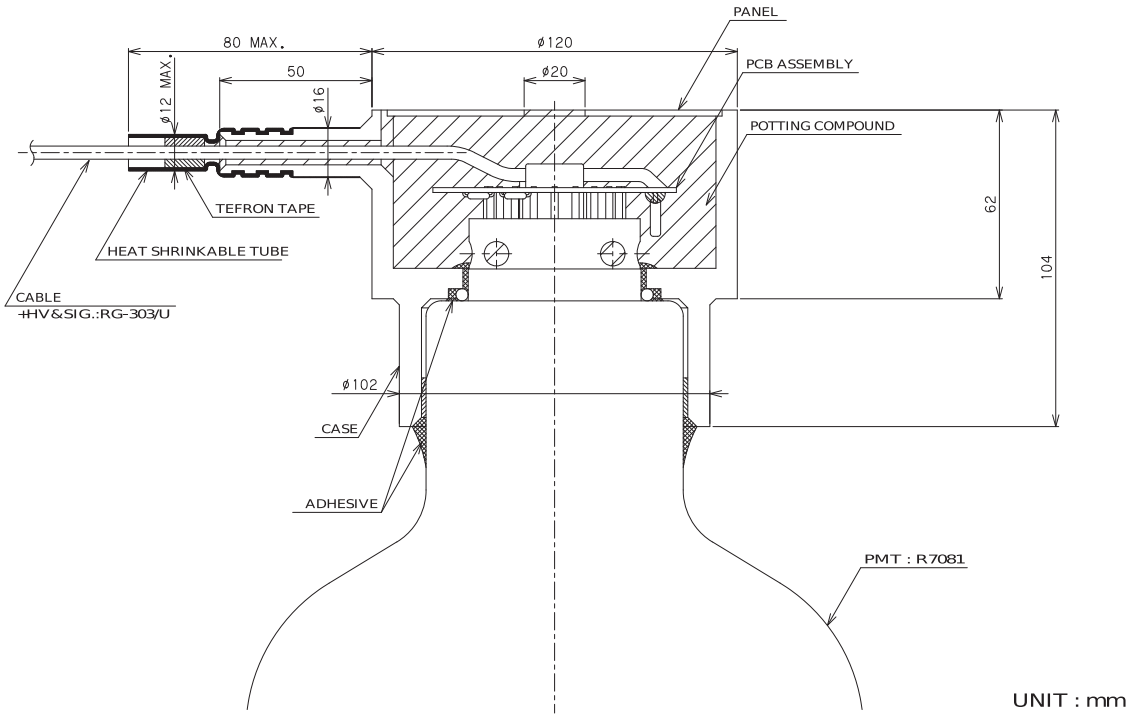

Figure 3.8: A cross-sectional view of a base of the PMT R7081 [44].

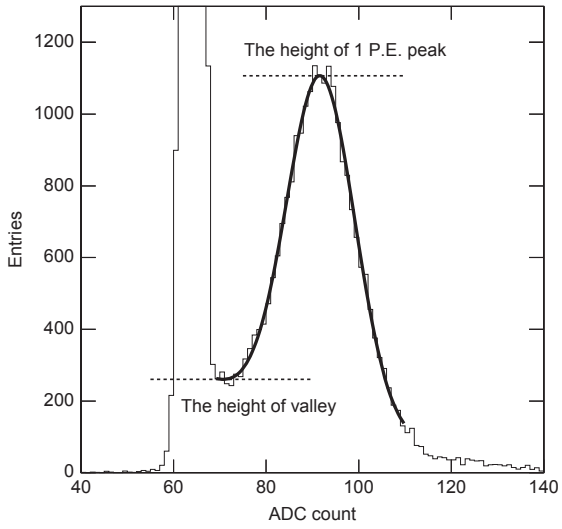

Figure 3.9: The peak to valley (P/V) ratio is characterized from the peak height of single photoelectron and the valley between the pedestal peak and single photo electron peak derived from the sampling of low energy input signal. [44]

Table 3.4: Composition of the Double Chooz liquids.

	Aromatic	Oil	Fluor	WLS	Gd-Compound	Density
Target	$C_{16}H_{18}$(20%)	$C_{12}H_{24}$(80%)	PPO (6 g/l)	bis-MSB (50 mg/l)	Gd-dpm (1 g/l)	0.800
gamma-catcher	$C_{16}H_{18}$(20%)	$C_{12}H_{24}$(80%)	PPO (3 g/l)	bis-MSB (50 mg/l)	/	0.798
Buffer	/	Mineral Oil	/	/	/	0.820
Veto	/	Mineral Oil	PPO (6 g/l)	bis-MSB (10 mg/l)	/	0.821

ing events tagged as muons by the IV. Moreover, the IV is aimed to shield the ID from the external radioactivity and spallation neutrons created by cosmic muons with 50 cm thick layer of the liquid scintillator.

Finally, the composition of the Double Chooz liquids is summarized in Table 3.4.

3.4 Readout electronics system

The block diagram for the ID and the IV readout electronics and data acquisition system are shown in Figure 3.11. Each component will be described in this section.

3.4.1 Photomultiplier tubes and splitter

The PMT is connected to the front-end electronics and the High Voltage (HV) system through the HV splitter. The PMT to the splitter is connected by a single cable RG303/U. Having only a single cable is advantageous for reducing the cost and complexity of cabling work during installation, avoiding noise that can be caused by ground loop and reducing inactive region due to cable holes. The splitter works for separating signal (5 mV/PE) and HV supply ($\sim$ 1.3 kV). It is custom made by CIEMAT group in Spain [45].

3.4.2 High Voltage system

The HV system supplies HV for all PMTs in the detector. Double Chooz uses HV frames and modules produced by CAEN S.p.A..

The HV system consists of multichannel power supply system SY1527LC crate and floating HV supplies A1535P module [46]. The voltage value $\sim$ 1.3 kV of HV supply was set so that PMTs provide a gain of 10^7.

Since the high voltage affects PMT gain, the HV system was calibrated for ensuring stability of PMT gain [47]. The calibration is to measure the output voltage with respect to input value. It was performed using a specially developed module by CAEN S.p.A., which enables to do the whole calibration sequence automatically. The stability of HV output was measured within 0.15 % for about two months for all channels including the ID and the IV. 0.15 % of HV variation corresponds to approximately 1.2 % of PMT gain

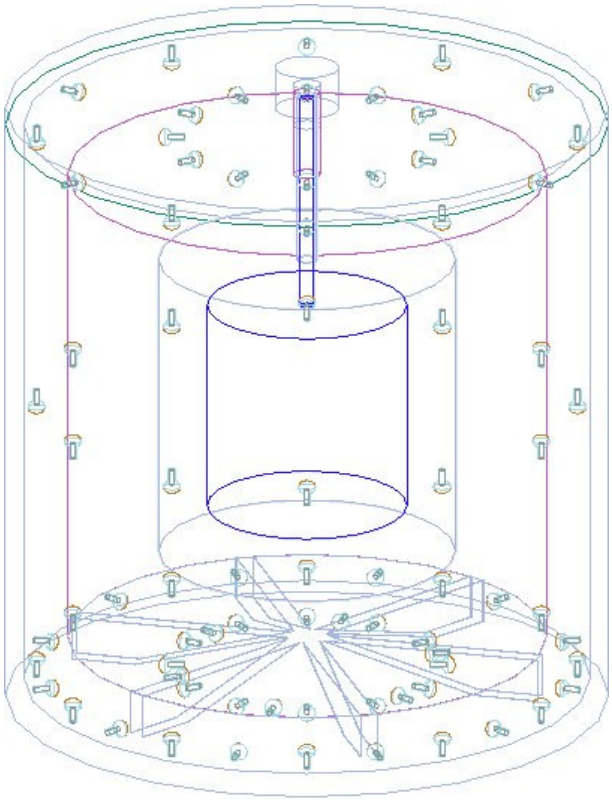

Figure 3.10: The layout of the IV PMTs

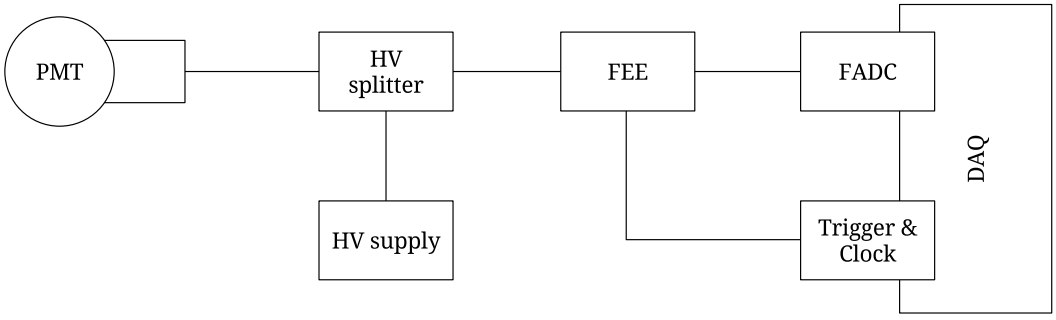

Figure 3.11: Double Chooz electronics system including readout and data acquisition system.

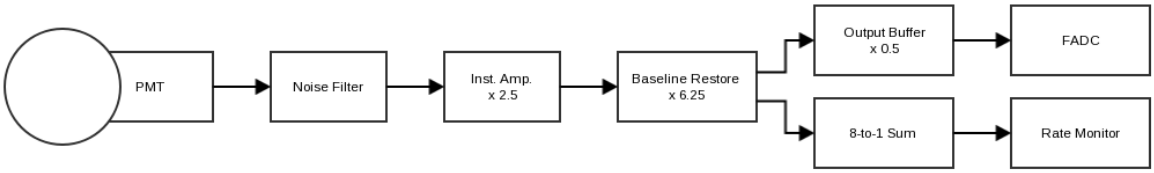

Figure 3.12: Block diagram of FEE

variation. It means the deviation of HV system does not contribute as a major factor of systematic uncertainties of the neutrino oscillation measurement.

3.4.3 Front-end electronics

The front-end electronics (FEE) amplify the signal and also provide a visible energy stretcher signal which are used to create trigger [48]. Typically, neutrino signal makes single photoelectron signal for each PMT. However the single photoelectron level of signal (4 mV to 5 mV) is too small to be read from the flash-ADC by themselves. The FEE amplifies the input signals by a factor of 7.8 to make it suitable to be read by flash ADCs. Not only amplification but also some optimization is fullfilled during the multiple stages of amplification process. The optimizations are clipping, baseline restoring, and coherent noise filtering. Figure 3.12 is a block diagram of the FEE. We will describe about the neutrino channel first, and muon channel next.

The first stage of the neutrino channel is an instrumentation amplifier (IA) having a gain of 2.5, which is a combination of op-amps. The op-amp is designed to remove any signal that is common to both inputs. The shielding on the cables is connected to the module ground through a 4.7μF capacitor by which noise greater than 6.7 kHz flow to ground. Therefore, it works to reduce noises common in both signal and shielding of the cables mainly caused by power supplies. The next stage is made of two inverting op-amps and an operational transconductance amplifier having a gain of 6.25. It works to restore a drift of baseline rapidly. It is important especially after a large pulse such as a muon which makes large drift. The output of the second stage is divided to three ways. One directly goes to the 8-to-1 summation stage to make a trigger signal for the custom made trigger system. And the other two goes through output buffer to flash ADC and rate monitor system. The output buffer is a dual op-amp with no gain.

Table 3.5: Basic characteristics of flash ADC VX1721

Property	Value
Number of channels	8 / slot
Time resolution	2 ns / sample (500 MHz)
Time precision	less than 5 ps
Number of samples	2048 / event
Dynamic range	8 bit / 20 mA / 1V
SRAM memory buffer size	2 MByte / channel

3.4.4 Flash ADC

Waveforms from the PMTs are digitized and recorded using flash ADC waveform digitizer VX1721 (VME64x) developed by CAEN S.p.A. in collaboration with AstroParticule et Cosmologie (APC) [46]. The basic specification of the flash ADC is summarized in Table 3.5. The module has 500 MHz sampling rate (1 sample per 2 ns), 8 channels, 8 bit resolution and 1 Vpp dynamic range. The meaning of the 8 bit resolution and 1 Vpp is that 0 to 1 voltage of input is converted into 0 to 255 digitized values. In this thesis, we call the digitized value as ADC (Analogue to Digital Count) value

The module provides a programmable way to apply DC offset to each channel. By changing the DC offset value, an offset of the ADC value is changed. In Double Chooz, since a PMT signal is negative voltage, therefore the DC offset is set so that the ADC value is kept around 210 (in 8 bit) for each channel [49] when zero voltage is applied. Figure 3.13 shows an example of waveform sampled with the module.

Each channel has 2 MByte static RAM memory buffer. The memory can be divided into 1024 memory buffers which we call "page". Each page can store 2048 samples corresponding to 4μs. When the flash ADC is operating, the data is continuously written into a page. If a trigger signal arrives, the the flash ADC stops writing to the current page and starts to write into the next page, so that the data can be taken without dead time. If all the pages are filled with data, the memory behaves like a FIFO (First In, First Out). It means the oldest data is overwritten by the current data stream. The number of pages for an event is adjustable, so it makes it possible to adjust a time window on demands. In Double Chooz, the time window is set to 256 ns (corresponds to 128 samples).

The flash ADC is known to have non-lienarity effect which can be characterized with two definitions: Differential Non-Linearity (DNL) and the Integral Non-Linearity (INL) [49]. First, the DNL is a deviation of step size of the ADC value. Ideally, a step size is 1/255 V, however there is a deviation of the size which can be positive or negative. We call this deviation as DNL. The INL is a deviation of ADC value with respect to input voltage originated by accumulation of the DNL. Since Double Chooz integrates the

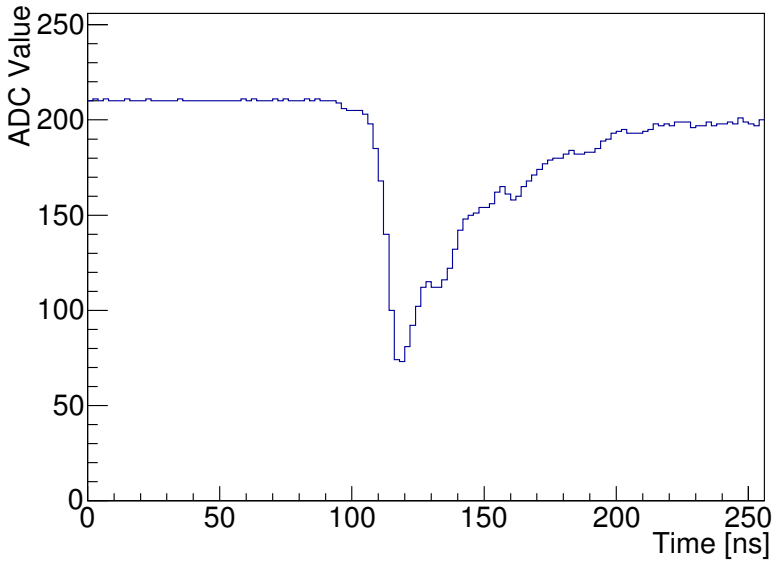

Figure 3.13: An example of waveform sample with the flash ADC VX1721. Since the PMT signal is negative, the waveform is going negative. The baseline is set to be around 210 ADC value. The time window is set to 256 ns, it corresponds to 128 samples with the sampling rate of 500 MHz.

waveform to calculate charge, the understanding of these non-linearity is important for the experiment. The detail of the evaluation of these non-linearity is described in the calibration chapter.

3.4.5 Trigger system

The role of the trigger system is to feed a trigger signal to the flash ADC. Since the experiment uses two different signals for neutrino identification, it requires a trigger of two signals with high efficiency. A trigger system was custom developed to fulfill requirements [50]. The custom made trigger system also provides following features that is needed for the experiment.

- Distribute common clock signal to data acquisition components
- Distributes a time stamp
- Distributes a unique event number
- Event classification

The common clock signal is needed for synchronization among the data acquisition components. The time stamp is used in the physics analysis of neutrino measurement when

requiring the coincidence of the prompt and delayed signals. The unique event number is used for identifying event. Also, trigger system characterizes events e.g. physics events, external trigger events, and so on.

The trigger system is implemented in a FPGA (Field Programmable Gate Array) XC2V500 manufactured by Xilinx Inc [51]. The FPGA is an integrated circuit designed such that customers can configure it by programming after manufacturing. The trigger system can be separated into two stages. We call the first stage as trigger board and the second stage as trigger master board.

Figure 3.14 shows a setup of the trigger system. The input of the trigger system is analogue signals from the PMTs which is processed in the front-end electronics beforehand. For the ID, typically eight PMTs are connected to a front-end electronics. Then, the front-end electronics produces a summed signal to be used as an input signal in the trigger board. The signals from two front-end electronics are summed and go to the trigger board. Therefore, it means 16 PMTs are grouped as a group to make input signal of the trigger board. For the IV, PMTs are grouped according to the location. Then, trigger boards process the signals and the outputs are processed in the trigger master board to make a trigger decision. The trigger master board is also connected with external triggers. The external triggers are:

- IDLI (ID Light Injection system) trigger
- IVLI (IV Light Injection system) trigger
- Calibration source trigger
- 470 nm laser trigger
- 365 nm laser trigger
- Dead time monitor trigger
- Outer Veto trigger

The trigger master board makes trigger words according to the trigger type. The configuration of the trigger word is defined as follows:

- Bit 0-3: TB A: pre-scale, neutrino like, neutron like, muon like
- Bit 0-6: TB B: pre-scale, neutrino like, neutron like, muon like
- Bit 12-17: TB IV: pre-scale, neutrino like, muon like, passing muon, stopping muon, crossing muon
- Bit 20-25: External triggers from calibration systems, trigger dead time monitor system and the Outer Veto
- Bit 28: Fixed rate trigger

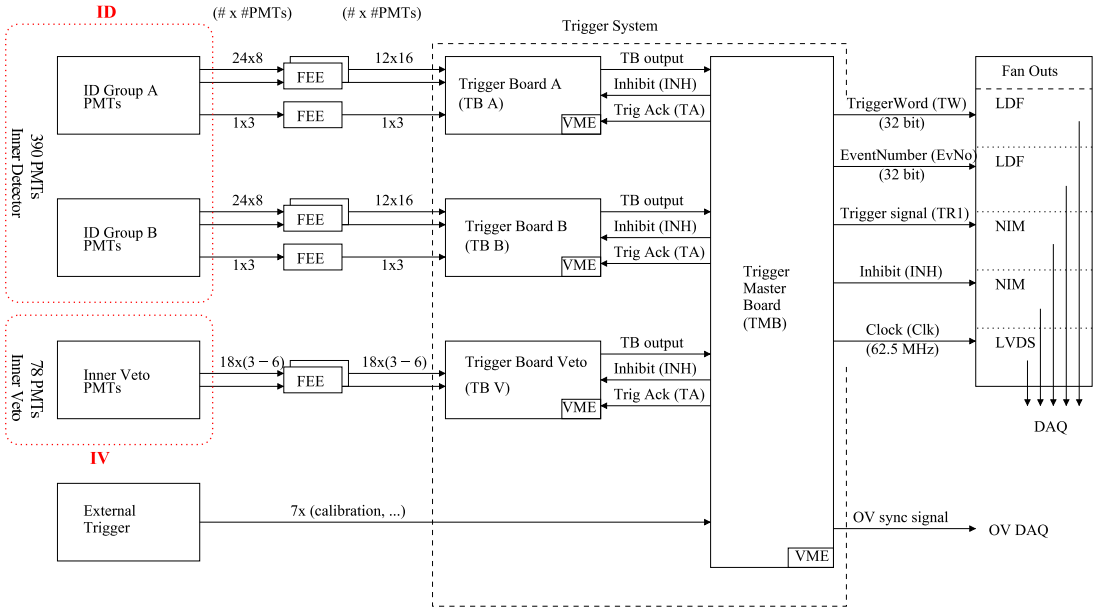

Figure 3.14: The setup of the trigger system of Double Chooz [50].

Physics trigger

Here, we will describe how the physics trigger is produced. The trigger decision is made using deposited energy in the detector and multiplicity condition of the active number of the PMT groups (figure 3.15). The deposited energy can be estimated from the PMT signal which is roughly proportional to the energy. The system allows to configure different energy thresholds.

For the ID, there are four thresholds: 1) Pre-scaled, 2) Low (neutrino like), 3) High (neutron like), and 4) Very high (muon like). We will explain one by one from the "pre-scaled" threshold. In Double Chooz, events with an energy lower than the "pre-scaled threshold" are eliminated such that the event rate is reduced by a factor of 1000 (it means one event is triggered in 1000 events). The pre-scaled threshold is low enough compared to the neutrino energy. The trigger is used for studies such as trigger efficiency or backgrounds. The "low (neutrino like) threshold" is a physics threshold of the ID corresponds to minimum energy of neutrino inverse beta decay (1.022 MeV). The threshold is set to approximately to 350 keV, although the inverse beta decay energy is higher. The "high (neutron like)" and the "very high (muon like)" thresholds are used for event classification. As their names suggest, the thresholds flag energy of neutron like signal and muon like signal. The "high" threshold value corresponds to approximately 6 MeV, the energy of neutron capture by a gadolinium nucleus. Finally, the "very high" threshold is set to approximately 50 MeV considering energy of muons. Furthermore, as mentioned before, the multiplicity is applied. A threshold of each group is set to 80 % of the "low (neutrino like) threshold". Firing of at least 2 groups out of 13 groups is required. However, no multiplicity condition is applied for the pre-scaled trigger.

For the IV, there are three thresholds: 1) "pre-scaled", 2) "neutron like", and 3) "muon like". As same as the ID, the pre-scaled threshold is set to reduce events by a factor of 1000. The neutron like threshold is set at 10 MeV, muon like threshold is set at 50 MeV. The multiplicity condition is applied to only the muon trigger, the threshold is set to at least 10 active groups out of 18 groups. A group threshold for the IV is set considering the number of PMTs in the group.

3.5 Outer Veto

The OV consists of plastic scintillator strips covering above the shielding of the ID, and is used for cosmic muon identification. There are a lower OV and an upper OV. The layout is shown in figure 3.16. The lower OV is directly mounted above the shielding. A region around the chimney is left open for the calibration source insertion. To cover the region around the chimney, the upper OV is mounted above the chimney and glove box. Thus, it is possible to cover the center as well as accessing to the area around the chimney when needed for source insertion. The lower OV has 13 m $\times$ 7 m area.

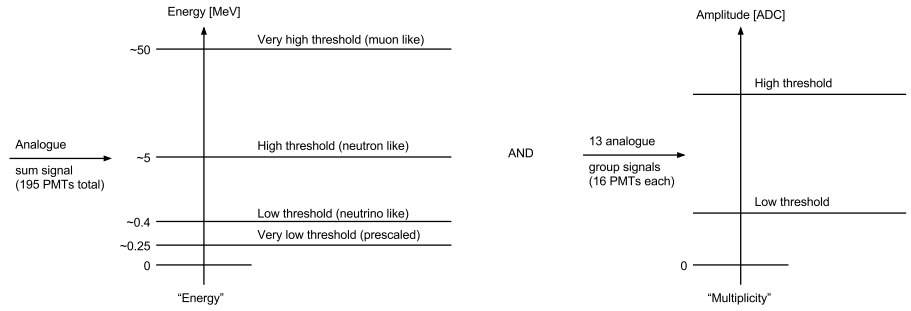

Figure 3.15: Showing the trigger decision principle of Double Chooz. The trigger decision is made from logical AND of the energy deposition in the detector and the multiplicity condition of number of active groups of PMTs [50].

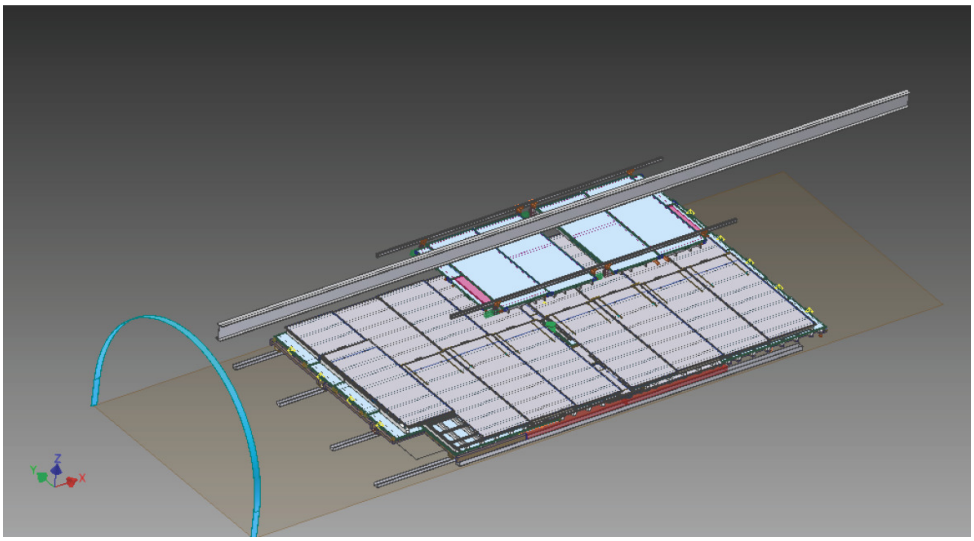

Figure 3.16: Drawing of the OV. The OV consists of the lower OV and upper OV. The chimney is indicated with the green cylinder, located at the center.

Each OV consists of two planes, which is made of 64 5 cm × 1 cm×320 cm or 360 cm scintillator strips. Two planes are piled perpendicularly, for making position reconstruction of the incoming muons to be possible. The OV plane is made of two layers having 32 strips. The offset between these layers is 2.5 cm. Through each of strip, 1.5 mm diameter wavelength-shifting fiber is threaded in a hole which is running through the strip. The fibers are connected to Hamamatsu H8804 multi-anode photomultiplier tube (M64) at one ends to detect scintillation light. Mirrors are attached to the other ends.

3.6 Data acquisition system

The Double Chooz data acquisition system (DAQ) consists of two independent systems [52]. We call the systems as the neutrino DAQ (NuDAQ) and the outer veto DAQ (OVDAQ). The NuDAQ manages the data acquisition of the ID and the IV, while the OVDAQ manages the data acquisition of the outer veto.

The NuDAQ consists of two parts: readout processors and an event builder processor. The readout processor runs on a VME controller on each flash ADC crate. Therefore, there are six readout processors in total for the inner detector and the inner veto channels. The processed data from the VME controllers are sent to the event builder processor via 10 Gbps local area network and merged there. The event builder processor is connected with run control and on-line monitor via TCP sockets.

The OVDAQ is an USB-based readout system. Its readout module is based on Maroc2 [53]. The module converts analog signals from 64 multi-anode PMTs of the outer veto into charges and hit times as digitized data. Then, the data is sent to the event builder and merged with data from the NuDAQ. The NuDAQ and the OVDAQ are controlled synchronically by a run control system. The matching of data from the NuDAQ and OVDAQ is carried out by using a 32 ns global trigger clock as a time-stamp which is provided by the trigger system. The run control system consists of run control server and run control GUI (Graphical User Interface). The run control server manges the data taking and its configuration information including such as run number, data taking time, and trigger condition. Here, the run number is an identifier for the "run", which means continuous data taking period. The signal data is serialized as ROOT [54] format and stored on hard disks, while the run information is stored in MySQL [55] database. The ROOT is a software framework and library for high energy physics developed and maintained by CERN. The MySQL is a widely used relational database management system (RDBMS). The run control GUI enables humans to interact with the run control system and take data from all over the world through network. A screen shot of the run control GUI is shown in Figure 3.17.

Furthermore, a monitoring system was developed for checking the data taking status remotely [56]. It is important for normal operation of the data taking.

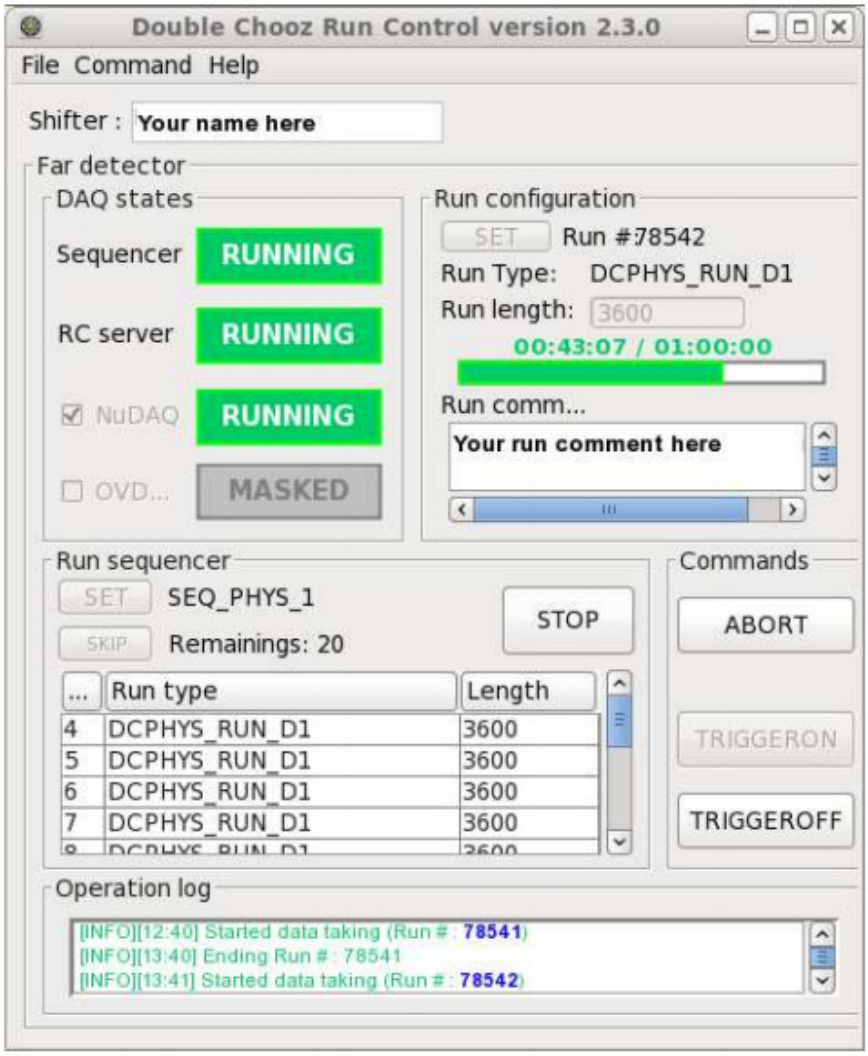

Figure 3.17: A screen shot of the run control GUI. Shifters (including on-site shifter and off-site shifter) use this graphical user interface to manage the data taking.

Chapter 4

Event reconstruction

4.1 Pulse reconstruction

As Double Chooz uses digitized waveform information, pulse reconstruction algorithms were developed for estimating the charge from the waveform inputs for each readout channel. The RecoPulse [57] is a tool to perform pulse reconstruction with a collection of algorithms.

The algorithms used in the RecoPulse consist of following components: 1) pedestal analyzer; 2) charge analyzer; and 3) time analyzer. These analyzers are used for estimating pedestal, time and charge respectively, as their names indicate.

The pedestal is a mean ADC counts in a baseline of a waveform. The number of time samples used to compute the pedestal can also be a parameter to determine if the pulse is signal or noise. Two algorithms to calculate the pedestal are developed. One is named "external baseline method" and another is named "floating baseline method". The external baseline method calculates the pedestal from a full time window (256 ns, 128 samples) of an external trigger event in absence of signal which is taken with a rate of 1 Hz. On the other hand, the floating baseline method calculates the pedestal for each waveform, which uses the first 20 ns samples in the waveform time window. Double Chooz uses both methods for the analysis because of their different advantages and disadvantages. The external baseline method can calculate a stable and robust pedestal because it is not affected by signal. However, the method is not valid for events after large signals such as muons because these kinds of events shift the baseline. Therefore, using the floating baseline method is more plausible for events after large signals. For the above reasons, Double Chooz uses the external baseline method primarily, however, if the event matches the condition which is determined as:

$$|\sigma_{\text{floating}} - \sigma_{\text{external}}| > 0.5 \text{ DUQ}, \tag{4.1}$$

the floating baseline method is employed for the case. Here, DUQ is a unit of integrated charge.

The charge of each signal waveform is calculated by time integration of the pulse amplitude in a given time window. Location of the time window is defined so as to maximize the integrated charge, and size of the time windows is fixed to be 112 ns which is almost half of the full readout window. Figure 4.2 shows the distribution of reconstructed charge for both data and MC.

The "time" means a location of a waveform in a 256 ns time window taken by the flash-ADC by a few definitions. It characterizes not only the location but also a shape of the waveform. The RecoPulse can define several kinds of timing. Following time definitions are used in the neutrino oscillation analysis in Double Chooz: start time; max time; and end time.

Figure 4.1 shows a schematic view of the time definitions. The start time is defined as the time where a signal pulse starting to rise up. The rising up time is defined where the amplitude exceeds 30 % of the maximum amplitude after subtraction of the pedestal. The max time is defined as the time where a point of maximum amplitude. The end time tells where he amplitude of the pulse is settled to a pedestal level, which is defined as the point where the amplitude reaches less than 20 % of the maximum amplitude is reached. Figure 4.3 shows a distribution of start time for the data and MC for 1 p.e. pulses. The data agree reasonably well with the MC.

A threshold level is laid down for ensuring that a signal is due to an actual PE. The threshold level is decided from pedestal spread (σ_{ped}) and time windows size (S) as:

$$Q_{\mathrm{min}} = n_{\sigma} \cdot \sigma_{\mathrm{ped}} \cdot \sqrt{S} \tag{4.2}$$

where n_{σ} is a value to determine the threshold. By default, $n_{\sigma} = 5$ is used.

Sometimes multiple pulses are found in a waveform. For this case, each of the pulse information, their summed charge, and number of pulses are stored.

4.2 Vertex reconstruction

Vertex information of an event is used for various purposes in the analysis. For example: neutrino selection; background estimation; and energy reconstruction.

Double Chooz has developed a tool for the vertex reconstruction which is based on maximum-likelihood algorithm assuming a point-like light source, and isotropic light propagation from it. The vertex reconstruction tool uses charge and hit time information for each PMT and the reconstruction is carried out by maximizing a likelihood function which is calculated from the following set of parameters:

$$\mathbf{X} = (x, y, z, t, \Phi), \tag{4.3}$$

where x, y and z represent the location of the light emission point, t is the event time, and Φ is the light intensity per unit solid angle (number of photons per sr). The likelihood

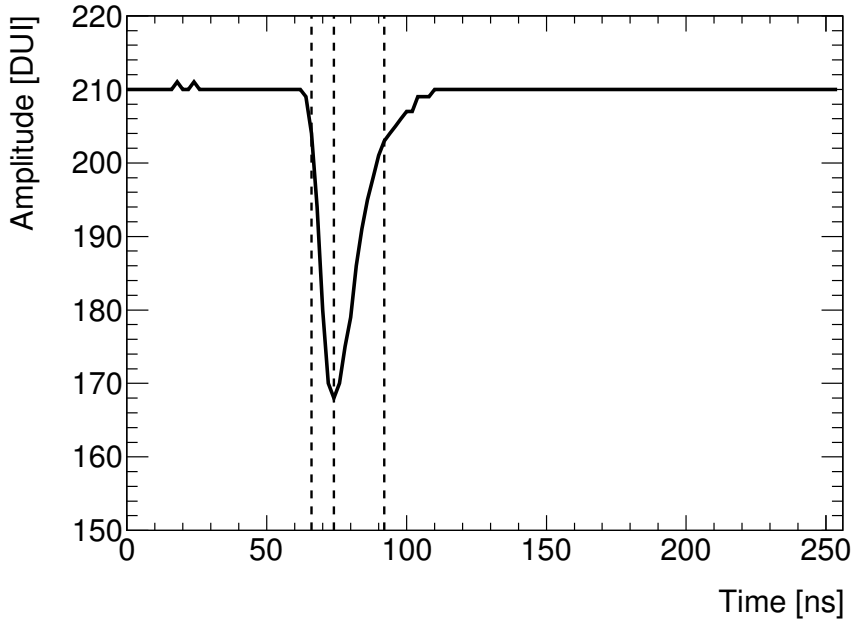

Figure 4.1: A schematic view of start time, max time and end time. The start time is defined as a time that pulse is starting to rise up, which is defined as 30 % of the maximum amplitude. The max time is defined as a time of maximum amplitude. The end time is defined as a time that pulse is settled to a pedestal level, which is defined as 20 % of the maximum amplitude. The start time, max time, and end time are indicated with dashed line from left to right, respectively.

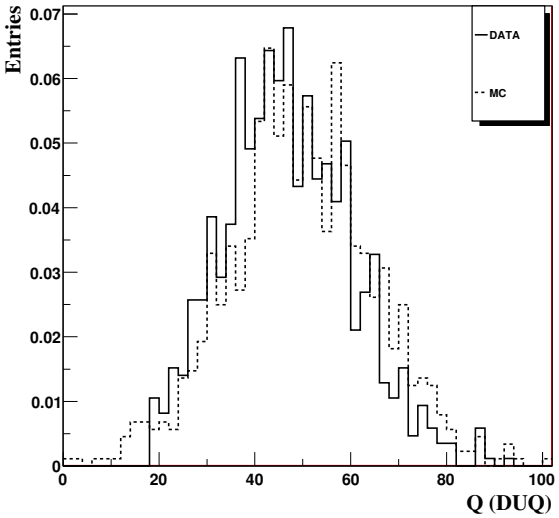

Figure 4.2: Distribution of reconstructed charge distribution with 1 p.e. inputs. The solid line indicates the actual data while the dashed line indicates MC.

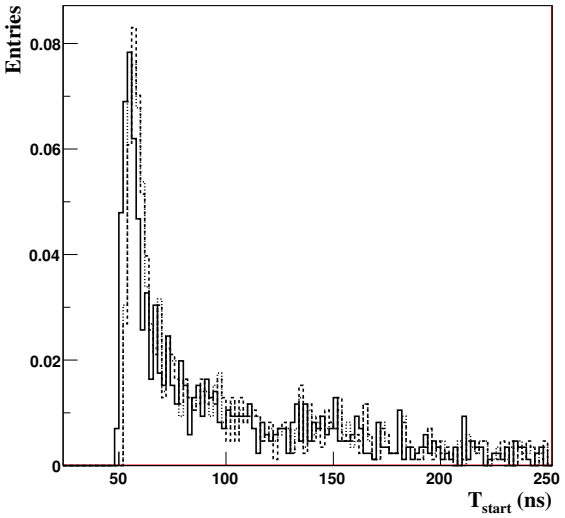

Figure 4.3: Distribution of reconstructed start time with 1 p.e. inputs. The solid line indicates the actual data while the dashed line indicates MC.

function is defined by the following equation:

$$\mathcal{L}(\mathbf{X}) = \prod_{q_i=0} f_q(0; q_i') \prod_{q_i>0} f_q(q_i; q_i') f_t(t_i; t_i', q_i') \tag{4.4}$$

q_i and t_i are measured charge and hit time (start time) for i-th readout channel, respectively. q_i' and t_i' are expected charge and hit time for each channel from a point-like light source. $f_q(q_i; q_i')$ is a probability distribution function (PDF) to measure a charge q_i with a given expected charge q_i'. $f_t(t_i; t_i', q_i')$ is a PDF to measure a time t_i with expected hit time t_i and a given expected charge q_i'. The PDFs were created with Monte Carlo simulation. Effective light attenuation and PMT angular response were tuned from source calibration data. Charge and time likelihoods are extracted from laser calibration data, and verifications were done by source calibration data and "physics data". The "physics data" is regularly taken data for observing neutrinos from reactors.

Vertex position can be estimated by maximizing the likelihood function $\mathcal{L}(\mathbf{X})$. It is equivalent to minimize the following negative log-likelihood function:

$$F_V = -\ln \mathcal{L}(\mathbf{X}) \tag{4.5}$$

$$= -\sum_i \ln f_q(q_i; \mathbf{X}) - \sum_{q_i>0} \ln f_t(t_i; \mathbf{X}) \tag{4.6}$$

The performance of the vertex reconstruction was evaluated with radioactive source deployment data. The spatial resolutions with different sources are: 29.6 cm for ^{137}Cs, 20.9 cm for ^{60}Co and 20.7 cm for ^{68}Ge.

The value F_V is also used for signal and background separation, because F_V tends to have a smaller value when a light emission is point-like, whereas, F_V tends to have a larger value when the light emission is spread in the detector.

4.3 Muon reconstruction

Double Chooz developed two muon track reconstruction tools called RecoMuHamID and FIDO [58]. Muon track is reconstructed using the observed charge and timing of PMTs in the ID and IV. In addition, FIDO uses OV hit positions. These two muon reconstruction algorithms are used to cross-check each other. The reconstructed muon track information is used for:

- Reduction of cosmogenic background such as ^{9}Li and ^{8}He, which are produced by muon interaction in the detector. These isotopes are produced on average at a distance of 500 mm to the muon track. This is the most important role of the muon reconstruction tool.

- Measurement of muon dE/dx in the detector. The value and the track information is correlated with cosmogenic isotope production which is one of the background sources.

- Study of cosmogenic isotope production due to stopping muons such as ^{12}B.
- Discrimination of single muon events and more complex events which have similar energy. For example, it is possible to distinguish IV passing through the upper corner of the IV from fast neutron interaction in the ID.
- Imaging of the detector. For example, muon events are used for photogrammetric survey of the OV.
- Timing calibration of all PMTs is also possible.

In Double Chooz, OV was not running in all of the data taking period. Therefore, FIDO is developed to work for both of the cases when OV is available or not. The reconstruction is carried out by calculating χ^2, which is calculated from difference of expected and observed signals. And the best track which minimizes the χ^2 is adopted as the track. In the algorithm, muons are assumed to be through-going and ultrarelativistic. If the muon seems to have stopped in the detector, an other reconstruction algorithm (which assumes that muon is stopped) is tested, and the algorithm which has better indication is chosen.

The muon reconstruction resolution by the FIDO is about 40 mm at the center of the detector, while it is larger by a factor of 2 at the top and bottom. In this case, a 30 GeV muon is used, which is the median muon energy in Double Chooz experiment. Figure 4.4 shows the resolution of the muon tracking using the FIDO, as a function of the z-axis of the detector.

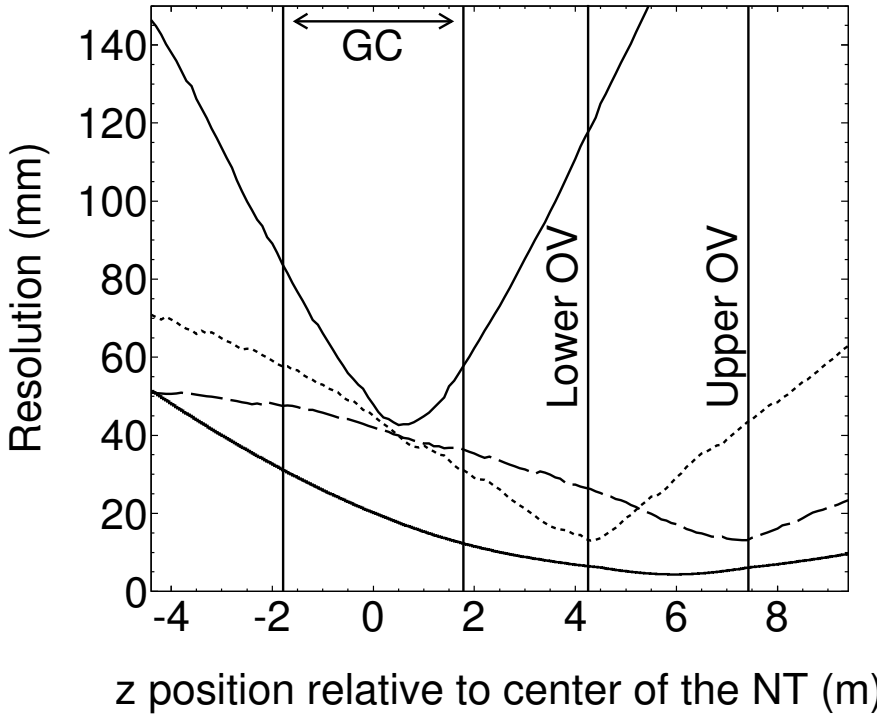

Figure 4.4: Muon track resolution with respect to z-axis [58]. The lower solid line shows the resolution with the OV, while the upper solid line shows without the OV. The dashed line shows the resolution with only the lower OV, while the dotted line shows with only the upper OV.

Chapter 5

Calibration system

Double Chooz employs a number of calibration systems for a precise measurement of neutrino energy, which is important for the precise measurement of θ_{13}.

In this chapter, the following calibration systems are explained:

- IDLI (Inner Detector Light Injection system)
- IVLI (Inner Veto Light Injection system)
- Laser calibration system
- Z-axis source deployment system
- Guide tube source deployment system

IDLI, IVLI and Laser calibration systems inject light into the detector. The IDLI and laser systems inject into the ID, while the IVLI injects into the IV region. IDLI system is used for ID PMT and electronics gain calibration which is referred to as linearized-PE calibration. It will be described in detail later in this chapter. IDLI system is also used for stability monitoring of timing offset of each readout channel. The laser calibration system is used for timing offset calibration for ID readout channel. Z-axis and guide tube source deployment systems are developed for deploying radioactive sources in the detector. These systems are used for various purposes such as energy calibration and efficiency studies and so on. Diffuser ball for the laser system is also deployed into the detector using the z-axis system.

Data is taken with the IDLI and IVLI once a week remotely for the calibration and stability monitoring. The other systems such as the laser system needs one to deploy manually insert the laser ball in the detector, so the data is taken only a few times a year.

5.1 IDLI

5.1.1 Overview of the system

Inner detector light injection (IDLI) is a system to inject LED light into the inner detector through optical fibers. University of Sussex [59] developed the system, and Tokyo Institute of Technology is responsible for its operation. The purposes of the system are the following:

- PMT and readout electronics gain calibration (linearized-PE calibration)
- PMT and readout electronics timing offset calibration
- Stability monitoring of the detector response and calibration constants

The gain calibration extracts a conversion factor of reconstructed charge into number of photoelectrons (p.e.). The timing calibration is a correction of hit timing for each readout channel. It is necessary because hit timing for each readout channel differs according to reasons such as difference of signal cable length from the PMT to electronics device. Laser calibration system is used for the timing offset calibration, however, the stability of timing offset of ID readout channels is measured using the IDLI system. Moreover, as well as the timing offset calibration, the laser system is used to estimate the speed of light in the detector. The estimated speed of light is used for the tuning of Monte-Carlo simulation parameters. Details of the calibrations using the IDLI system is described later.

Since the IDLI is an embedded calibration system with fixed light injection points inside the detector, it is possible to take the calibration data regularly by shifters through the network from all over the world. This enables us to monitor the stability of the detector response, such as readout gain and timing during the operation. This is important for Double Chooz which has been taking data for more than three years so far and plans to continue for several years. Unlike the deployment calibration systems which requires operation by experts on-site, operation of the IDLI system is fully automated by using the on-line system.

There are four components in the IDLI system: a pulser box, a control box, optical fibers and light injection points.

The pulser box contains LEDs which are connected with optical fibers. A picture of the pulse box is shown in Figure 5.2. The connector device is the golden pieces longitudinally arrayed at the middle in the picture. Figure 5.3 shows a schematic view of the connector device. There are three wavelengths of LEDs available: 385 nm, 425 nm and 470 nm. These LEDs have following features:

- The 385 nm wavelength light excite the scintillator fluid.

- The 425 nm and 470 nm light does not excite the scintillator fluid and is neither absorbed, so that it illuminates the opposite side PMTs.

These different wavelengths of LED light are used for different purposes of the detector response check or the calibrations. Mainly two wavelengths are used in the analysis. For the calibration purposes, 385 nm wavelength light is used for the gain calibration as it illuminates large number of PMTs by the isotropic light of re-emission, and 425 nm wavelength is used for timing calibration as we need to subtract the flight of photons for timing calibration. A PIN photo-diode is attached in the connector device of the LED and the optical fiber, which allows one to monitor the light intensity, also shown in Figure 5.3. However, as we found the fluctuation of PIN photo-diode is larger than the variation of total charge observed in the detector, we used total charge to monitor the stability.

The optical fibers are transparent for passing LED light into the detector. One side of the optical fiber is connected to the pulser box and the other end is fed into the inner detector through a pipe together with PMT cables, and attached to the light injection point on a PMT frame.

The light injection point is a device to fix the optical fiber on the PMT frame. There are two types of injection points: "diffused" and "pencil". Injected light from the diffused and pencil light injection points are called "diffused light" and "pencil light" respectively. The diffused light injection point equips an optical diffuser, so that the incident light spread in the detector with an angle of about 22 degrees (half-cone angle). On the other hand, the pencil light injection point does not equip the diffuser. Therefore, the light injects directly from the optical fiber into the inner detector. The spread of the pencil light is about 7 degrees as a measure of the half-cone angle. Different materials are used for the optical fibers for the diffused point and the pencil point: poly-methyl methacrylate (PMMA) and quartz for the diffused and the pencil respectively.

Among the 32 diffused light injection points, 6 are attached on the top and bottom (12 in total), and 20 are attached on the wall of the ID. All of the diffused light injection points are directed toward the center of the detector. Therefore, whole detector wall can be illuminated at least by one diffused light injection point. In addition, there are 14 pencil light injection points. All of the pencil light injection points are attached on the wall of the detector directed horizontally to the PMT on the opposite side, which is not like the case of the diffused light injection points. Therefore, some of the light path cross the neutrino target, gamma catcher and buffer region while some other paths cross only the buffer of the gamma catcher and buffer regions. This enables us to use the pencil light injection points for investigating the stability of the liquid scintillator separately. Especially it is important to check the stability of the neutrino target which contains gadolinium, because CHOOZ experiment had a problem with the stability of the liquid scintillator with gadolinium. An illustration of the layout of the light injection points is shown in the figure 5.1.

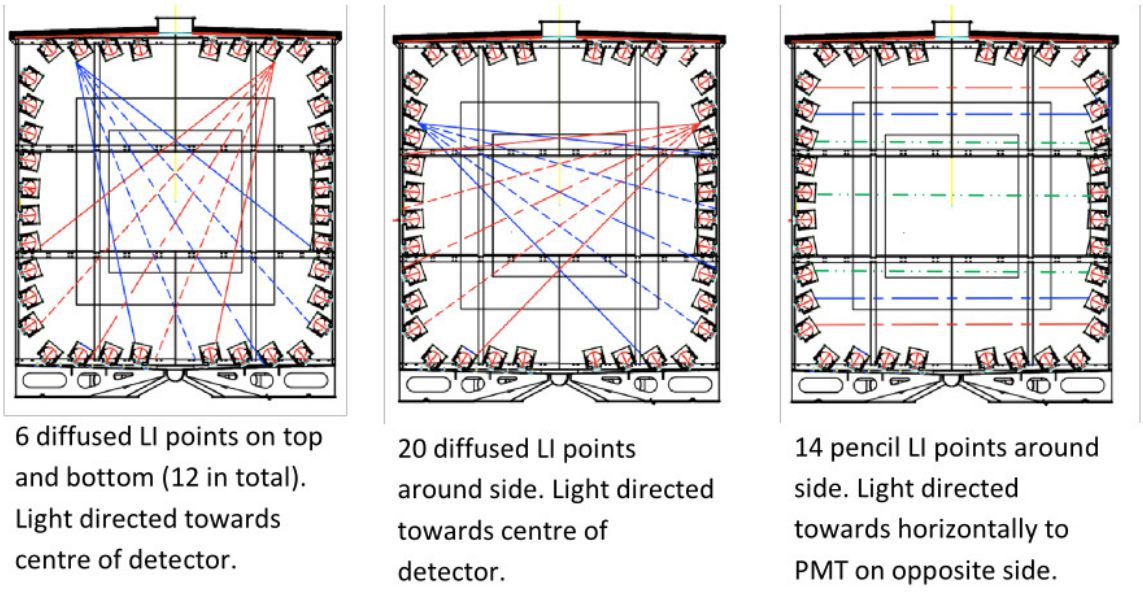

Figure 5.1: Layout of the IDLI light injection points [59]. The left and center figures show the diffused light emission, and the right figure shows the emission of pencil beams.

The control box manages operation of the IDLI system. A picture of the control box shown in Figure 5.4. The control box sends signals to the pulser box and the trigger board synchronously. When the signal is sent from the control box to the pulser box, the pulser box emits LED light. At the same time, the trigger board receives the external trigger, which prompts the data to be taken. In addition, the trigger signal is sent to a channel of the flash ADC, therefore it makes it possible to measure the timing of the trigger signal precisely with less than 1 ns precision. An example of the trigger signal from the control box is shown in Figure 5.5.

5.1.2 Time property

Examples of waveforms taken with the LEDs used for the IDLI system is shown in Figure 5.6. These data were taken with high light intensity. The three different LED lights have different time properties. In case of the figure shown, the full width half maximum (FWHM) for the 385 nm and the 425 nm LEDs are around 15 ns, while that for the 470 nm LED is 150 ns.

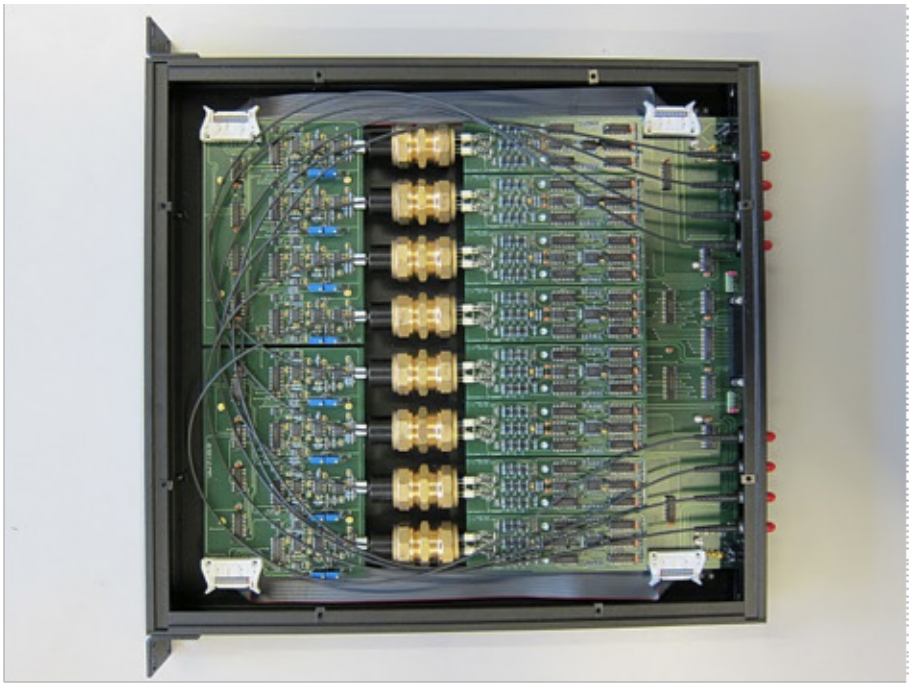

Figure 5.2: Picture of the IDLI pulser box. The LEDs are contained in the golden device.

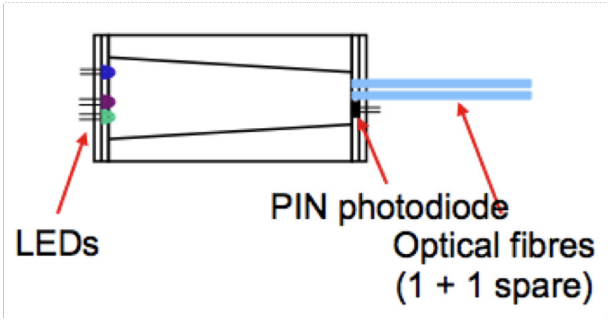

Figure 5.3: A connector of the LEDs and the optical fibers. Three LEDs with different wavelengthes and the two optical fibers are attached. One of the optical fibers is used as a spare. [59]

Figure 5.4: Picture of the IDLI control box. The IDLI system is operated through the control box.

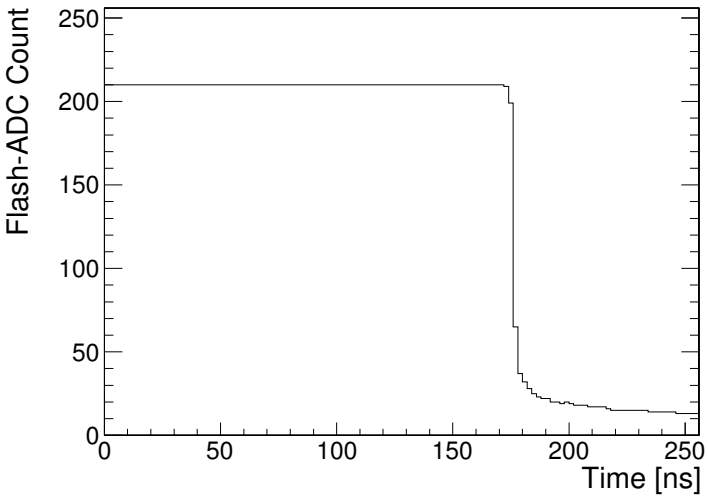

Figure 5.5: A waveform of the IDLI trigger signal

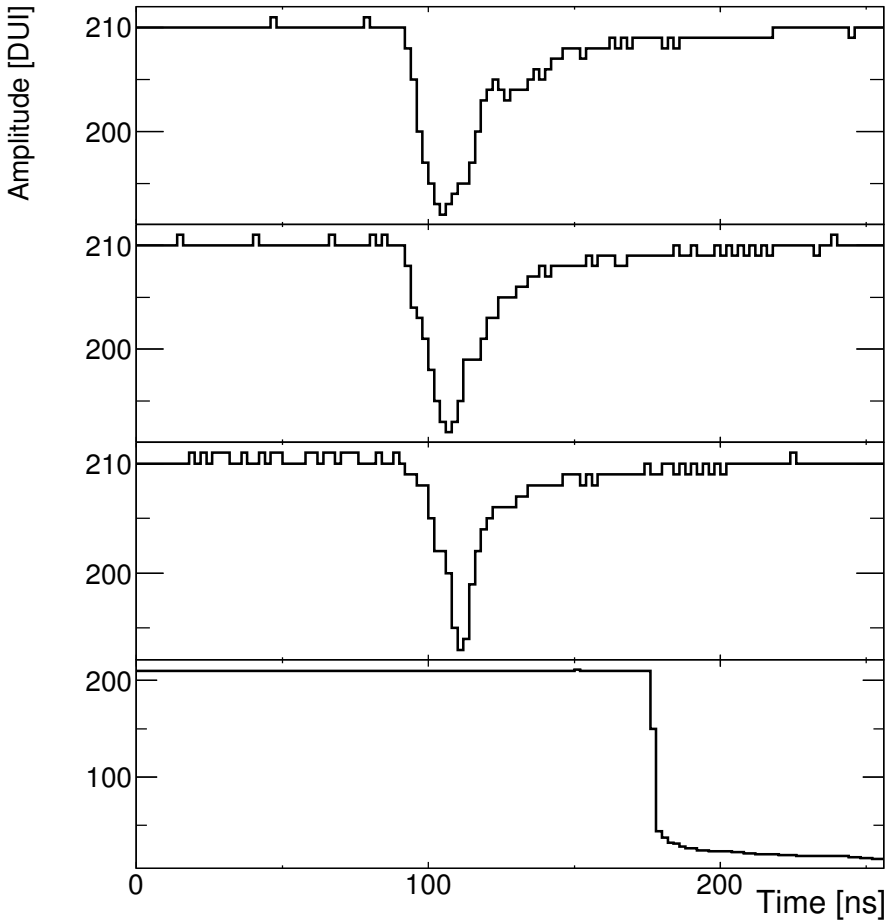

Figure 5.6: Examples of waveforms taken with the LEDs used for the IDLI system. The three waveforms from top to bottom are waveforms taken with the IDLI. The bottom waveform is the external trigger signal which comes from the trigger board, and the information is used for timing calibration.

5.1.3 Observed data taken with IDLI

5.1.4 Pulse shape

Examples of pulse shapes recorded by the flash-ADCs taken with the IDLI are already shown in Figure 5.6. Waveforms of all readout channels were checked and confirmed that pulses are within the time windows of the flash-ADC. Also, the trigger signal from the control box is shown in the bottom of the figure. Trigger signal is used to adjust fluctuation of the position of the signal in the flash-ADC time window due to 16 ns trigger clock. It is especially important for timing offset calibration, which will be described later.

5.1.5 Event display

The charge distribution patterns for all light injection points were checked using event display. It was checked if the light injection points are allocated to proper locations. Figures 5.7 and 5.8 show examples of events taken with the IDLI with 425 nm and 385 nm wavelength diffused light, respectively. Since the 425 nm wavelength light penetrates scintillation liquid in the ID, the opposite side PMTs are illuminated. On the other hand, the 385 nm wavelength light excites the scintillation liquid in the GC near the light injection point, so the PMTs near the light injection point is illuminated from the scintillation light.

5.1.6 Intensity

It is possible to configure the light intensity of the IDLI system by setting input intensity using software developed for controlling the IDLI system. Figure 5.9 shows the charge distribution for a readout channel with different input light intensity values.

5.2 IVLI

IVLI (Inner Veto Light Injection) system was developed to calibrate the IV detector. Similarly to the IDLI system, the IVLI system injects light into the IV to illuminate IV PMTs. The IVLI system is used for IV PMTs and electronics gain and timing calibration. Also, the system can be used for monitoring purposes such as parameters of IV PMTs, light yield of the IV liquid scintillator, and so on.

The IVLI system equips 96 LEDs, of which 6 are 365 nm wavelength and the others are 475 nm. 475 nm wavelength light is used for PMT and electronics gain calibration and monitoring of the PMT properties, while the 365 nm wavelength light is used to monitor the light yield or other properties of the liquid scintillator.

The LED is connected with quartz fiber through a connector, and the fiber is attached on the PMTs. At least one fiber is attached to all 78 IV PMTs.

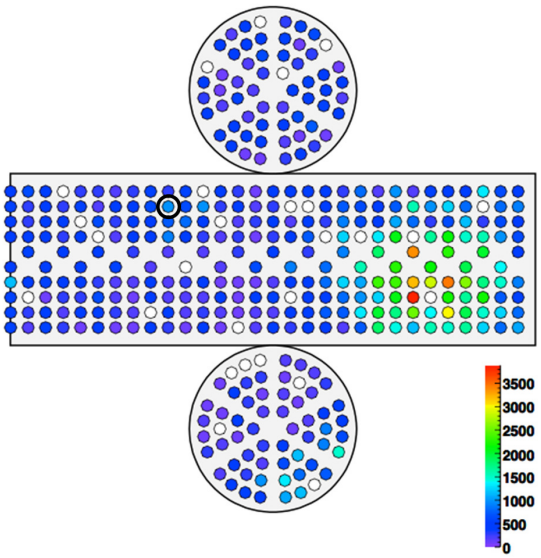

Figure 5.7: Event display of an event taken with IDLI system from a 425 nm wavelength diffused light injection point. Colored circles in the figure are locations of PMTs in the ID and the color represents amount of observed charge. Light injection point is marked with black circle in the figure.

5.3 Laser calibration system

Laser calibration system illuminates the ID PMTs through a diffuser ball in the NT through an optical fiber. A picture of the diffuser ball is shown in Figure 5.10. The ball is an 80 mm diameter sphere. The ball is deployed inside the NT along the vertical axis using the z-axis fish line system described in section 5.4, and when the ball is illuminated, the diffused light spreads in the detector. There are two types of the balls: one is used with 380 nm laser while the other is used with 470 nm laser. The ball for the 380 nm wavelength laser is filled with scintillator liquids. The mixture of the liquid is the same as the scintillation mixture which is used in the NT. The ball for the 470 nm wavelength laser is filled with GE silicon sealant gel. The material is chosen to satisfy anisotropy of light to be less than 5 % level.

The system is used for timing offset calibration of the readout system in the ID, tuning of the vertex reconstruction algorithm described in the section 4.2, investigation of optical properties of liquids in the ID, and so on. The laser system is capable to correct the timing offset for each channel within 0.15 ns time resolution.

470 nm blue laser and 380 nm ultra violet laser are prepared for the different purposes of the calibration. The 470 nm blue laser is used for the timing offset calibration, while the 380 nm ultra violet laser is used for study of the PMT and readout electronics gain.

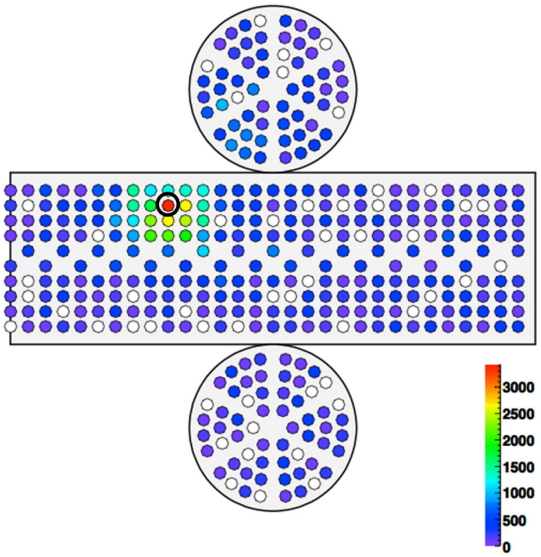

Figure 5.8: Event display of an event taken with IDLI system from a 385 nm wavelength diffused light injection point. 385 nm wavelength light excites the scintillator in the GC region near the light injection point. The illumination of scintillation light can be seen in the figure.

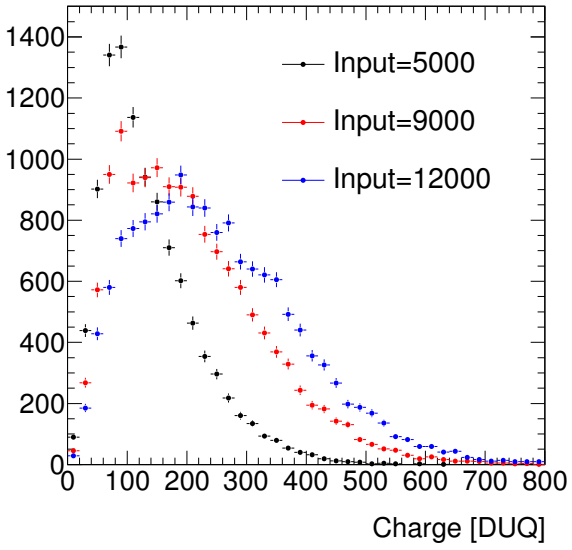

Figure 5.9: Charge distribution for a readout channels with different IDLI input intensities. The "input" in the legend is input value of light intensity for the IDLI. Higher charge is observed with higher input value.

Figure 5.10: Picture of diffuser ball.

Table 5.1: Calibration sources deployed in the detector

Source	Particle	Deposited energy [MeV]
^{137}Cs	γ	0.662
^{60}Co	γ	1.17, 1.33
^{252}Cf	Neutron	2.2 (n-H), 8.9 (n-Gd)
^{68}Ge	β^+	1.022

5.4 Z-axis fish line

The z-axis fish line is developed for the precise calibration of the Double Chooz detector. The radioactive sources are capsuled and inserted into the ID through the chimney from above the detector. The capsule is deployed vertically inside the detector as shown in Figure 5.12. The system is used not only for the deployment of radioactive sources, but also it is possible to deploy the LED flasher and laser ball as well. The system is used for absolute energy scale determination including position dependence along the central axis of the detector. Moreover, by deploying a neutron source (^{252}Cf) inside the NT, it is possible to evaluate detection efficiency of neutron captures which is basically equivalent to the delayed signal of inverse beta decay signal of reactor neutrino.

The system consists of a stepper motor, a deployment cable, and an acrylic weight. The material of the deployment cable is stainless steel and coated with FEP-Teflon to avoid the stainless steel to be exposed to the liquids in the detector. The deployment cable is mounted on a guide pulley and a position encoder is equipped on it, so that it is possible to determine the location of the capsule to be deployed in the detector. The z-axis fish line system can place the calibration source along the z-axis. The picture of the stepper motor is shown in Figure 5.11.

Calibration sources deployed inside the detector are summarized in Table 5.1.

5.5 Guide tube calibration system

The guide tube system is used to determine the absolute energy scale and its position dependence in the GC region. Furthermore, the system is also used to investigate the fraction of neutrons which enter to the NT from the GC.

The system consists of a L shaped pipe which are running between the NT and GC vessels as shown in Figure 5.12. Radioactive sources are capsuled and attached to a wire, and inserted into the GC through the pipe.

Figure 5.11: Stepper motor.

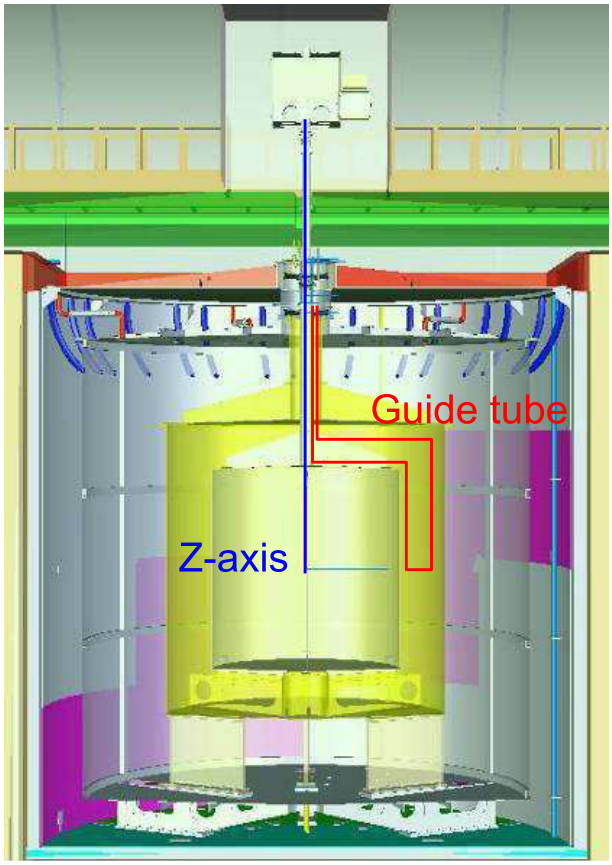

Figure 5.12: Paths of z-axis fish line and guide tube. The blue line shows the path of the z-axis fish line. The red line shows the path of the guide tube.

Chapter 6

Detector and energy calibration

6.1 Timing offset calibration

Double Chooz uses 390 readout channels in the ID for neutrino observation. Even if all PMTs observe signals simultaneously, the hit timings are different by channel because of the different length of cables and different response of readout electronics. This fact motivates the timing offset calibration for adjusting hit timing for all readout channels. It is especially important for the vertex reconstruction, which requires good precision of hit timing for good spacial resolution of the reconstructed vertex position.

Timing offset calibration is carried out primarily using the laser system. In addition, IDLI system is used for stability monitoring of timing offset for each channel. Both of the methods will be explained in this section.

6.1.1 Timing offset calibration using the laser system

Timing offset for each channel is calculated using the laser system by placing the laser ball at three different positions in the detector: $z = -92$ cm, 0 cm, and $+92$ cm along the central z-axis.

The first procedure is to estimate effective speed of light in the detector using the relationship between the hit time and distance from position of the laser ball. Since we have no knowledge about the relative timing offset for each readout channel at this point, the effective speed of light c_n was calculated by assuming the all timing offsets to be zero, and measured to be $c_n = 20$ cm/ns.

Next, the timing offset for each channel is calculated by subtracting the estimated hit time from the c_n and the distance between the PMT and the location of the laser ball.

The laser source cannot be deployed regularly, so stability of the timing offset is monitored by data taken with the IDLI system as it is described in the next section.

6.1.2 Timing offset calibration using the IDLI system

In this method, the timing offset is calculated from relationship between the subtracted time ($T_{\rm sub}$) and distance between the light injection point and the PMT:

$$T_{\rm sub} = T_{\rm max} - \frac{v}{d^{ij}} - T_{\rm trig}, \tag{6.1}$$

where $T_{\rm max}$ is maximum time as defined in section 4.1, v is speed of light in the detector, and d_{ij} is the distance between i-th PMT and j-th light injection point. $T_{\rm trig}$ is the timing of the trigger signal which is defined as start time of the rectangularly shaped trigger signal. The reason why the max time is used is because it was studied using Monte-Carlo that the resolution of the timing offset measured with the max time is better than that with the start time. The $T_{\rm sub}$ is defined as the hit time subtracted by $T_{\rm trig}$ which cancels out event-by-event trigger to light emission timing difference. Ideally, the $T_{\rm sub}$ and the distance between the PMT and the light injection point has linear relationship, therefore it can be represented by following equation:

$$d^i = vT^i_{\rm sub} + b^i, \tag{6.2}$$

where d^i is the distance between the PMT of i-th readout channel and the light injection point, v is effective speed of light in the detector, T^i is the $\rm T_{sub}$, and b^i is an offset.

Eight light injection points are used for the timing offset calibration. Two light injection points are attached on the top, four are on the wall, and two are on the bottom of the ID. These light injection points are selected so as to all PMTs to be illuminated from at least one of the eight light injection points. Light incident angle to a PMT is preferred to be as perpendicular as possible, so the best light injection point for all PMTs are decided from the geometry of the light injection points and the PMTs.

Diffused light injection points are used for the timing calibration to cover all PMTs with minimum sets of calibration data. Wavelength of 425 nm (which does not illuminates the scintillation liquid) is used, because one needs to know precisely the relationship between the length of a PMT to a light injection point and photon's flight time in the detector. If 380 nm wavelength (which illuminates the scintillation liquid) is used, one cannot know the vertex of light emission precisely, therefore it is not appropriate for the timing offset calibration. In addition, time profile of light re-emission needs to be considered with 380nm wavelength and therefore not suitable for time offset calibration.

The first step of the timing offset calibration is to estimate the $T_{\rm sub}$ for each readout channel. As the trigger signal is provided from the trigger system which judges the trigger condition with 16 nsec clock, there is event-by-event time fluctuation in 16 nsec which is large compared to the required time offset calibration for the vertex reconstruction. The trigger signal is recorded by a particular readout channel using the flash-ADC. Therefore, it is possible to subtract the trigger timing from the hit timing for each readout channel, so the event-by-event timing variation can be canceled out. The trigger signal is a square

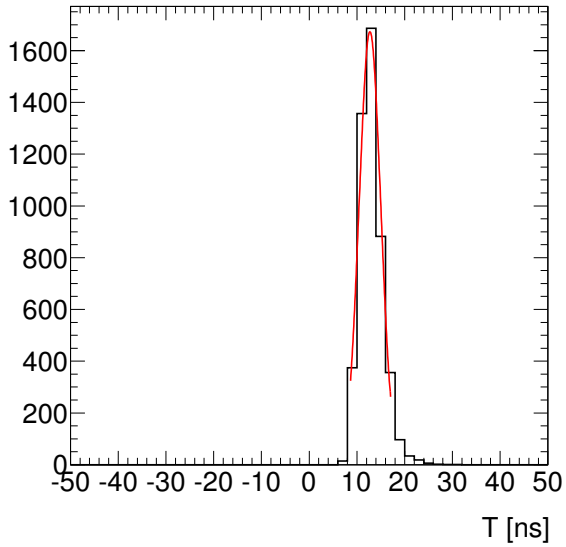

Figure 6.1: Distribution of $T_{\rm sub}$ for a channel. The data is taken with the IDLI system. $T_{\rm fit}$ is extracted by fitting with Gaussian from the distribution.

wave which follows NIM (Nuclear Instrumentation Module) standard which is shown in Figure 5.5. The timing can be precisely determined from the edge of the signal.

Figure 6.1 shows the distribution of $T_{\rm sub}$ taken with the IDLI system. In this case, the $T_{\rm sub}$ distribution has about 4 ns variation. To eliminate the effect of the variation, fitting by Gaussian was done to calculate the timing offset. In this thesis, the timing extracted by the fitting is called as $T_{\rm fit}$.

Next, the effective speed of light in the detector is estimated by a linear fitting to the scatter plot of the distance between the light injection point and PMT versus $T_{\rm fit}$. Since the relative timing of the trigger pulse and light emission is different for each light injection point, effective speed of light and offset are estimated independently for each light injection point using the function defined by Eq. 6.2. The mean of all values is used for timing offset estimation, to improve the precision and robustness of the estimation. Furthermore, the offset for each light injection point is calculated again with the derived effective speed of light. Figure 6.2 shows the relationship between the distance and the $T_{\rm fit}$. In this figure, the linear tendency is seen. The residual fluctuation is considered as originating from the timing offset.

Finally, the timing offset for each channel is estimated by the estimated speed of light and offset for each light injection point. The same speed of light is used for all light injection points, while the offset is subtracted for each light injection point. The distribution of the timing offset is shown in figure 6.3.

Channel to channel comparison of the timing offset with the laser method is shown

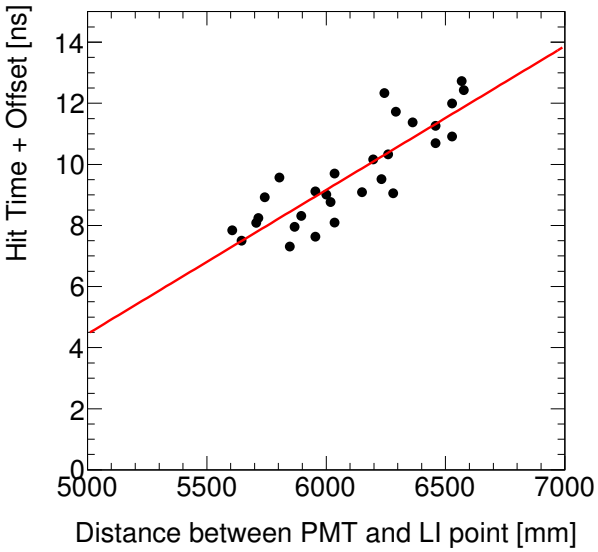

Figure 6.2: Distance between the light injection point and PMT versus T_{fit}. Each point corresponds to each run (with different LED intensity and location). Red line drawn in the figure is a regression line. Speed of light in the detector can be calculated from the regression line, which will be used for the calculation of the timing offset.

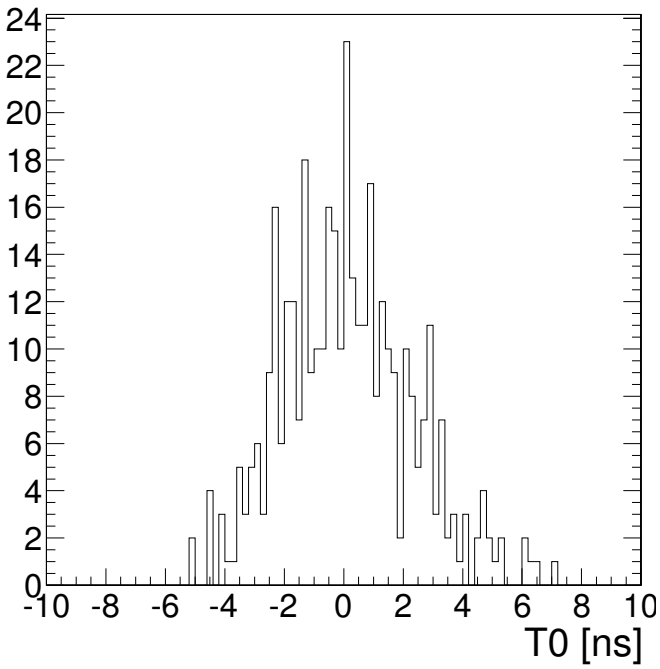

Figure 6.3: Distribution of timing offset for all channels.

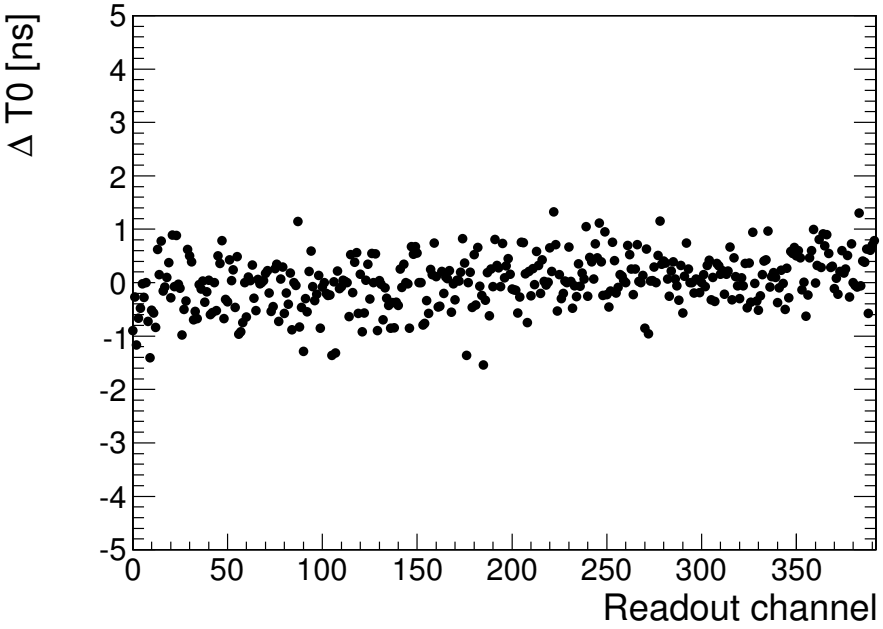

Figure 6.4: Channel by channel comparison of timing offset for the laser and IDLI method. X-axis indicates the readout channel. Y-axis shows the difference of T0 obtained from the laser method and IDLI method.

in Figure 6.4 and its distribution is shown in figure 6.5. The difference between the two methods introduced is 0.48 ns, which is consistent within the precision.

Stability of the timing offset is monitored using the IDLI data. Figure 6.6 shows the stability of the timing offset for some readout channels. This result shows that the stability of the timing offset is stable in less than 1 ns.

6.2 Overview of energy reconstruction

In Double Chooz, visible energy is reconstructed by several calibration steps. First, the observed integrated charge is converted into number of photoelectrons (which is emitted at the photo-cathode of the PMT). Then, using the derived number of photoelectrons (N_{pe}^{m}, where m means data or Monte-Carlo), uniformity calibration, absolute energy scale calibration, stability calibration, and energy non-linearity calibration are applied to reconstruct the visible energy. The formula of the visible energy reconstruction is expressed by following equation:

$$E_{\mathrm{vis}} = N_{\mathrm{pe}}^{m} \times f_{\mathrm{u}}^{m}\left(\rho, z\right) \times f_{\mathrm{MeV}}^{m} \left(\times f_{s}^{\mathrm{data}}\left(E_{\mathrm{vis}}^{0}, t\right)\right) \left(\times f_{\mathrm{nl}}^{\mathrm{MC}}\left(E_{\mathrm{vis}}^{0}\right)\right). \tag{6.3}$$

In the equation above, $f_{u}^{m}\left(\rho, z\right)$ represents the uniformity calibration. m indicates the data or Monte-Carlo. The parameters ρ and z represent the vertex position in the cylin-

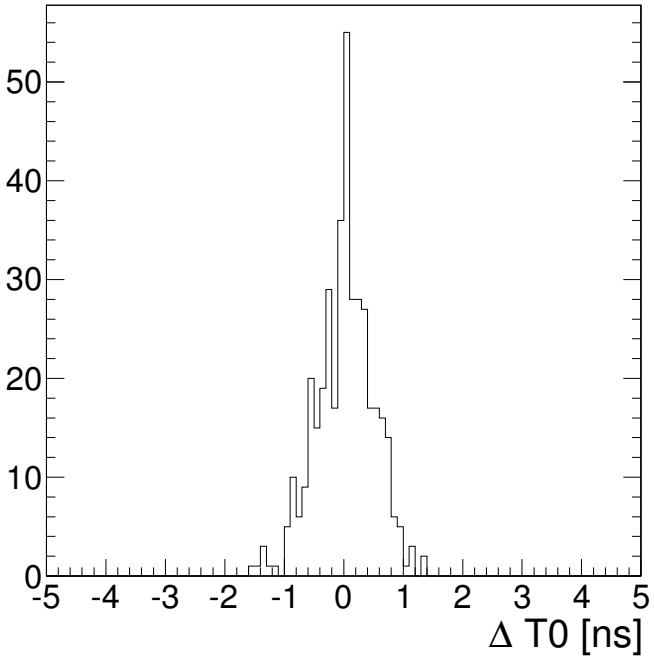

Figure 6.5: Distribution of the T0 difference between the laser and IDLI method. Each entry is the difference of T0 obtained from the laser method and IDLI method for a readout channel. The variance (RMS) of the distribution is calculated to be 0.48 ns.

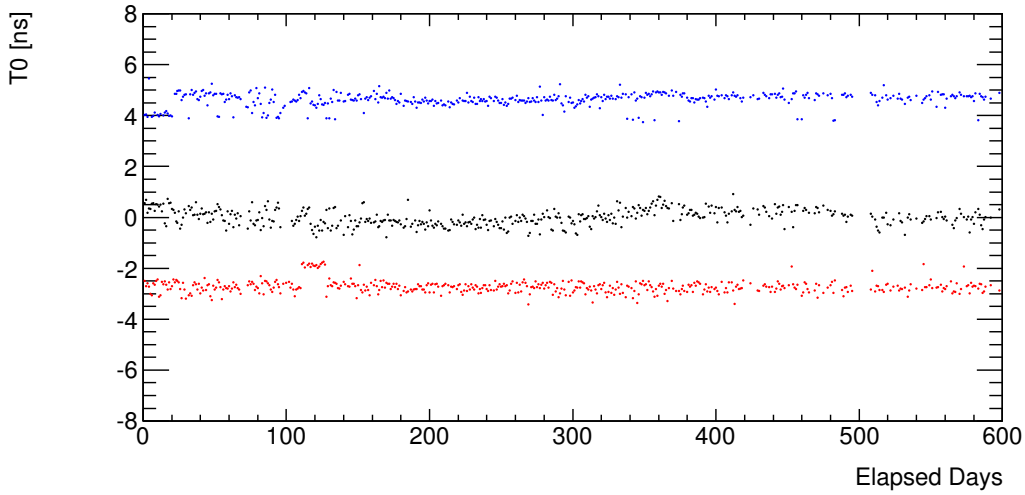

Figure 6.6: Stability of the timing offset for some channels. Stability of all channels were checked using the IDLI system.

drical coordinate, where z is measured along the vertical axis in the center of the detector, and ρ means the radial distance from the z-axis. The calibration is applied for reducing the position dependence of the detector response.

f^m_{MeV} represents the absolute energy scale calibration. It is a constant conversion factor from the number of photoelectrons to MeV scale. Obtained energy after these three calibrations (the linearized-PE calibration (section 6.3), uniformity calibration (section 6.4), and absolute energy scale (section 6.5) calibration) applied is denoted as E^0_{vis} for convenience. $f^{\mathrm{data}}_s\left(E^0_{\mathrm{vis}}\right)$ represents the time stability calibration, which is applied only to the data as the time variation of detector response is not considered in the Monte-Carlo. Finally, the term $f^{\mathrm{MC}}_{\mathrm{nl}}\left(E^0_{\mathrm{vis}}\right)$ means the energy non-linearity calibration. It corrects for the difference of energy non-linearity between the data and the Monte-Carlo. The calibration steps above will be explained one by one in the following sections.

6.3 Linearized-PE calibration

The linearized-PE calibration is aimed to correct for the flash-ADC non-linearity channel by channel. The linearized-PE calibration determines conversion of the integrated charge by pulse reconstruction (section 4.1) into the number of photoelectrons. The conversion factor vary with respect to charge (which is referred as non-linearity), so the linearized-PE calibration takes into account the charge dependence of the conversion factor.

The most prominent part of the non-linearity is considered to originate from properties of the flash-ADCs. In addition, the pulse reconstruction algorithm is considered to introduce the non-linearity. The non-linearity by the properties of flash-ADC can be categorize by two components [49]. As it was described in the detector chapter, these two non-linearities are called differential non-linearity (DNL) and integral non-linearity (INL). The DNL is a deviation of step-by-step ADC value while the INL is a deviation of ADC value with respect to input voltage originating from the DNL.

Data set used for the linearized-PE calibration is taken with the IDLI system. The wavelength is 385 nm diffused light, so the incident light illuminates the scintillation liquid in the GC region, and the re-emitted light is detected by the PMTs. For each data, light intensity is constant. However, since the gain varies with respect to the integrated charges, the data is taken with different configurations of light intensities. Eight light injection points with different locations are used for this calibration. In total, about 50 sets of data with different configurations are used.

Formula of the conversion can be written as follows:

$$N_{\mathrm{pe}} = \sum_i \frac{q_i}{g_i\left(q_i, t\right)}. \tag{6.4}$$

The left term N_{pe} is number of photoelectrons. In the right term, i means readout channel, q_i is the integrated charge for the i-th channel, and $g_i\left(q_i, t\right)$ is the conversion factor which

is called gain in this section.

The gain is estimated using the following relationship:

$$g_i = \alpha \times \frac{\sigma_i^2}{\mu_i}, \tag{6.5}$$

where μ_i is a mean charge for each IDLI configuration, and σ_i is the standard deviation (RMS) of the observed charge distribution for the i-th readout channel. α is a parameter to correct for the small deviation of the gain determined from Poisson statistical fluctuation, σ^2/μ. Details of derivation of the equation is explained in appendix A. The parameter α is assumed to be the same for all readout channels in this calibration technique. The value of α is determined using PMT hit multiplicity. The idea of the determination of the α is to make observed number of p.e. (which is calculated by Eq. 6.4) to be equal to the PMT hit multiplicity. When the light yield is small enough, most of the PMTs should observe single p.e.. Thus, total PMT hit multiplicity should be equal to the number of p.e.. However, the PMT hit multiplicity is not used as it is, because even with small light yield, some of the PMTs observe more than one p.e. due to statistical fluctuation. To take into account for the multi p.e. contribution, Poisson corrected number of PMT hits is introduced which is determined as:

$$n = -N_{\mathrm{PMT}} \ln\left(1 - \frac{N_{\mathrm{hits}}}{N_{\mathrm{PMT}}}\right), \tag{6.6}$$

where n is the Poisson corrected number of PMT hits, N_{PMT} is the number of the active PMTs, and N_{hits} is the observed PMT hit multiplicity. Derivation of the Poisson corrected number of PMT hits is described in appendix B. Using the Poisson corrected number of PMT hits, the α can be determined by the following equation:

$$n = N_{\mathrm{pe}}. \tag{6.7}$$

Figure 6.7 shows the gain as a function of the integrated charge for an example readout channel. Each point shows each measurement of the gain with different configuration of the light injection point and the input intensity. In the linearized-PE calibration, the gain is represented by a function which consists of two lines, represented by three parameters, namely: slope, intersection, and g0, respectively. As it is clear in Figure 6.7, the function consists of two lines one of which reproduces the variation of gain with respect to the integrated charge, while the other represents the constant gain given by g0 above the intersection point. The gain varies with the integrated charge at small charge below the intersection due to non-linearity, while the effect becomes negligible at higher charge region. The rate of the increment (or decrement) is defined by the slope. Also, integrated charge versus number of photoelectrons curve is shown in Figure 6.8.

Figure 6.9 shows the g0 for each readout channel and its distribution from all readout channels. Furthermore, Figures 6.10 and 6.11 show the slope and intersection.

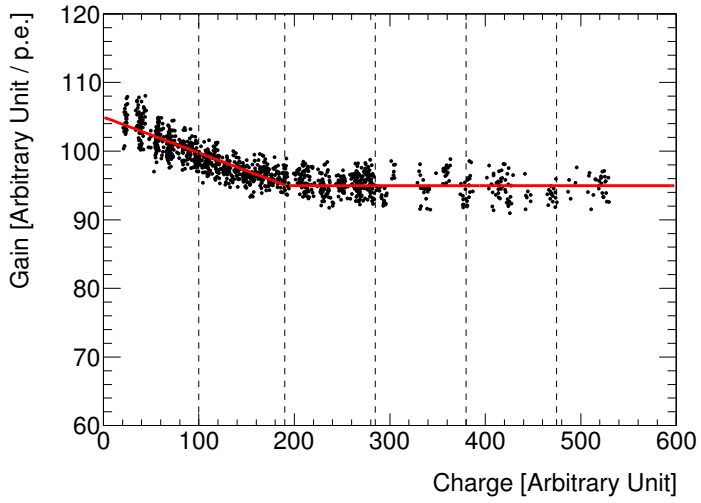

Figure 6.7: The gain as a function of the integrated charge for a readout channel. Black points are the measured gains using the IDLI system. Each point is taken with different configuration (light injection point and intensity). Red curve is the gain function parameterized with three parameters: slope, intersection and g0. The curve is obtained by regression analysis using ROOT [54]. The five dashed lines indicate the charges for 1p.e., 2p.e., 3p.e., 4p.e., and 5p.e., respectively from left to right.

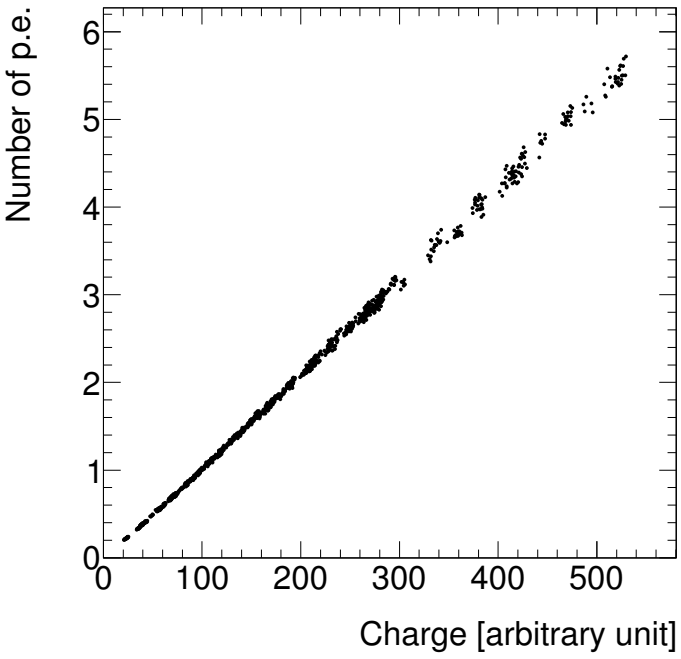

Figure 6.8: Integrated charge versus number of photoelectrons.

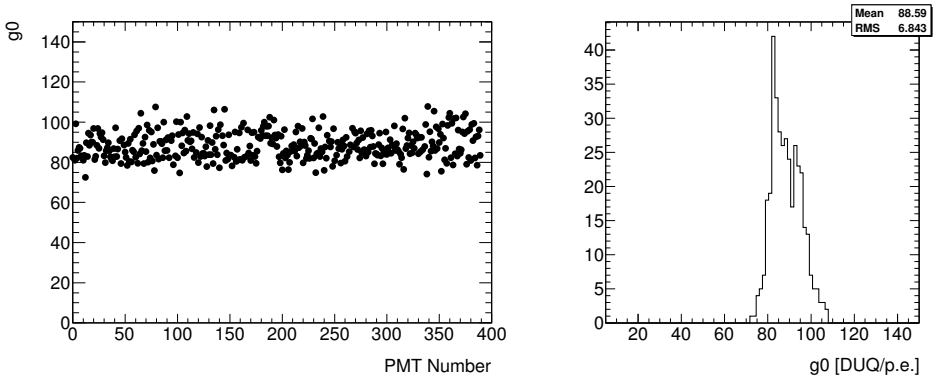

Figure 6.9: Measured g0 versus PMT channel (left). Distribution of measured g0 for all ID readout channels (right). In this case, mean of g0 is measured to be 88.59 and spread (RMS) is 6.843. Therefore, relative spread can be calculated as 7.72%.

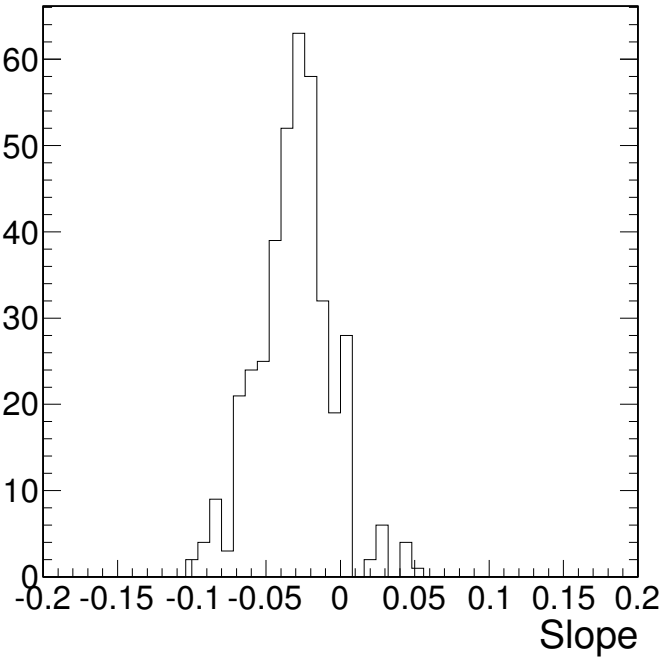

Figure 6.10: Distribution of slope from all readout channels.

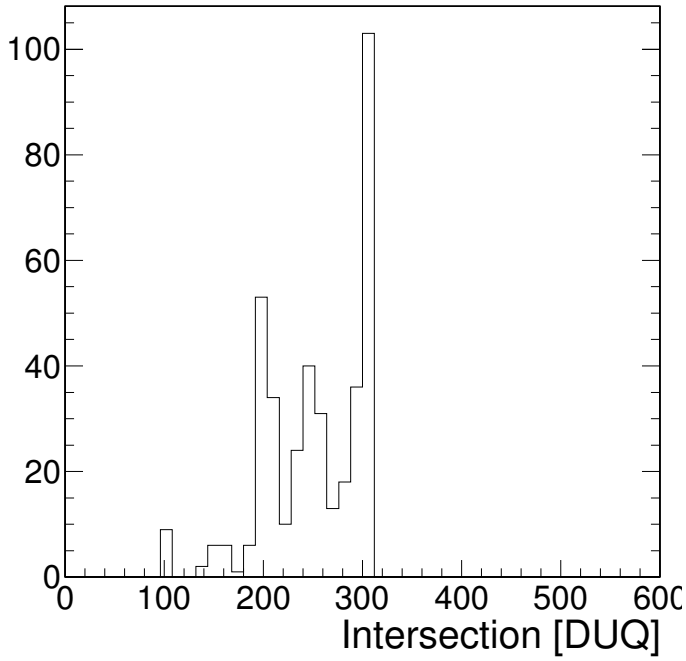

Figure 6.11: Distribution of intersection from all readout channels.

In the same way, the linearized-PE calibration is also applied to the Monte-Carlo simulation, since Double Chooz simulates the PMT and electronics including the flash-ADC, so the gain non-linearity is introduced similarly to the observed data. Furthermore, it is beneficial to prevent biases that may be introduced by the method.

6.3.1 Evaluation of non-linearity correction

Figure 6.12 shows the neutron capture peaks on hydrogen and gadolinium nuclei with and without the linearized-PE calibration. After fitting the peaks with Gaussian, the ratio of peak values are calculated for the peaks with and without the linearized-PE calibration. Neutron capture peaks on hydrogen and gadolinium nuclei are 2.224 and 8.029 MeV, so the ratio should be 3.61. Ratio of energy peaks is calculated as: 3.52 without calibration, and 3.60 with calibration. So the discrepancies to the truth value is decreased to 0.28% from 2.4% by the linearized-PE calibration.

6.4 Uniformity calibration

Detector response is position dependent due to reasons such as detector geometry, difference of the PMT and electronics response, and so on. Therefore, uniformity calibration is

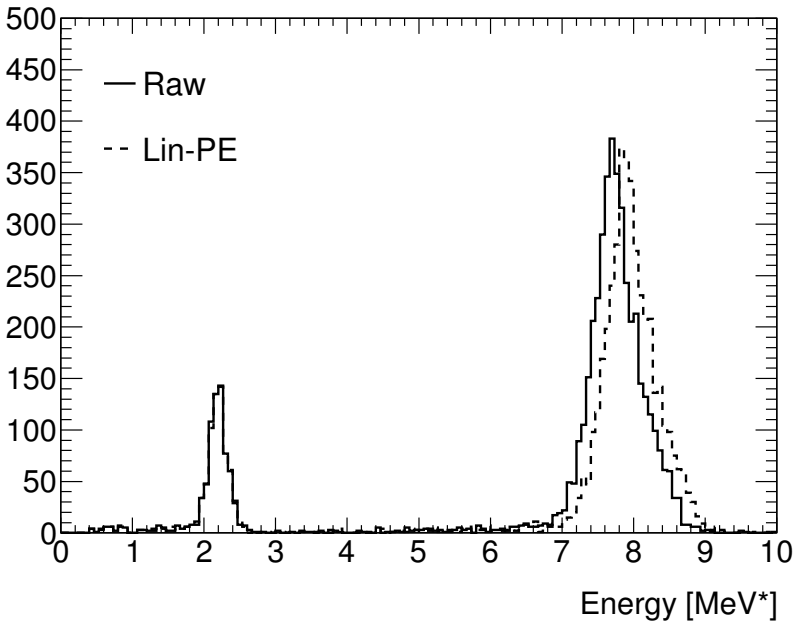

Figure 6.12: The solid line shows the neutron capture peaks without the linearized-PE calibration, while the dashed line shows that with the linearized-PE calibration. Ratio of these peak values are compared. Energy scale is defined by neutron capture on hydrogen nuclei peak to be 2.2 MeV.

introduced to reduce the position dependence of the energy, and it reduces the difference of the detector response between the data and Monte-Carlo simulation.

Uniformity calibration corrects the position dependence of the number of photoelectrons which is derived after the linearized-PE calibration. Correction maps were created both for the data and Monte-Carlo simulation independently as a function of cylindrical coordinate as parameters, which can be written as $f_u^m(\rho, z)$ $(m = data, MC)$.

Gamma rays from neutron captures on hydrogen nuclei are used to create the correction map. In the data, neutrons collected from muon spallation on carbon in the scintillation liquid are used, while in the Monte-Carlo, neutrons are collected from the IBD events. A 2.2 MeV gamma emerges after neutron capture on hydrogen nuclei. These events are collected for the ID and GC region, and number of photoelectrons are measured by blocks of ρ and z. The number of photoelectron distribution is fitted by a function including gamma-ray signals by Gaussian and background model to extract the peak position. The vertex reconstruction algorithm (see section 4.2) is utilized to obtain the vertex position of the neutron capture events.

Figures 6.13 and 6.14 show the energy correction maps for the data and Monte-Carlo simulation. The figures show the ratio of the peak of the number of photoelectron distribution at any location to that at the center of the detector. By applying the obtained correction factor to the data and Monte-Carlo, it is possible to cancel out the position dependence of energy. In these figures, both data and Monte-Carlo simulation have similar distribution, which indicates that dominant factor of the position dependence is the detector geometry.

Systematic uncertainty is evaluated from residual position-dependent difference between data and Monte-Carlo taken with neutron captures on gadolinium nuclei events. The evaluated systematic uncertainty is 0.36 %.

6.5 Absolute energy calibration

The absolute energy scale to obtain MeV from number of p.e. is measured by fitting the peak of neutrons from ^{252}Cf captured on hydrogen nuclei, which is at 2.2 MeV. Only one deployment data is used for the absolute energy calibration. The scale was measured by fitting the energy peak, and defines to make the peak energy 2.2 MeV. The energy distributions for the data and Monte-Carlo simulation are shown in Figure 6.15.

From the measurement, the factors $1/f_{\mathrm{MeV}}^m$ which convert p.e. into MeV are determined: 186.2 p.e./MeV and 186.6 p.e./MeV for the data and the Monte-Carlo simulation, respectively.

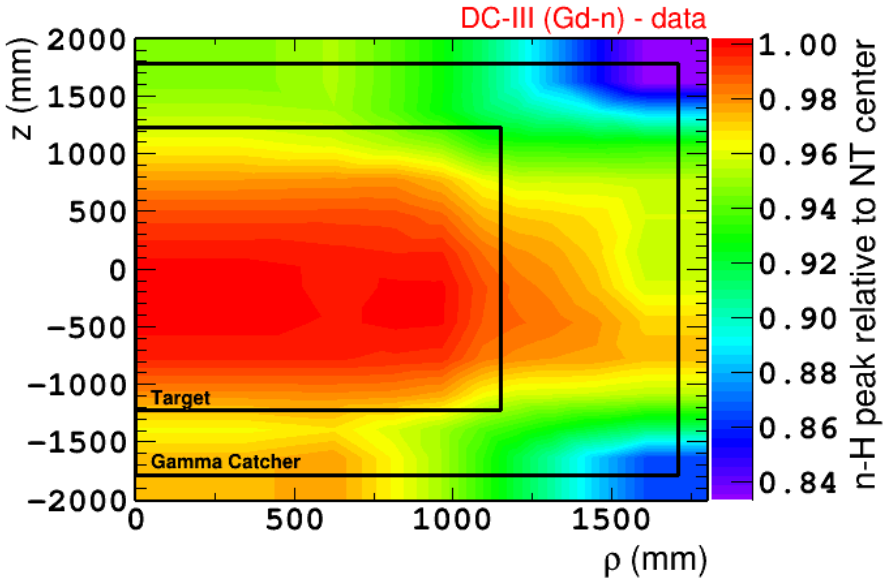

Figure 6.13: Uniformity correction map for the data [37].

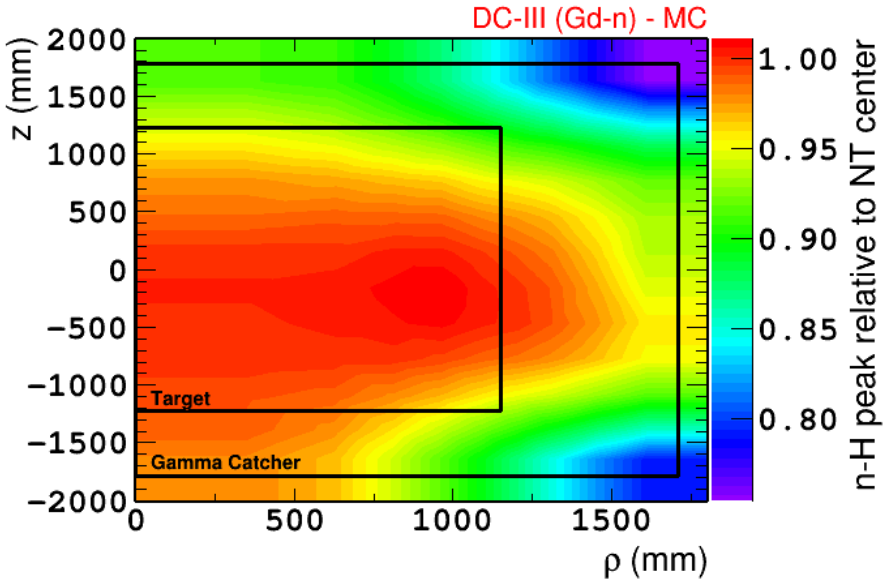

Figure 6.14: Uniformity correction map for the Monte-Carlo simulation data [37].

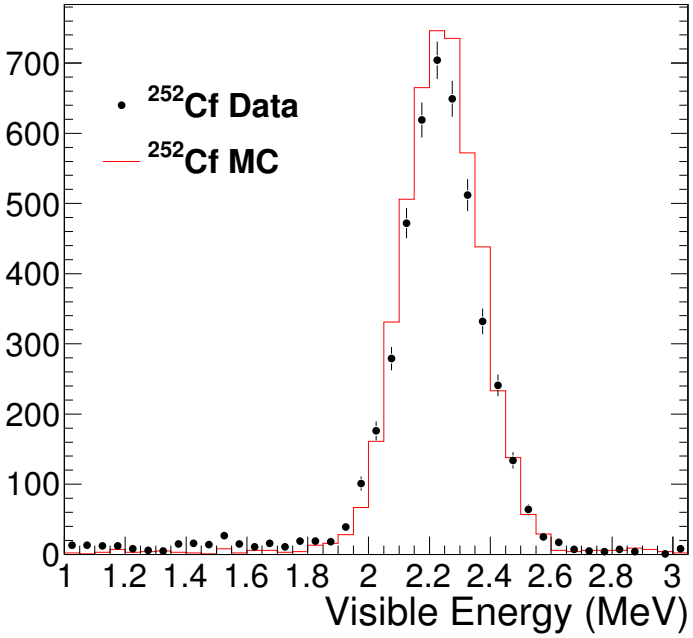

Figure 6.15: Black points show the energy distribution taken with a neutron source ^{252}Cf deployed at the center of the detector. Red histogram shows the Monte-Carlo simulation. [37]

6.6 Stability correction

Fluctuation of visible energy needs to be corrected for good energy resolution. Dominant origins are considered to be caused by instabilities of mean gain (here it refers to the factor of integrated charge to p.e.) and detector response. The instabilities of the detector response include, for instance, light yield of the scintillator liquid, the response instability of the PMTs and readout electronics. The Monte-Carlo simulation of the Double Chooz detector does not assume time instability of the detector response, so the stability correction is only applied to the data. The stability correction is aimed to reduce the time fluctuation of visible energy.

In addition, it was found that time fluctuation is energy dependent. It is considered to be caused by residual gain non-linearity and inefficiency of single p.e. detection. The energy dependence was properly taken into account by scaling the correction factor with respect to energy. The scaling of the correction function was defined by minimizing the fluctuation of three energy peaks derived from sources which have different energies. The method is explained later in this section. Since the correction function is a function of time and energy, it can be written as:

$$f_s^{\text{data}}\left(E_{\text{vis}}^0, t\right). \tag{6.8}$$

The correction factor is calculated from the Poisson corrected PMT hits multiplicity, as it is defined as $n = -N_{\text{PMT}} \ln\left(1 - N_{\text{Hits}}/N_{\text{PMT}}\right)$ in which n is calculated from neutron capture on hydrogen nuclei events. Figure 6.16 shows the distribution of n which is calculated from events taken with neutron captures on hydrogen nuclei. The correction factor is applied to visible energy obtained by the absolute energy calibration.

By its definition, the multiplicity must correspond to the total number of p.e.. The stability correction is carried out by equalizing the observed total number of p.e. to the expectation of number of p.e. from the multiplicity, and we denote the factor as α. Figure 6.17 shows the fluctuation of α.

As described before, the fluctuation of visible energy is energy dependent. Therefore, strength of the stability correction is scaled as a function of the visible energy. Energy peaks from three kinds of signals are used as an indicator of the magnitude of time variance, and used for determination of scaling of the correction factor α. Two of these signals are energy peaks of neutron captures on hydrogen and gadolinium nuclei. These energies peak at 2.2 MeV and 8.0 MeV for the neutron captures on hydrogen and gadolinium nuclei respectively. The third signal is alpha decays of ^{212}Po collected using the ^{212}Bi$-$ ^{212}Po decay chain coincidence signals. The α particle from the decay has energy of 8.8 MeV, however, due to quenching effect, the visible energy is reduced at around 1 MeV. Using the α particle from the decay chain, fluctuation of the visible energy below neutron capture peaks can be monitored.

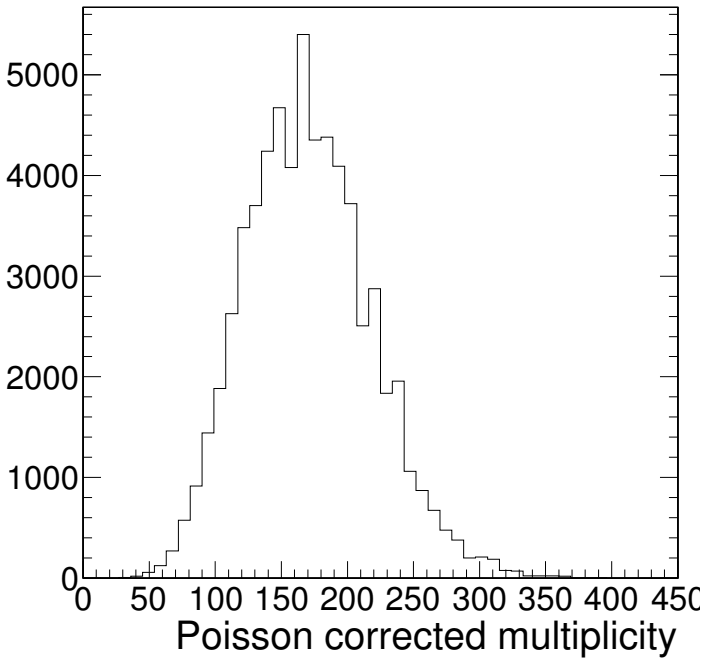

Figure 6.16: Distribution of the PMT hit multiplicity n.

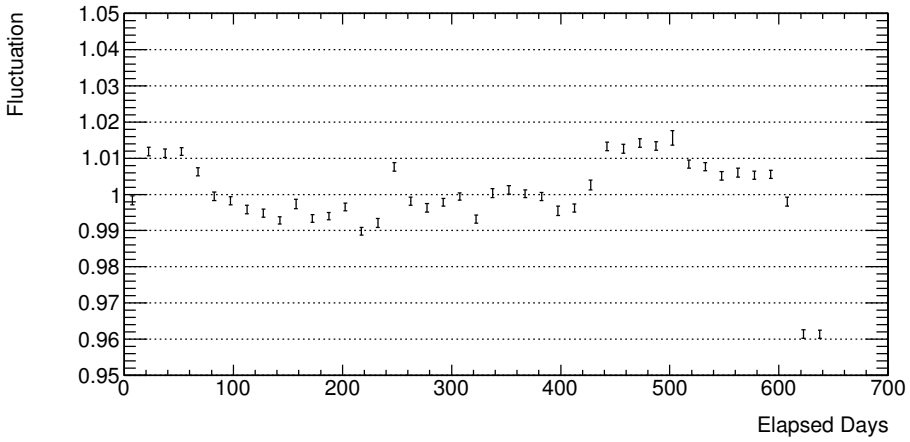

Figure 6.17: Stability of the correction factor α.

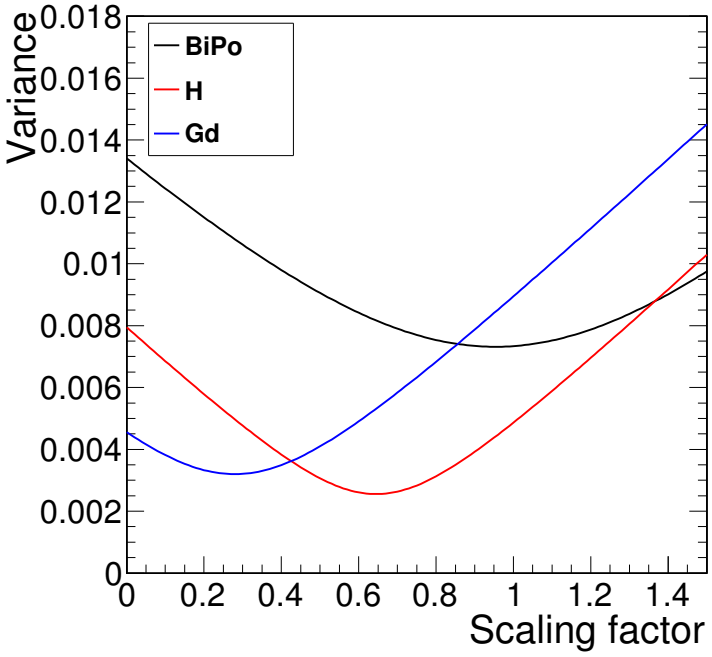

Figure 6.18: Variance of fluctuation with respect to scale of α fluctuation.

The variance of fluctuation with respect to the scale of α is shown in Figure 6.18. The fluctuation is smallest for the neutron captures on hydrogen nuclei, because the PMT hit multiplicity is derived from this signal. The variance from α decay of ^{212}Po is relatively large, it is because of less samples. Figure 6.19 shows the relationship between the best scaling and energy. From the three sources, the result indicates that the scaling decreases linearly with respect to energy.

Increment (or decrement) of the time variation for the whole data taking period is checked by linear regression. This is also taken into account by the stability correction. Figure 6.20 shows the long time behavior of the energy stability which is monitored using neutron captures on hydrogen nuclei. The measurement shows that visible energy varies 0.3 percent per year increase for the whole run period with the Double Chooz far detector.

As we saw before, the stability correction uses correction factor n to reduce the time instability of energy scale. The stability correction function takes into account energy dependence and long time stability. The energy dependence is parameterized by two parameters: a, b. Then the energy dependence can be represented as a function of energy: $aE + b$. While the long time stability is parameterized by one parameter c, as a function of time: cT. Therefore, in total, three parameters are used to determine the stability correction function. It was carried out by moving the parameters a, b and c to minimize the total variation of time fluctuations from three sources. The variation of

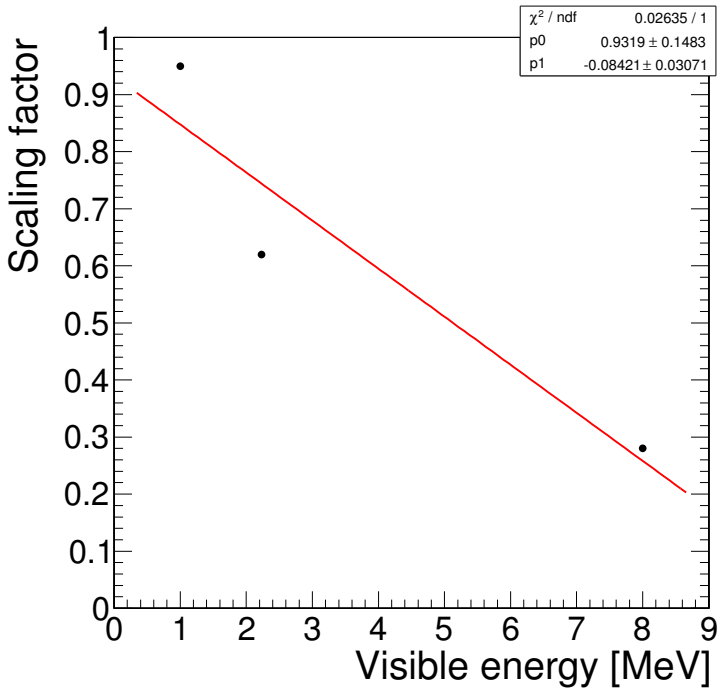

Figure 6.19: Relationship between the best scaling and energy

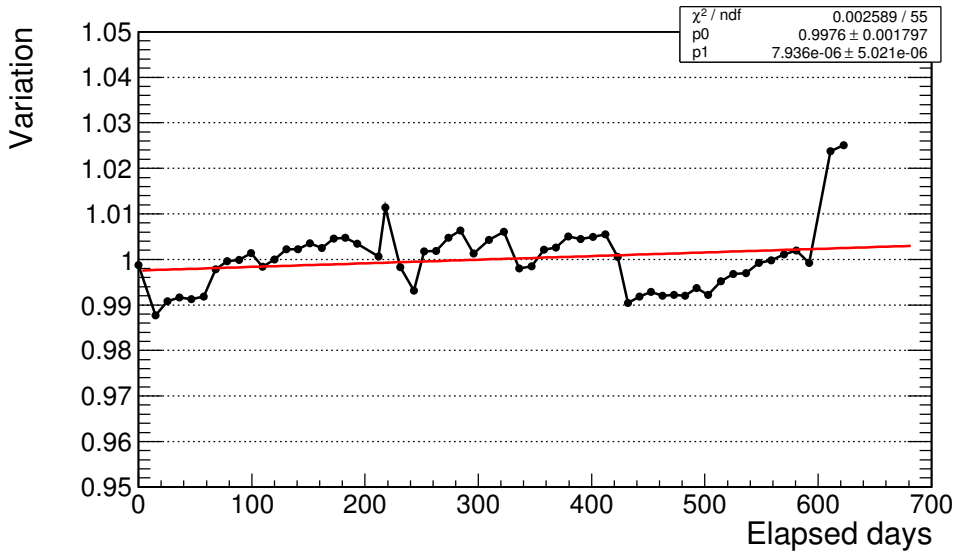

Figure 6.20: Stability of the energy peak taken from neutron captures on hydrogen nuclei events. The visible energy is found to vary 0.3 % per year.

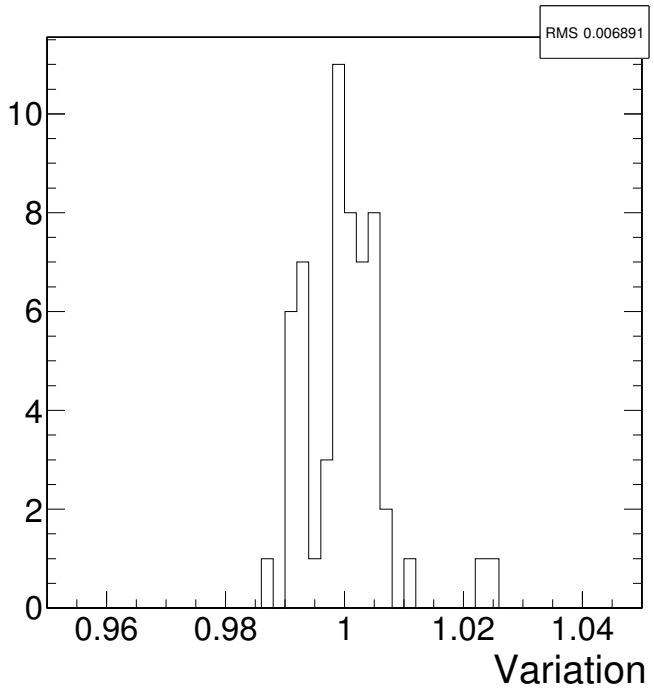

Figure 6.21: Fluctuation of the energy peak from neutron captures on hydrogen nuclei events. RMS is measured to be 1.2 %.

time fluctuation is calculated as a RMS of variance for each 15 days. In this manner, the correction function is calculated as:

$$f_s^{\text{data}}\left(E_{\text{vis}}^0, t\right) = 1.0 + \delta\alpha \times \left(0.7866 - 0.07101 \times E_{\text{vis}}^0\ [\text{MeV}]\right) - 8.24 \times 10^{-6} \times (t\ [\text{day}] - 398.0)\,. \tag{6.9}$$

$\delta\alpha$ is the fluctuation of correction factor measured for each 15 days interval.

The fluctuations of energy peaks without stability calibration are shown in Figure 6.21. Without the stability calibration, the fluctuation of the visible energy is found to be 1.2 % from the measurement of the energy peak derived by cosmic muon induced neutron capture on hydrogen nuclei events.

Figure 6.22 shows the stability of the energy peaks comparing before and after the stability correction. The magnitude of fluctuation after the stability correction was measured to be 0.70 %, 0.17 %, and 0.25 % at 1 MeV, 2.2 MeV, and 8 MeV energies, respectively. Thus, the time stability is suppressed by applying the stability calibration. It was found that the stability measurement by the neutron capture on hydrogen nuclei is the most stable among the signals. It is understandable because the neutron capture on hydrogen nuclei is used for the calculation of PMT hit multiplicity.

The systematic uncertainty of the stability is evaluated to be 0.50 %. It is estimated from the remaining timing variation after the correction using α decays of ^{212}Po and

neutron captures on Gd nuclei events weighted to the IBD energy spectrum.

6.7 Energy non-linearity correction

The energy non-linearity correction is applied to the Monte-Carlo to correct for relative energy non-linearity difference between data and Monte-Carlo.

The energy non-linearity is considered to originate from two different sources, namely charge non-linearity (QNL) and light non-linearity (LNL). The QNL originates from the modeling of the readout system and charge reconstruction algorithm. Therefore, the QNL correction is applied to all events. On the other hand, the LNL originates from scintillator modeling, and it is particle dependent. Since the energy of prompt (positron) signal is important for the neutrino energy measurement, the LNL correction for the prompt signal is studied and applied only to the prompt signals.

From the measurement, the correction function for the Monte-Carlo is determined as:

$$f_{\mathrm{nl}}^{\mathrm{MC}}\left(E_{\mathrm{vis}}^{0}\right) = \left(0.0023 \times E_{\mathrm{vis}}^{0}\ [\mathrm{MeV}] + 0.9949\right) \times \left(-0.027/E_{\mathrm{vis}}^{0}\ [\mathrm{MeV}] + 1.008\right). \quad (6.10)$$

In this equation, the first factor represents the QNL correction, whereas the second factor represents the LNL correction.

The QNL is measured by signals of neutron capture on gadolinium nuclei by deploying ^{252}Cf neutron source at the center of the detector. On average 3.76 γ's are emitted from the neutron capture with a total energy of the signal at 8 MeV, therefore the energy of γ-ray is almost the same energy as that from the neutron capture on hydrogen nuclei. Therefore, the behavior of the energy non-linearity which shows up by the ratio of energy peaks from neutron captures on gadolinium and hydrogen nuclei between the data and Monte-Carlo is understandable to be caused by modeling of the readout system and charge reconstruction algorithm.

On the other hand, LNL is a function of the energy of one γ-ray. The LNL is measured by generating Monte-Carlo simulations with different combinations of the liquid scintillator parameters. The parameters for Birks' quenching effects kB and light yield of the liquid scintillator are considered [60, 61]. The light yield affects the fraction of Čherenkov light in the total light yield, and different light yield makes the different behavior of the non-linearity. The parameters which perform the best agreement between the data and Monte-Carlo are chosen for the LNL correction.

Comparison of ratio of the visible energy between the data and Monte-Carlo with the QNL correction, with and without the LNL correction is shown in Figure 6.23. It shows the ratio of the visible energies observed with ^{68}Ge, ^{137}Cs, ^{60}Co and ^{132}Cf sources between the data and Monte-Carlo as a function of the single γ energy. The energy of the single γ of neutron capture on gadolinium nuclei is evaluated using Monte-Carlo. These sources

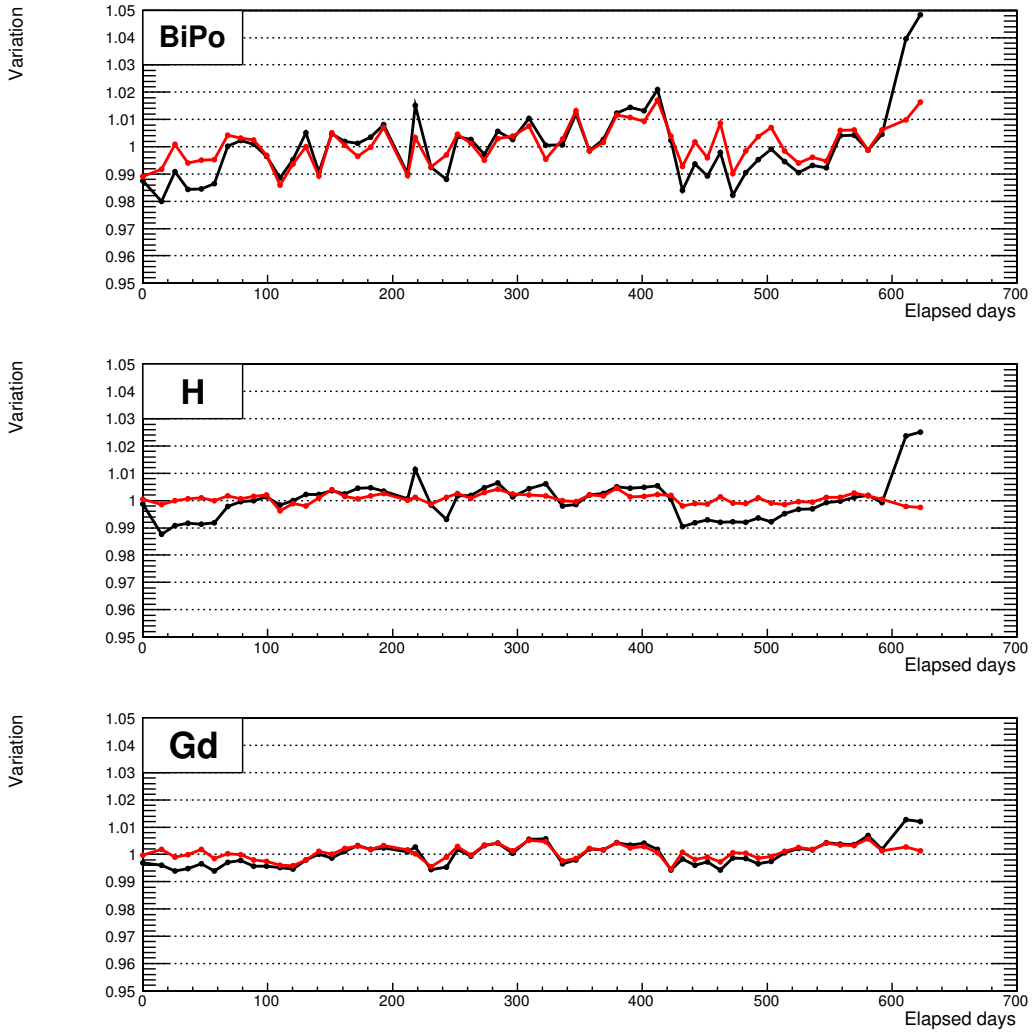

Figure 6.22: From up to down, the stability of ^{212}Po, neutron captures on H, and neutron captures on Gd peaks are shown. The stability is measured with 15 days of interval. The black line shows before the stability correction and the red line shows after the correction. It can be seen that stability is improved after the correction. Significant stability improvement is seen on neutron captures on H nuclei peak is seen, because the PMT hit multiplicity is measured from the neutron captures on H nuclei events. The fluctuation of ^{212}Po peak is relatively high because of low statistics.

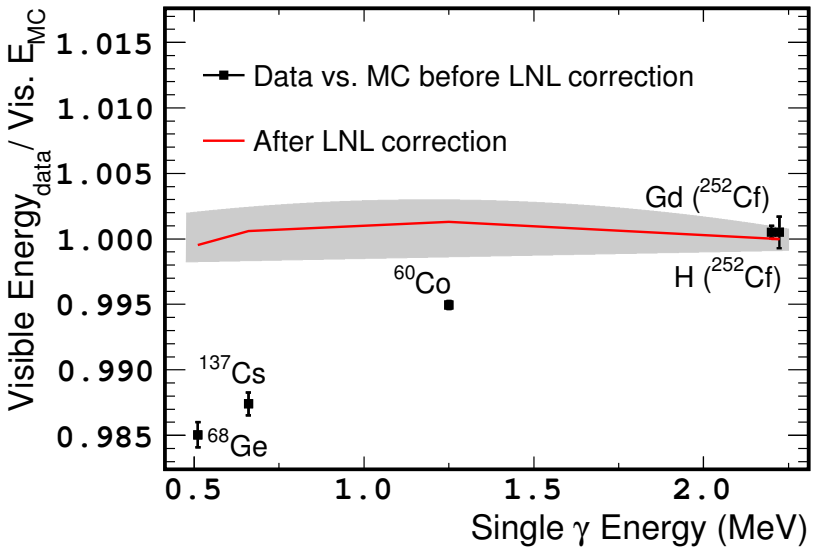

Figure 6.23: Non-linearity of visible energy between the data and Monte-Carlo after the QNL correction is applied to the Monte-Carlo [37]. The x-axis is the average energy of single γ. Black points show the discrepancy between the data and Monte-Carlo after the QNL correction is applied, but without the LNL correction. Red line shows the non-linearity of single γ energy between the data and Monte-Carlo with the LNL correction. The systematic uncertainty is shown by the gray band.

are deployed at the center of the NT. In the figure, Gd (^{252}Cf) and H (^{252}Cf) show the neutron captures on gadolinium and hydrogen nuclei respectively. As mentioned before, it is not the total energy but energy of single γ, so the energy of the Gd (^{252}Cf) and H (^{252}Cf) are almost same. The result shows that the non-linearity depends on single γ energy but not the total visible energy. It indicates that the remaining non-linearity after the QNL correction is caused by the scintillator modeling, but not by the readout modeling or charge reconstruction algorithm.

Figure 6.24 shows resolution of the visible energy. The data and Mote-Carlo are compared. Derived values are fit with the function defined below:

$$\frac{\sigma}{E_{\rm vis}} = \sqrt{\frac{a^2}{E_{\rm vis}} + b^2 + \frac{c^2}{E_{\rm vis}^2}} \tag{6.11}$$

where a, b and c are statistical fluctuation, constant term, and energy independent width due to electronic noise, respectively.

The derived values of a, b, and c are summarized in Table 6.1. From these values, the data and Monte-Carlo are consistent within errors.

Finally, systematic uncertainties on energy scale is summarized in Table 6.2.

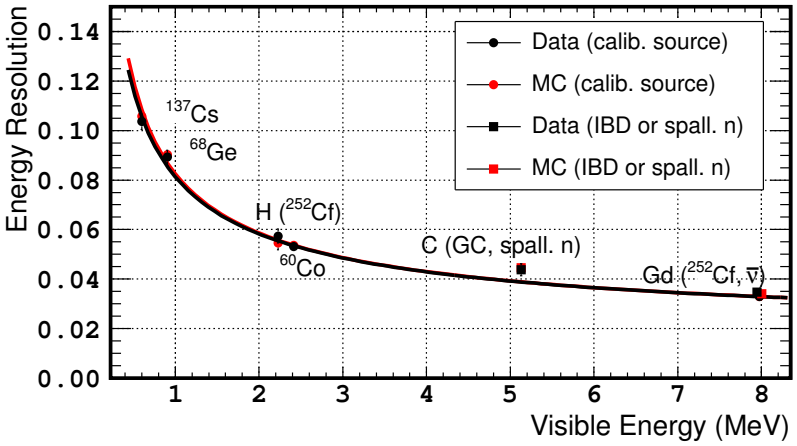

Figure 6.24: Resolution of visible energy with respect to visible energy [37]. Visible energy is obtained from fitting of energy peaks. 2.2 MeV peak by neutron capture on hydrogen nuclei is used to adjust for the absolute energy for the data. Visible energy of ^{68}Ge is less than 1 MeV, which is different from 1.022 MeV. It is due to remaining non-linearity and quenching effect, therefore the QNL/LNL correction is applied to the Monte-Carlo. Discrepancy between the data and Monte-Carlo is small by the correction.

Table 6.1: Systematic uncertainty on energy scale.

	Data	MC
a	0.077 ± 0.002 MeV$^{1/2}$	0.077 ± 0.002 MeV$^{1/2}$
b	0.018 ± 0.001	0.018 ± 0.001
c	0.017 ± 0.011 MeV	0.024 ± 0.006 MeV

Table 6.2: Systematic uncertainties on energy scale.

Source	Uncertainty (%)
Non-uniformity	0.36
Instability	0.50
Non-linearity	0.35
Total	0.74

Chapter 7

Signal prediction

7.1 Production of reactor anti-neutrino

Reactor anti-neutrino is produced by beta decays through nuclear fission reaction. Mainly, four radioisotopes ^{235}U, ^{239}Pu, ^{238}U, and ^{241}Pu contribute to produce neutrinos. These nuclei split into two or more lighter nuclei e.g. ^{140}Ba and ^{94}Kr by absorbing a neutron. These nuclei tend to have more neutrons than protons, therefore electron anti-neutrinos are produced by beta decays from those nuclei.

The reactions are described here one by one. First, fission reaction of ^{235}U is written as:

$$^{235}\mathrm{U} + n \rightarrow A + B + 6.1\beta^- + 6.1\bar{\nu_e} + 202\ \mathrm{MeV} + 2.4\ n. \tag{7.1}$$

Where the numbers show the average numbers of β^-, $\bar{\nu}_\mathrm{e}$, neutron, and the energy released to the outgoing particles. A and B are the daughter nuclei. Next, reaction of ^{238}U is written as:

$$^{238}\mathrm{U} + n \rightarrow A + B + (5 \sim 7)\beta^- + (5 \sim 7)\bar{\nu_e} + 205\ \mathrm{MeV} + xn. \tag{7.2}$$

Reaction of ^{239}Pu which is produced through the following reaction:

$$^{238}\mathrm{U} + n \rightarrow {}^{239}\mathrm{U} \rightarrow {}^{239}\mathrm{Np} \rightarrow {}^{239}\mathrm{Pu} \tag{7.3}$$

There are two chains of reactions to dominate the neutrino production from the fission. One is represented as follows:

$$^{239}\mathrm{Pu} + n \rightarrow A + B + 5.6\beta^- + 5.6\bar{\nu_e} + 210\ \mathrm{MeV} + 2.9n. \tag{7.4}$$

And the other case, firstly ^{241}Pu is produced by the neutron captures:

$$^{239}\mathrm{Pu} + 2\mathrm{n} \rightarrow {}^{240}\mathrm{Pu} + \mathrm{n} \rightarrow {}^{241}\mathrm{Pu} \tag{7.5}$$

Then ^{241}Pu produces neutrinos:

$$^{241}\mathrm{Pu} + n \rightarrow A + B + 6.4\beta^{-} + 6.4\bar{\nu_e} + 212 \text{ MeV} + 2.9n. \quad (7.6)$$

Approximately six neutrinos are produced during a chain decay of the fission product. Neutrino energy spectra for ^{235}U, ^{239}Pu, and ^{241}Pu distribute around a few MeV as measured by the ILL and Bugey experiments (described in the next section). The total thermal power of the Chooz reactor (P) is 3 $\mathrm{GW_{th}}$ (3×10^9 J/s), and the release energy per fission (E) is about 200 MeV, therefore neutrino rate can be roughly calculated like:

$$n = \frac{P}{E} \times 6 = \frac{3 \times 10^9 [\mathrm{J/s}]}{1.6 \times 10^{-19} [\mathrm{J/MeV}] \times 200 [\mathrm{MeV/fission}]} \times 6 [\bar{\nu}_\mathrm{e}/\mathrm{fission}] \sim 6 \times 10^{20} [\bar{\nu}_\mathrm{e}/\mathrm{s}] \quad (7.7)$$

Thus, large number of few MeV energy electron anti-neutrinos are produced in the reactor cores. Reactors are good source for neutrino experiment to measure θ_{13} in the viewpoint of its flux and energy as well as the cost (it is free neutrino source for physics experiments).

7.2 Reactor simulation

Double Chooz measures electron anti-neutrinos produced in two reactor cores of Chooz nuclear power plant. Therefore, it is essential to precisely predict the neutrino flux for the precise measurements of the θ_{13}.

The neutrino flux is predicted by simulation. Information provided by French electric utility company Électricité de France S.A. (EDF) which operates the Chooz nuclear power plant is used as inputs for the simulation. The informations are thermal power, locations and initial burn-up of each nuclear fuel assembly. The thermal power is given as instantaneously for each reactor core with a time step of less than 1 minute with uncertainty of 0.5 % of the full reactor power (4.25 $\mathrm{GW_{th}}$). Figure 7.1 shows the time variation of the thermal powers for the Chooz reactors B1 and B2. The locations and initial burn-up of each nuclear fuel assembly are provided for every reactor fuel cycle which is approximately one year in duration.

In the reactor core, $\bar{\nu}_\mathrm{e}$'s are produced by β-decay of fission products. More than 99.7 % of neutrinos originate from four isotopes: ^{235}U, ^{239}Pu, ^{238}U, and ^{241}Pu. Reference $\bar{\nu}_\mathrm{e}$ spectra from three of these isotopes ^{235}U, ^{239}Pu, and ^{238}U are derived from measurement of their β spectrum at the ILL research reactor [62, 63, 64]. In addition, anti-neutrino spectrum for the ^{238}U is measured by the experiment described in Ref. [65]. However, energy regions which is used for the neutrino oscillation measurement is not fully covered by this measurement. Therefore, combination of the summation method [66] and an exponential-polynomial fit on the data is developed to predict the anti-neutrino energy spectrum from the ^{238}U to cover the energy region below 3 MeV and above 7.5 MeV. The energy spectra of electron anti-neutrino from these nuclei are shown in figure 7.2, in

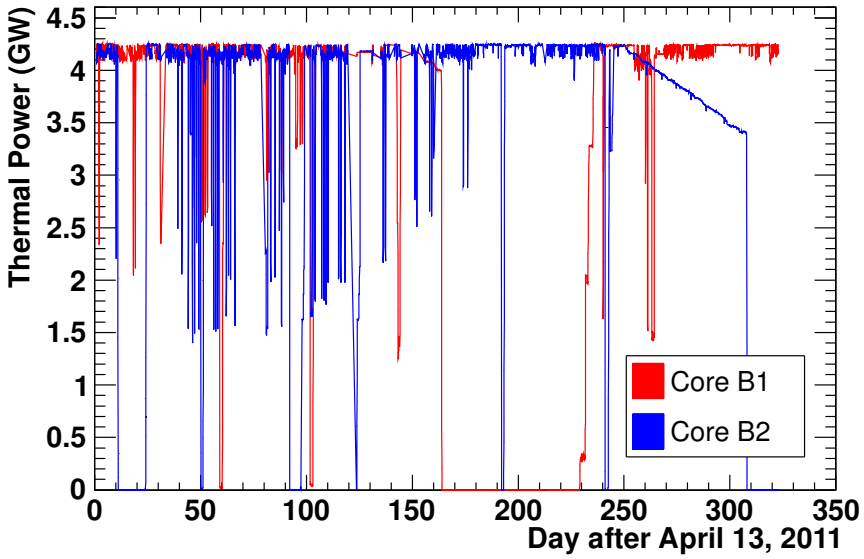

Figure 7.1: Time variation of the thermal powers of the Chooz reactors B1 and B2 since starting day of the data taking of Double Chooz. Thermal powers of the Chooz B1 reactor is shown with the red line while the B2 reactor is shown with the blue line.

which ^{238}U spectrum is from simulation which is consistent with the one based on the measurement used in the analysis described in this paper.

As time elapses, the component of the nuclear fuel assembly changes. Mixture ratio of ^{235}U decreases while mixture ratios of ^{239}Pu and ^{241}Pu increase. Since the energy spectra of neutrinos are different for each source, it is important to estimate the time variation of the composition of the nuclear fuel assembly. Double Chooz uses two codes to simulate the reactor cores and estimate fission rates of fuel isotopes in the reactors. They are MURE and DRAGON [68, 69, 70, 71]. MURE simulates a full 3D core by Monte-Carlo techniques to model the neutron transport, while DRAGON simulates individual fuel assemblies with 2D modeling. It simulates the neutron transport by some approximation. MURE is used as the primary simulation code, while the DRAGON is used as quick assembly-level cross checks. Time variation of fission rates which is computed using MURE code for the main four isotopes is shown in Figure 7.3 (for Chooz B1 reactor). Information of the thermal power and the boron concentration are used for the computation provided by EDF.

These codes are validated with Takahama-3 reactor data. Both codes are consistent with other codes which are commonly used in the reactor industry for reactor modeling [72]. Also, Double Chooz uses neutrino rate measurement data by Bugey4 [73] at a distance of 15 m to mitigate uncertainties on the neutrino spectra as described in Section 7.5.

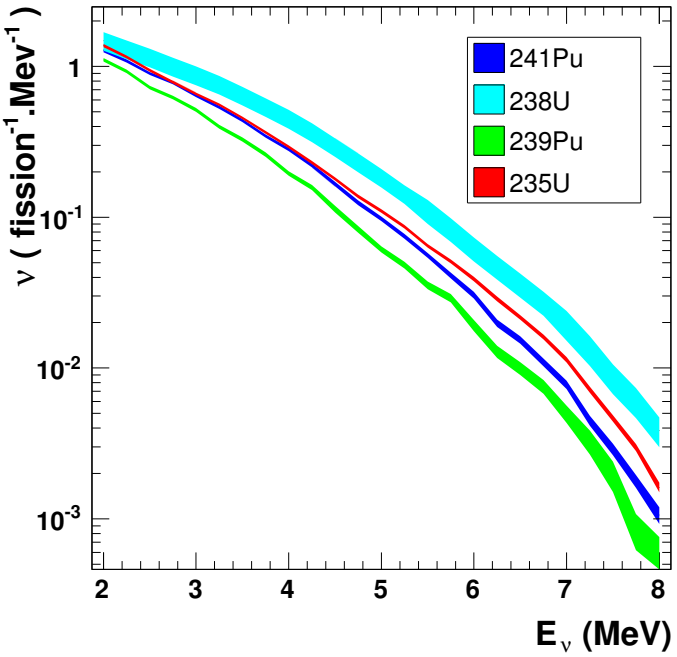

Figure 7.2: Electron anti-neutrino spectra from the four isotopes ^{235}U, ^{239}Pu, ^{241}Pu, and ^{238}U. The spectra from ^{235}U, ^{239}Pu, and ^{241}Pu are estimated in Ref. [67]. The spectrum ^{238}U is estimated in Ref. [65].

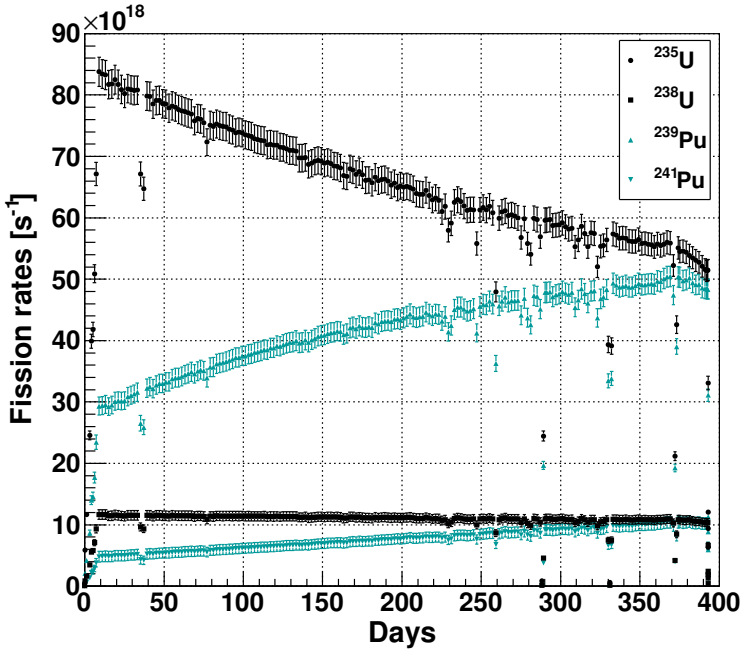

Figure 7.3: Time variation of fission rates for the main four isotopes ^{235}U, ^{239}Pu, ^{238}U, and ^{241}Pu at the Chooz B1 reactor. The rates are computed by using the MURE code. Discrete drops of the fission rates are due to reactor off.

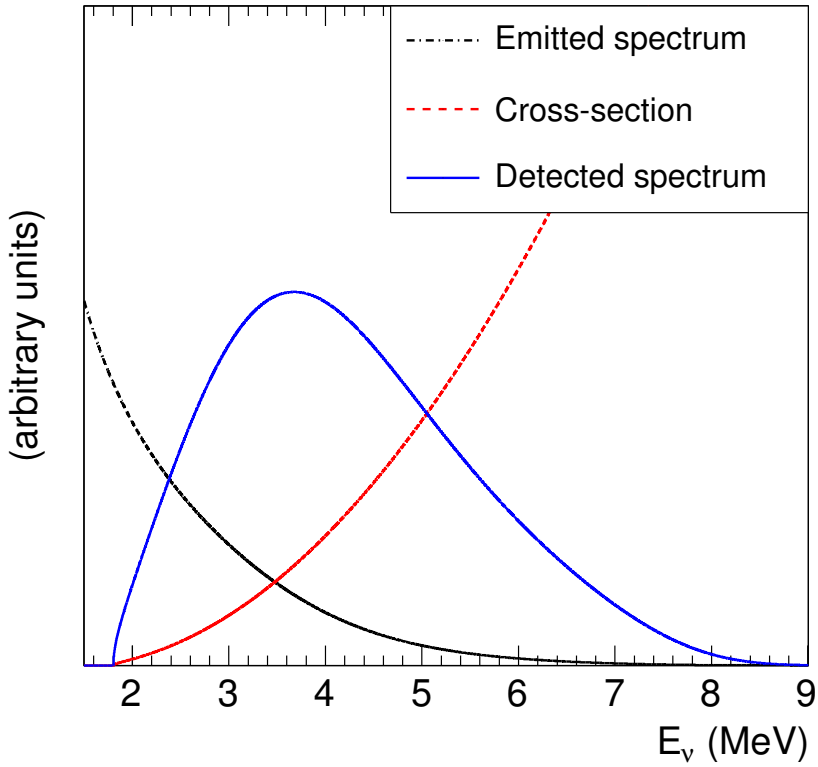

Figure 7.4: IBD cross section (red), reactor neutrino flux (black), and convolution of the reactor neutrino flux and IBD cross section (blue) [77].

7.3 IBD cross section

The cross section of inverse beta decay (IBD): $\bar{\nu_e} + p \rightarrow e^+ + n$ can be approximately calculated [74]:

$$\sigma_{\text{IBD}}\left(E_\nu\right) = \kappa p_e E_e, \tag{7.8}$$

where $E_e = E_\nu - (M_n - M_p)$ represents the energy of the positron, and $p_e = \sqrt{E_e^2 - m_e^2}$ represents the momentum of the positron. κ is a factor:

$$\kappa = \frac{2\pi^2/m_e^5}{f^R \tau_n} = 0.961 \times 10^{-43} \left[\frac{\text{cm}}{\text{MeV}}\right]^2, \tag{7.9}$$

where $f^R = 1.7152$ is the phase space factor for the beta decay of the free neutron, and $\tau_n = 881.5 \pm 1.5$ [s] is the neutron lifetime [75]. It is approximated to order of $1/M$, where the M is average nucleon mass [76]. Figure 7.4 shows the cross section of IBD reaction, reactor neutrino flux, and convolution of the reactor neutrino flux and cross section of IBD reaction with respect to the neutrino energy.

7.4 Detector simulation

Double Chooz developed detector simulation tool based on Geant4.9.2.p02 [78, 79]. Customized models of the neutron scattering, gadolinium γ cascade, scintillation processes, and photo-cathode optical surface are implemented. In the neutron scattering model, hydrogen molecular bonds in elastic scattering below 4 eV based on [80] is implemented as well as radiative capture model below 300 eV is improved. The customized model was tested and found to have better performance compared to the default Geant4.9.2.p02.

In the simulator code, the detector geometry, detector liquids, readout system are implemented. The parts of the detector geometry and detector liquids are based on Geant4, while the readout is modeled by a custom simulation code. The acrylic and steel vessels, support structure, PMTs and its shielding are included as the detector geometry. The light yield of the NT and GC liquid scintillators, photo-emission time probabilities, light attenuation, and ionization quenching treatments based on the lab measurements are included as optical parameters of the detector liquids implemented in the simulator. In the readout simulation, response of the PMTs, front-end electronics, flash-ADC, and data acquisition system are implemented. The readout system is empirically simulated by probability distribution functions based on the measurements. It characterizes the responses of each readout component to single photo-electron. Responses to multi photo-electrons are simulated by accumulating the single photo-electron waveform signal. Channel-wise response variations caused by gain, baseline, and noise are also taken into account based on the measurements.

7.5 Prediction of neutrino flux and systematic uncertainty

The expected number of IBD interactions is given by:

$$\frac{dN^R(t)}{dt} = \frac{\epsilon N_p}{4\pi} \frac{P_{th}^R(t)}{L_R^2 \langle E_f \rangle^R(t)} \langle \sigma_f \rangle^R(t), \tag{7.10}$$

where, ϵ is the neutrino detection efficiency. N_p is the number of target protons in the NT. $P_{\rm th}^R(t)$ is the thermal power of the reactor R (e.g. Chooz B1 and B2 reactors). L_R is the distance between the reactor R and the detector. $\langle E_f \rangle^R(t)$ is the mean energy release per fission. $\langle \sigma_f \rangle_R$ is the mean cross section per fission. $\langle E_f \rangle$ and $\langle \sigma_f \rangle_R$ are calculated as a sum of each fuel isotope k:

$$\langle E_f \rangle_R(t) = \sum_k \alpha_k^R \langle E_f \rangle_k(t) \tag{7.11}$$

$$\langle \sigma_f \rangle_R(t) = \sum_k \alpha_k^R \langle \sigma_f \rangle_k(t) \tag{7.12}$$

Table 7.1: Uncertainties on the reactor neutrino flux prediction.

Source	Uncertainty (%)
σ_{Bugey4}	1.4
Fractional fission rate of each isotope	0.8
Thermal power	0.5
IBD cross section	0.2
Mean energy released per fission	0.2
Distance to reactor core	< 0.2
Total	1.7

As it will be described in section 11.1, the neutrino oscillation analysis is performed by separating energy into 40 bins. For this reason, systematic uncertainty on the neutrino prediction is represented by a 40×40 covariance matrix, in which each matrix element corresponds to each energy bin. The flux covariance matrix is given as a sum of each factor of uncertainties:

$$M_{ij}^{\text{flux}} = M_{ij}^{N_p} + M_{ij}^{L} + M_{ij}^{P_{\text{th}}} + M_{ij}^{\sigma_{\text{Bugey4}}} + M_{ij}^{\langle E_f \rangle} + M_{ij}^{\alpha_k} + M_{ij}^{\langle \sigma_f \rangle}. \tag{7.13}$$

The matrices on the right-hand side are the covariance matrices for each property indicated with the superscript.

The systematic uncertainties on the reactor neutrino flux is summarized in table 7.1. The total uncertainty is measured to be 1.7 % to the IBD signal rate. The dominant systematic uncertainty on the neutrino prediction is due to the experimental error of the Bugey4 measurement, which is 1.4 %.

Chapter 8

Neutrino selection

In Double Chooz, reactor electron antineutrinos are observed at a rate of about 50 events per day. On the other hand, trigger rate is about 150 Hz (corresponds to 13 million events per day). The events are mostly γ's from natural radioisotopes contained in the detector materials. Thus, selection method is developed for the effective neutrino event selection against the background.

The details are explained in this chapter.

8.1 Single event selection

Primarily, events which satisfy the following conditions are kept.

- Not a muon. An event which satisfies $Q_{\mathrm{IV}} > 30000$ DUQ [1] or $E_{\mathrm{ID}} > 20$ MeV is defined as a muon event, where Q_{IV} is the total measured charge in the IV region, and E_{ID} is the visible energy in the ID region.
- Δt with respect to last muon is larger than 1 ms.
- Visible energy is larger than 0.4 MeV.
- Not a light noise.

Muons deposit large energy when they pass into the detector, so it can be identified as an event with large energy in the ID as well as the IV region. Not only the muon, but also events following the muons are rejected, because large amount of background induced by spallation neutrons and cosmogenic isotopes are included. In addition, muon's large energy makes baseline to fluctuate, and precision of energy reconstruction is worsen for a certain period after the muon signals. Muon rate is measured to be 45 Hz, and inefficiency

[1] DUQ is a unit of integrated charge. The integrated charge is computed by the algorithm explained in section 4.1.

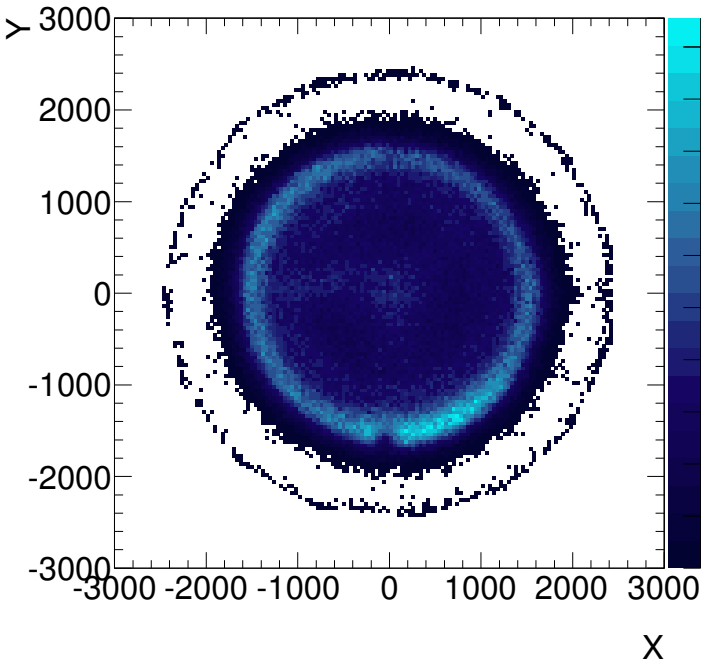

Figure 8.1: Vertex distribution of the single events plotted on XY-plane within -500mm $<$ z $<$ 500mm. Large fraction of events are distributed close to the wall of the detector, because majority of the single events are considered as gammas from detector materials such as the wall stainless steel and PMTs.

to the 1 ms of the muon veto is calculated to be 4.5%. Low energy events below 0.4 MeV are rejected, since it is much below the minimum energy of $\bar{\nu}_{\mathrm{e}}$ at 1.02 MeV. It was checked that inefficiency due to this threshold is small enough and negligible. Furthermore, events so-called "light noise" is eliminated by a technique which is described later in this section. The light noise is a spontaneous light emission from some PMT bases.

The remaining events are called single events. Figures 8.1 and 8.2 show the vertex distribution and energy spectrum of the single events respectively.

8.1.1 Light noise cut

Events satisfy all conditions below are kept.

- $Q_{\mathrm{max}}/Q_{\mathrm{tot}} < 0.12$
- $Q_{\mathrm{diff}} < 30000$ DUQ
- $\sigma_T < 36$ or $\sigma_{\mathrm{Q}} < 464 - 8 \cdot \sigma_{\mathrm{T}}$

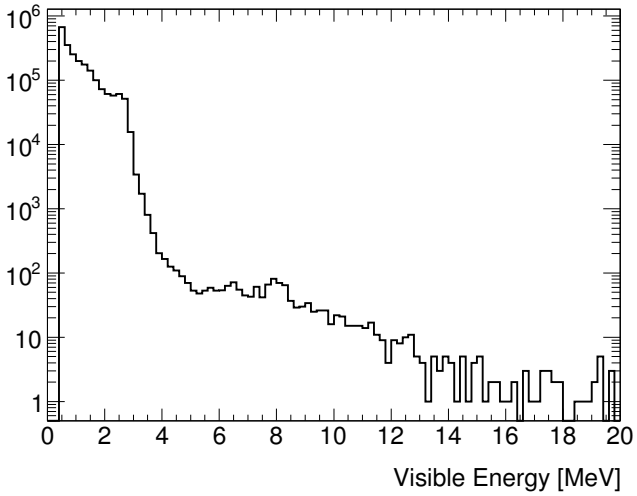

Figure 8.2: Energy spectrum of the single events. There are many events below 4 MeV due to γ rays from radioactivities. An energy peak due to neutron captures on gadolinium nuclei events is seen around 8 MeV.

Candidates of inverse beta decay signals are selected from the remaining events after the selection listed above. Each of the item is explained one by one here.

First is about the $Q_{\rm max}/Q_{\rm tot}$ cut, where $Q_{\rm max}$ is the maximum measured charge of all ID readout channels, and the $Q_{\rm tot}$ is the total charge. Since the light noise is caused by light emission at the base of the PMTs, the light noise events tend to have large value of the $Q_{\rm max}/Q_{\rm tot}$. By requiring the condition $Q_{\rm max}/Q_{\rm tot} < 0.12$, light noise events can be reduced.

$Q_{\rm diff}$ is also a measure of "locality" of charge distribution. It is defined as the sum of difference of charge between the max charge PMT and surrounding PMTs close to the max charge PMT. $Q_{\rm diff}$ is defined by the formula below:

$$Q_{\rm diff} = \frac{1}{N}\sum_i \frac{(Q_{\rm max} - Q_i)^2}{Q_i}, \tag{8.1}$$

where N is number of PMTs within a distance of 1 m from the PMT which gives the maximum charge and i indicates the PMTs around, $Q_{\rm max}$ is the maximum charge and Q_i is individual charge measured by the i-th PMT, respectively. Light noise event tends to have larger value of the $Q_{\rm diff}$.

Moreover, two dimensional cut is applied for the light noise rejection. $\sigma_{\rm T}$ is the standard deviation of the start time distribution for the first pulse from each readout channel. The start time is defined in section 4.1. $\sigma_{\rm Q}$ is the standard deviation of the integrated charge distribution of all readout channels in the ID. Figure 8.3 shows the distribution of physics events and light noise events in the $\sigma_{\rm T}$ - $\sigma_{\rm Q}$ plane. Smaller $\sigma_{\rm T}$ area

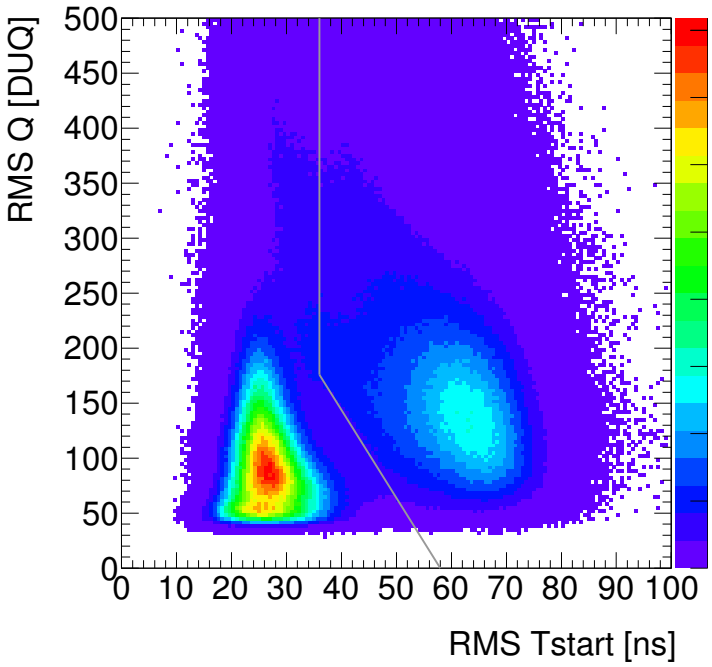

Figure 8.3: Two dimensional cut for light noise rejection. The sample is single events after the $Q_{\mathrm{max}}/Q_{\mathrm{tot}}$ cut and Q_{diff} cut are applied. The gray line indicates the criteria. The events in the right region are light noise events.

is physics event rich, while large number of light noise events are found in large σ_T area. The figure indicates that σ_{T} can be loosen in the region where the σ_{Q} is low. Thus, it improves the efficiency of physics events by using the correlation between the σ_T and σ_Q for the cut, at the same time reducing light noise events.

Figure 8.4 shows the energy spectrum of all triggers without muon events, nor events after 1 ms after the muon events. After the light noise rejection, peaks such as neutron capture on gadolinium nuclei (8 MeV), 2.6 MeV γ from ^{208}Tl are emerged. Inefficiency for IBD signals due to the light noise rejection is estimated to be $0.0124 \pm 0.0008\%$ by Monte-Carlo simulation.

8.2 Time and space coincidence cut

Prompt signals are selected as events which satisfy the visible energy is between 0.5 MeV and 20 MeV. And the energy for the delayed events is between 4 MeV and 10 MeV.

Following time and space coincidence selection are applied to a pair of prompt and delayed signals:

- Time correlation between the prompt and delayed signals should satisfy $0.5 < \Delta T <$

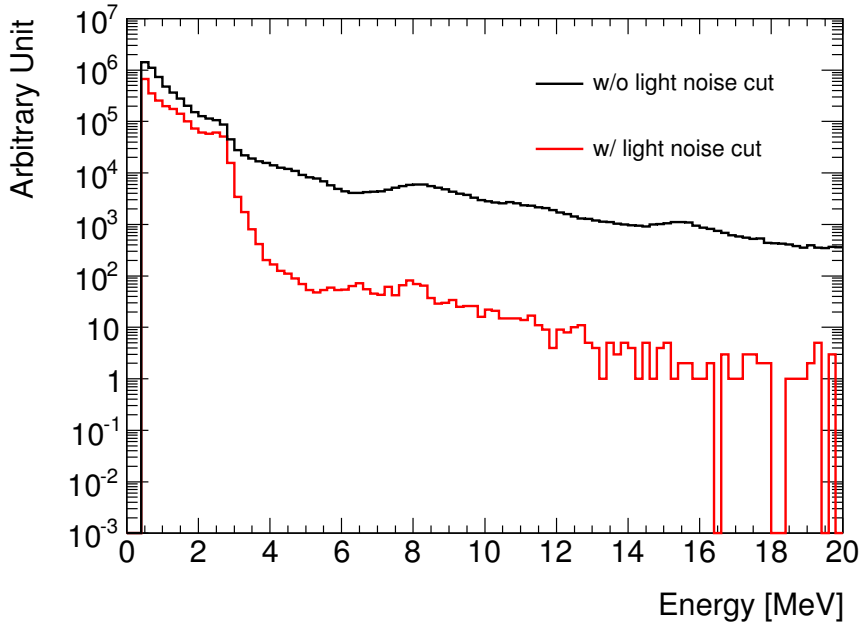

Figure 8.4: Energy spectrum before (black histogram) and after (red histogram) the light noise cut. The red histogram is same as the histogram in Figure 8.2.

150 μs.

- Distance between the reconstructed vertex positions of prompt and delayed signals should satisfy $\Delta R < 100$ cm.

8.2.1 Multiplicity cut

Cosmic ray muons create multiple neutrons, and these neutrons are suppressed by multiplicity cut. The multiplicity cut rejects events if there are extra signals in a certain period. The definition is as follows:

- No valid triggers (single events) allowed in 200 μs preceding the prompt signal.
- Only one signal (it is delayed signal) is allowed in 600 μs following the prompt signal.

8.3 Background reduction cuts

Although large amount of the background events can be removed by the time and space coincidence cut, remaining background events can be further removed by the background reduction cuts. In the analysis, F_V veto, OV veto, IV veto, and Li + He veto are introduced. These cuts are explained one by one.

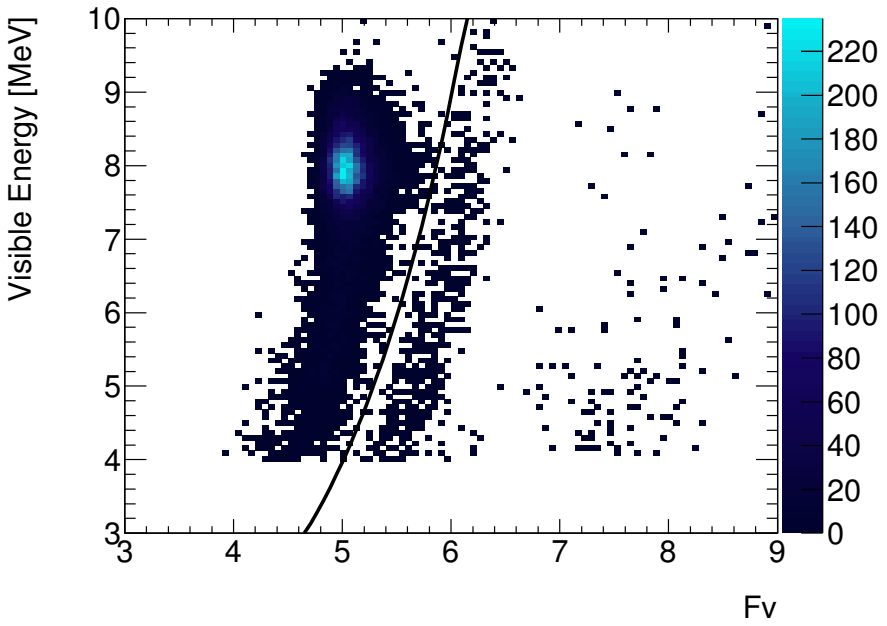

Figure 8.5: F_V versus visible energy for IBD candidates (without F_V cut). Drawn line is the cut criteria. The events on the left of the line are determined as neutrino events, and the events on the right are determined as backgrounds.

8.3.1 F_V veto

F_V veto can effectively reduce stopping muon backgrounds. The definition of F_V is given by equation 4.5. F_V indicates consistency of the PMT hit pattern with the expectation assuming a point light source at the reconstructed vertex position. The value of F_V becomes large when an event is not point-like. The stopping muon events which happen inside the chimney tend to have large F_V. Figure 8.5 shows the correlation between F_V and visible energy of delayed signals. Three components can be found in the figure: lower F_V band, middle F_V band, and higher F_V band. Most of signals are contained in the lower F_V band, which are IBD signals. Signals in the middle F_V band is considered as stopping muons. Finally, higher F_V band indicates the remaining light noise events. Thus, F_V veto effectively rejects these background signals.

From the result, F_V veto condition is defined as:

$$E_{\mathrm{vis}} > 0.068 \exp\left(\frac{F_V}{1.23}\right). \tag{8.2}$$

The F_V veto is applied to the delayed signals.

8.3.2 OV veto

If the prompt signal is coincident with OV hits within 224 ns, the event is rejected. The OV veto cut is introduced to reduce the stopping muons. Muon deposit energy in the OV before it enters the ID, so OV hit event is recognized as muon.

8.3.3 IV veto

IV veto is intended to reduce fast neutron backgrounds. Fast neutron often makes recoil protons which deposit energy in the IV. The deposited energy is less than the energy of threshold energy to identify muons (30000 DUQ). IV veto recognizes fast neutrons by signals of IV as well as correlation between the signals in the IV and signals in the ID. The IV veto condition is defined as:

- IV PMT hit multiplicity ≥ 2.
- Total integrated charge int the IV $\geq$ 400 DUQ [2].
- Distance of reconstructed event vertex in the ID and the IV is less than 3.7 m.
- Difference between the ID hit timing and IV hit timings is less than 50 ns.

8.3.4 Li+He veto

Li+He veto cut is applied for cosmic background rejection. Likelihood of ^{9}Li is calculated from signals of the prompt and delayed events, and events which satisfy the following condition are kept:

$$\mathcal{L}_{^9\mathrm{Li}} < 0.4 \tag{8.3}$$

The details about the lithium and helium background, and /shows is described in section 10.4.2.

8.4 Summary

17351 neutrino candidates are obtained by the selection. Figure 8.6 shows the ΔT distribution between the prompt and delayed IBD candidates. We confirmed that the ΔT distribution follows the exponential function with $\tau = 27\mu$sec from inverse beta decay reaction followed by neutron capture on gadolinium nuclei. The value is close to the expectation value of 31.1 μs. Energy spectrum of the delayed signal is shown in Figure 8.7. The 8 MeV peak of neutron capture on gadolinium nuclei peak can be seen.

Figure 8.8 shows the distribution of vertex distances between the prompt and delayed IBD candidates.

[2] 400 DUQ roughly corresponds to 0.2 MeV.

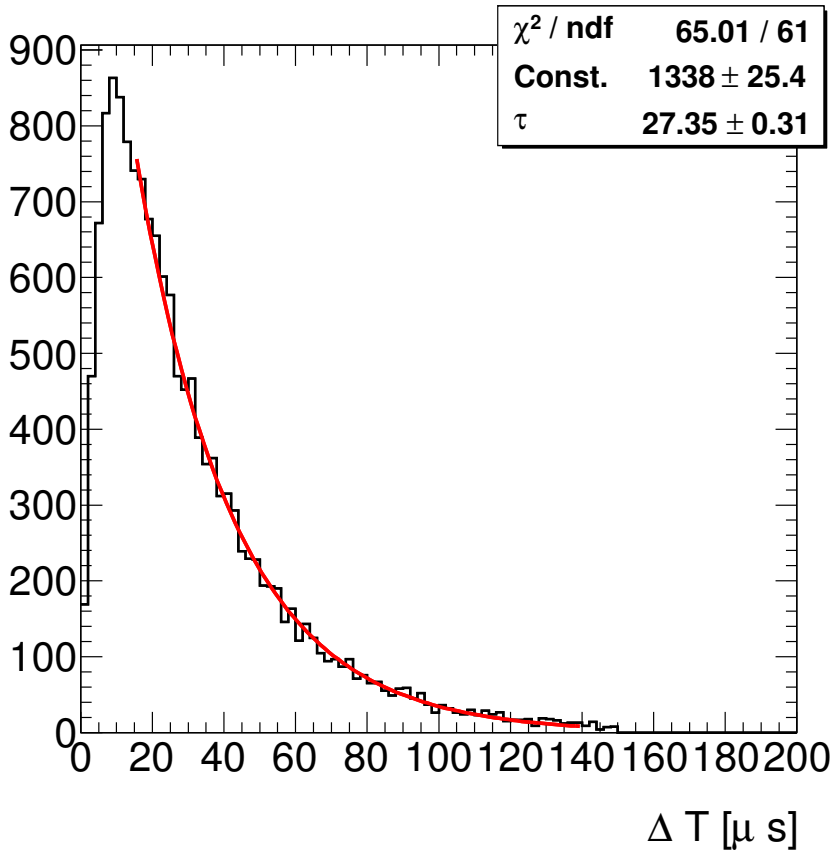

Figure 8.6: Distribution of ΔT between the prompt event and delayed event. From the fitting with the exponential curve, $\tau = 27\mu$sec was measured. It is consistent with the prediction.

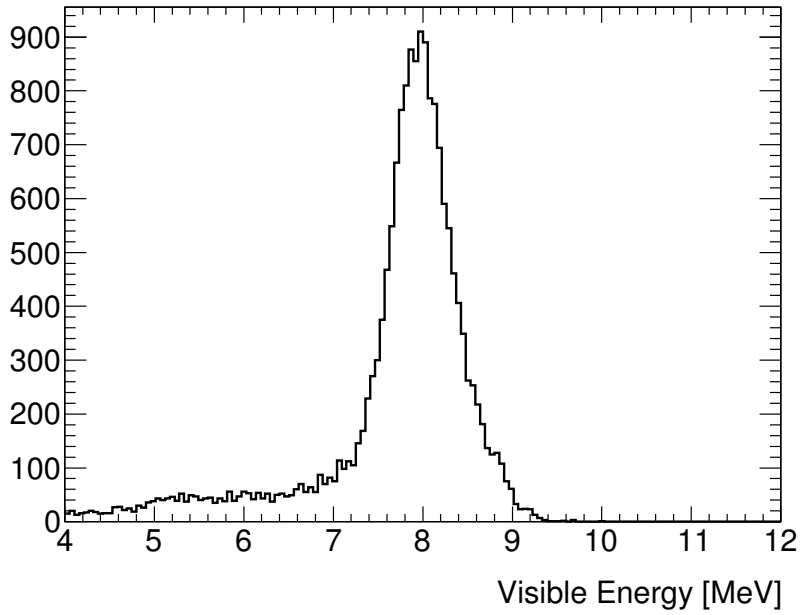

Figure 8.7: Energy spectrum of the delayed events. A peak of neutron captures on gadolinium nuclei at 8 MeV is seen.

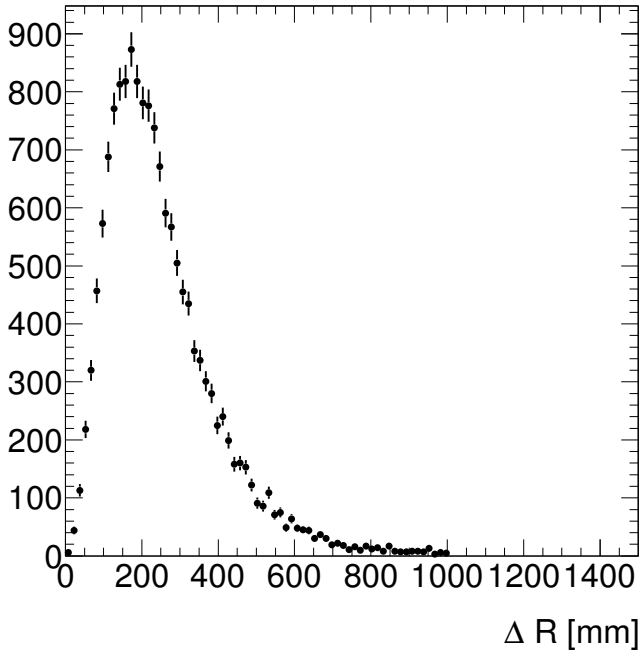

Figure 8.8: Distribution of ΔR between the prompt event and delayed event.

Chapter 9

IBD detection efficiency

In this chapter, the measurement of IBD detection efficiency for the data and Monte-Carlo is described. Difference of the IBD detection efficiency between the data and Monte-Carlo is measured, and the correction factor is introduced to cancel out the difference.

IBD detection efficiency is evaluated from three aspects: 1) Gd fraction, 2) IBD selection efficiency, and 3) spill-in/out. Correspondingly, IBD detection efficiency is corrected by measurement for each contribution and corrected with correction factors: C_{GdF} for Gd fraction, C_{Eff} for IBD selection efficiency, and C_{Sio} for spill-in/out.

The Gd fraction is a fraction of number of IBD candidates captured on gadolinium nuclei to that captured on gadolinium and hydrogen nuclei. Gd concentration in the NT determines the ratio of neutrons to be captured on Gd nuclei to H nuclei, therefore the detection efficiency is affected by the Gd fraction. The IBD selection efficiency concerns the events which are rejected with the standard IBD selection cut. The spill-in/out is a pair of processes which is related with a neutron transfer between the NT and GC regions. The spill-in occurs when IBD reaction happens in the GC, and emitted neutron moves into the NT and captured on Gd nuclei. On the contrary, spill-out occurs when IBD reaction happens in the NT, and emitted neutron moves into the GC and captured on H nuclei so that it is not identified as the IBD signal. The systematic uncertainty on the spill-in and spill-out currents are estimated in comparison of two different simulation codes.

All of the listed aspects are related with delayed signals. Inefficiency of the prompt signals is negligible due to dead time free data acquisition system, and the trigger efficiency of 100 % when visible energy is larger than 500 keV.

9.1 Gd fraction

The fraction of Gd in the NT was measured using ^{252}Cf neutron source deployment data. The ^{252}Cf source emits neutrons with γ rays. On average, the number of emitted neutrons

is 3.8 per spontaneous fission [81]. Signals from the γ rays are detected as a prompt event, and neutron capture signals are detected as delayed events. The fraction of Gd is estimated by measuring the fraction of number of neutron capture events with different energy windows. The energy window for the numerator is decided to be $3.5 < E_{\rm vis} < 10$ MeV, which only contains neutron capture on Gd nuclei events. The energy window for the denominator is decided to be $0.5 < E_{\rm vis} < 10$ MeV, which contains neutron capture on Gd nuclei as well as H nuclei events. Other selection criteria are the same as the standard IBD selection cut, however, following cuts are additionally applied for rejecting accidental backgrounds.

- $E_{\rm vis}$ of the prompt event is larger than 4 MeV.
- More than one neutrons are detected after the prompt signal.

Remaining accidental background is estimated from off-time coincidence window, and subtracted from the sample. The measured Gd fraction is $85.30 \pm 0.08\%$ for the data, and $87.49 \pm 0.04\%$ for the Monte-Carlo. The selection criteria for the Monte-Carlo is the same as that applied to the data. The correction factor $C_{\rm GdF}$ is obtained by dividing the Gd fraction for data by that of the Monte-Carlo:

$$C_{\rm GdF} = 0.9750 \pm 0.0011(stat) \pm 0.0041(syst). \tag{9.1}$$

Evaluation of the systematic uncertainty is carried out by changing the energy windows.

The value is measured with different positions and time of the data taking. The result shows that Gd fraction is uniform in the NT and stable during the data taking period.

9.2 IBD selection efficiency

IBD selection efficiency is estimated for the data and Monte-Carlo. The estimation is carried out by two methods. One of the method uses ^{252}Cf neutron source, and another one uses IBD candidates. From the measured selection efficiency, correction factor of the selection efficiency (data to Monte-Carlo) is calculated to be $C_{\rm Eff} = 1.0000 \pm 0.0019$ from a combination of the two methods. The estimated correction factor are consistent with unity within uncertainty of a few per mil by both methods. Details are described by the following subsections.

9.2.1 Efficiency measurement by Cf neutron source

Using the ^{252}Cf source, high statistics of neutron capture events with negligible background contamination can be obtained. From the data, efficiency of the neutron capture signal is measured. The data are taken with z-axis fish line. The ^{252}Cf source was deployed at different levels along the vertical axis. The efficiency is measured from number

of selected events by two selections. One is the standard IBD selection, while the other is a loosen selection. The signal window for the loosen selection is extended as shown by the following conditions:

- 0.25 μs $< \Delta T <$ 1000 μs
- No ΔR cut
- 3.5 MeV $< E_{\rm vis} <$ 10 MeV

The efficiency is calculated from the ratio of the number of neutron capture events taken with these selections. Namely, calculating the ratio of the number of neutron capture events with the standard selection as the numerator, and that with the loosen selection as the denominator. The energy window for the looser cut is defined to be the same as that used in numerator for Gd fraction measurement not to double count the inefficiency.

Since the efficiency in the NT is position dependent, the average efficiency over the full NT is estimated using the calibration data taken with the ^{252}Cf source, which is taken at different positions. The correction factor is given as a function of z and ρ as:

$$\epsilon(z, \rho) = \epsilon_0 \times f_1(z) \times f_2(\rho), \tag{9.2}$$

where ϵ_0 is the correction factor measured using data taken with ^{252}Cf neutron source deployed at the center of the detector, and $f_1(z)$ and $f_2(\rho)$ represent the position dependence along the z axis and ρ axis. Figure 9.1 shows the neutron detection efficiency measured using ^{252}Cf calibration data, from which the $f_1(z)$ is calculated. On the other hand, behavior of the $f_2(\rho)$ is assumed to be same as that of the $f_1(z)$ as a function of the distance between the position and the wall of the NT. The validity of the assumption was confirmed by the Monte-Carlo simulation, and the systematic uncertainty is taken into account.

The averaged efficiency over the full NT is obtained from the integration of efficiency using the equation 9.2. The averaged efficiency is measured to be $98.29 \pm 0.23\%$ for the data, and $98.26 \pm 0.22\%$ for the Monte-Carlo simulation. Therefore, the correction factor for the IBD selection efficiency is measured to be:

$$C_{\rm Eff,Cf} = 1.0003 \pm 0.0032. \tag{9.3}$$

9.2.2 Efficiency measurement by IBD candidates

The IBD selection efficiency is also measured using the IBD candidates themselves. The benefit to use the IBD candidate is that the vertex positions distribute over the whole NT. On the other hand, the statistics of the IBD candidates is less than the samples

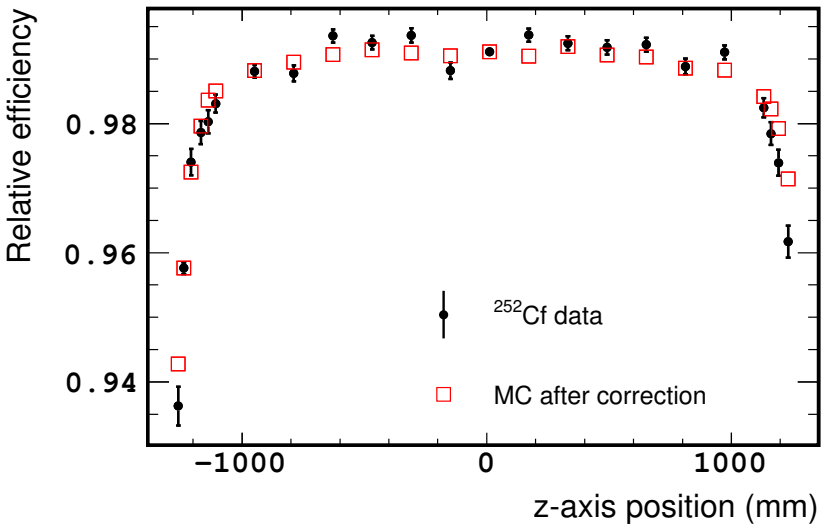

Figure 9.1: Neutron detection efficiency with respect to the z-axis [37]. The black points are the neutron detection efficiency measured by using the ^{252}Cf source, and the red squares are calculated by Monte-Carlo simulation.

taken with the calibration source, and the IBD candidates sample contains non-negligible amount of backgrounds.

In a similar manner to the efficiency measurement by the ^{252}Cf source, the efficiency is measured by a ratio of number of IBD candidates taken with the standard IBD selection to that with loosen selection. Some of the windows are extended for the loosen selection. Difference of the selection criteria for the loosen cut is listed below:

- $0.25\ \mu\text{s} < \Delta T\ \mu\text{s}$
- $\Delta R < 1.7$ m
- Visible energy of the delayed signal is: $3.5 < E_{\text{vis}} < 10$ MeV

Also, to reduce the background contamination, the following selections are applied in addition to the standard IBD selection.

- Visible energy of the prompt event is: $0.5 < E_{\text{vis}} < 8$ MeV
- F_{V} of the prompt event is less than 5.8.

The remaining accidental background is estimated by the off-time coincidence window and subtracted from the IBD candidates.

From the analysis, the efficiencies for the data and Monte-Carlo of electron antineutrino are measured to be 98.58±0.19% and 98.62±0.02%, respectively. From a comparison of the measured efficiencies for the data and Monte-Carlo, the correction factor is:

$$C_{\mathrm{Eff,IBD}} = 0.9996 \pm 0.0021. \tag{9.4}$$

Thus, a consistent value of the IBD selection efficiency with the ^{252}Cf source events is derived from the IBD candidate events. Final correction factor for the neutrino oscillation analysis is determined by a combination of the values obtained by the two methods described in this section.

9.3 Spill-in/out

The number of spill-in events (neutron emitted by IBD reaction outside the NT is captured on Gd nuclei in the NT) and spill-out events (neutron emitted by IBD reaction inside the NT is captured on H nuclei outside the NT) cannot be measured by the data. Therefore, Geant4-based Monte-Carlo simulation tool specially developed for Double Chooz is used for the estimation of the spill-in and spill-out events. Also, another Monte-Carlo simulation code, TRIPOLI-4 [82] is used for the cross check and uncertainty estimation. The neutron transport model in the Geant-4 based code does not take into account the effects of molecular bonds on neutron elastic scattering. On the other hand, the TRIPOLI-4 takes different approach to calculate the spill-in and spill-out events which is able to take into account the effects of molecular bonds between carbon and hydrogen atoms based on experimental data. Using these codes, net spill current to the number of IBD interactions in the NT is calculated. The net spill current to the number of IBD interactions is defined by the following equation:

$$\Phi_{\mathrm{Spill}} = \frac{1}{N_{\nu}^{\mathrm{Target}}} \times \left(\frac{N_{\mathrm{SI}}^{\mathrm{det}} + N_{\mathrm{SO}}^{\mathrm{det}}}{\epsilon_{\mathrm{det}}} - N_{\mathrm{SO}} \right), \tag{9.5}$$

where, $N_{\nu}^{\mathrm{Target}}$ is the number of IBD interactions in the NT. $N_{\mathrm{SI}}^{\mathrm{det}}$ is number of the spill-in events, namely, number of the IBD interactions occurred outside the detector but detected as IBD candidates. N_{SO} is number of events that IBD interactions occurred in the NT, however neutron is transfered to the GC. $N_{\mathrm{SO}}^{\mathrm{det}}$ is number of IBD interactions occurred in the NT, and produced neutrons are transfered to GC, however, it is detected as IBD interactions because the neutron is captured on ^{12}C. ϵ_{det} is the detection efficiency with IBD selection. Using the Geant4 based simulation code and TRIPOLI-4, the net spill current is measured to be 2.08 % and 2.36 %, respectively. Difference of the measurement from the Geant4 based code and TRIPOLI-4 is taken as the systematic uncertainty, and a value of 0.27 % is obtained.

$$C_{\mathrm{Sio}} = 1.0000 \pm 0.0027. \tag{9.6}$$

The correction factors are summarized in Table 9.1.

Table 9.1: Summary of the correction factor and the fraction uncertainties.

Correction source	MC Correction	Uncertainty (%)
DAQ & Trigger	1.000	< 0.1
Veto for 1 ms after muon	0.955	< 0.1
IBD selection	0.989	0.2
FV, OV, IV, Li+He veto	0.993	0.1
Scintillator proton number	1.000	0.3
Gd fraction	0.975	0.4
Spill-in/out	1.000	0.3
Total	0.915	0.6

Chapter 10

Background estimation

Three types of backgrounds are considered in the neutrino oscillation analysis: accidental coincidences, cosmogenic isotopes (^{9}Li and ^{8}He), and correlated events (fast neutrons and stopping muons).

The rates and energy spectra of the backgrounds are estimated using observed data.

10.1 Accidentals

A pair of uncorrelated events may mimic IBD signal if they coincidentally observed within the IBD selection time window. If a pair of events satisfy the IBD selection criteria, it is referred to as accidental background. Mostly, gammas from natural radioisotopes mimic the prompt (positron) signal. Natural radioisotopes (e.g. ^{238}U and ^{232}Th chains, and ^{40}K) which is contained in detector materials like PMT glass, liquid scintillator, acrylic vessels, or surrounding rock emit gamma rays. Whereas delayed (neutron capture) signal is generally mimicked by some of sources originating from cosmic muon, like spallation neutron captured on gadolinium, recoil protons from fast neutrons, or beta decay of cosmogenic isotopes (^{12}B).

A technique called off-time window method is developed to measure the rate and shape of the accidental background. The idea is simple, which utilizes the fact that the prompt and delayed signals are uncorrelated in time.

The method is to put time windows more than 1 second after the prompt candidate, and measure the random coincidence without changing other neutrino selection criteria. In order to accumulate statistics, 2000 of successive time windows are opened after 1 second for each prompt signal, so that it helps to improve the precision of the measured rate and spectrum shape.

From the measurement using the off-time window method, the accidental background rate was measured to be:

$$R_{\mathrm{acc}} = 0.071 \pm 0.0003\ (stat) \pm 0.0026\ (syst)\ [\mathrm{events/day}]. \tag{10.1}$$

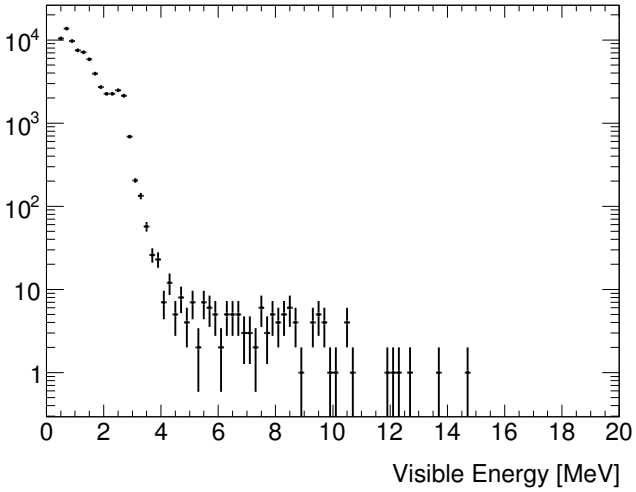

Figure 10.1: Energy spectrum of the prompt accidental background signals collected using the off-time method.

Since the off-time method uses different dead time from the standard IBD selection, the correction is applied to account for the associated systematic uncertainties. Energy spectrum of the prompt accidental background signals is shown in Figure 10.1. The spectrum distributes up to 3 MeV with 2.6 MeV gamma from thallium-208.

Figure 10.2 shows the rate stability of the accidental background. The rate is almost flat for the whole data taking period.

10.2 Fast neutrons and stopping muons

In the neutrino oscillation analysis, two kinds of correlated backgrounds are accounted for; these originate from fast neutron and stopping muon.

Fast neutron is induced by spallation interactions of cosmic muon in the rock near the detector. When fast neutron enters into the detector and collides with hydrogen nuclei, recoil proton is produced. Signals of ionization due to the recoil proton in the scintillator is recognized as a prompt signal. Through the process, the neutron loses its kinetic energy and captured on a nucleus such as gadolinium. And signal of the neutron capture is recognized as a delayed signal.

Stopping muon is a cosmic muon entering the ID and stops inside the ID. These muons are identified by the IV, but they sometimes pass into the detector through chimney. The muon decays via the Michel decay with average life time on via the Michel decay with average life time on 2.2 μs, and electron is produced. The two consecutive signals mimic the IBD reaction (muon as prompt signal and Michel electron as a delayed signal) and

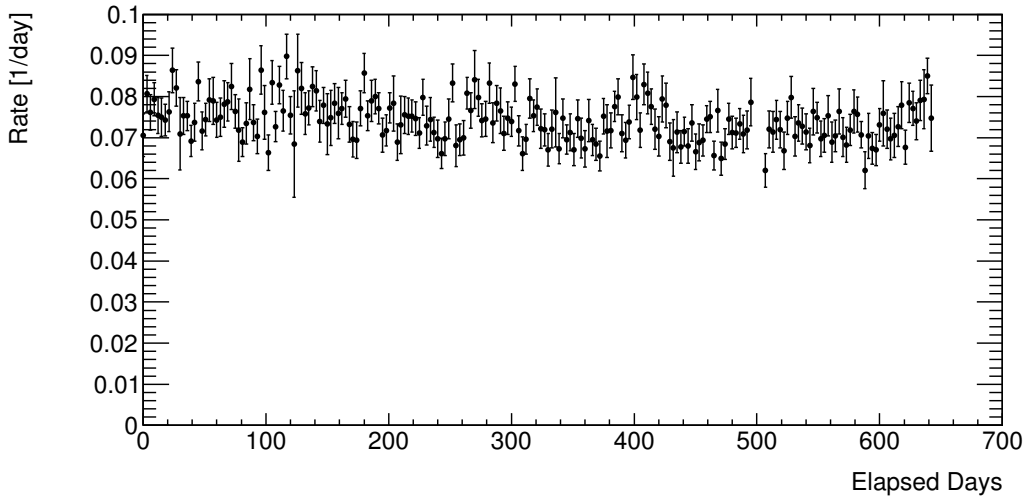

Figure 10.2: Time stability of accidentals rate.

regarded as background.

The spectrum shape is measured using events with activity in the IV, called IV-tagged events. The IV-tagged event indicates that the event penetrated the IV region. Since the fast neutron and stopping muon events often deposit energy in the IV region, these events can be selected effectively. The criteria of the IV-tagged event are defined below:

- IV PMT hit multiplicity ≥ 2.
- Total integrated charge in the IV > 400 CU (corresponding to roughly 0.2 MeV).
- Outputs of the event reconstruction in the ID and IV are close in space ($\Delta d < 3.7$m) and time (within 50 ns).
- Time coincidence between the ID and IV are close ($-110 < \Delta t < -10$nsec).

Except that the events are IV-tagged, other IBD selection criteria must be fulfilled. Figure 10.3 shows the energy spectrum of the IV-tagged events.

Count rate of the correlated background is measured by assuming the background rates due to the stopping muon and fast neutron are flat in energy. As it is shown in Figure 10.3, validity of the assumption can be confirmed by looking at the spectrum shape. Count rate of the correlated background is estimated from the number of IBD candidates between 20 MeV and 30 MeV, where IBD events and other backgrounds do not exist. In this selection, ID muon veto threshold is changed from 20 MeV to 30 MeV. Other selection criteria are same as the standard IBD selection. Impact of changing the muon veto threshold is studied, and it is confirmed to be negligible. The estimated value is 0.604 ± 0.051 events/day.

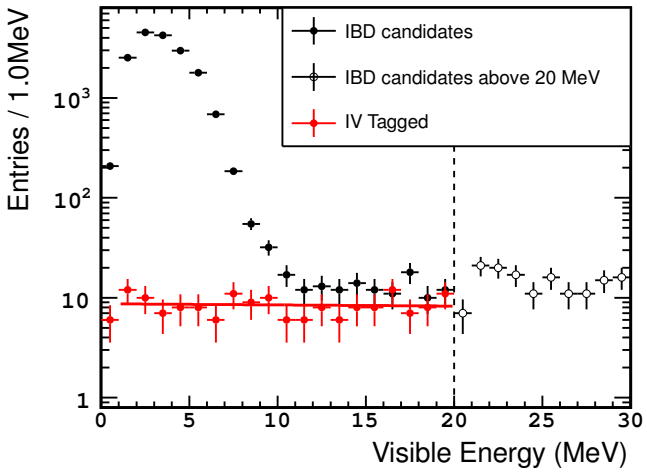

Figure 10.3: Energy spectrum of IV tagged events are shown with red points [37]. Also, energy spectrum of IBD candidates is shown with black points ($E_{\rm vis} < 20$ MeV), and circles ($E_{\rm vis} > 20$ MeV). Red line is the best fit with a linear function to the IV tagged events. During the fitting, less than 1 MeV events are not used, since events from Compton scattering of γ's are included in the IV and ID. The slope is measured to be -0.02 ± 0.11events/MeV^2 (therefore, the spectrum can be assumed as flat).

10.3 ^{12}B background

^{12}B is the most commonly generated isotope from spallation interactions by cosmic muons in the Double Chooz detector, although the ^{12}B background can be eliminated well and therefore it is not dominant in the Double Chooz experiment. However, the ^{12}B events are used for background subtraction of ^{9}Li and ^{8}He events, therefore the characteristics of ^{12}B is also explained here. The details of the ^{9}Li and ^{8}He backgrounds are described in section 10.4 later.

^{12}B is produced in the detector when a muon induced spallation neutron replaces a photon in ^{12}C nucleus. ^{12}B decays to ^{12}C by β decay with 98 % of branching ratio, and Q-value of 13.3 MeV.

$$^{12}\mathrm{B} \rightarrow \beta^{-} +^{12}\mathrm{C} \tag{10.2}$$

Emitted electron peaks at approximately 7 MeV. The lifetime is 29.1 ms, consequently the event is not vetoed by muon veto (which rejects events for 1 ms after the muon).

Therefore, ^{12}B can be prompt and delayed signal, and a pair of the ^{12}B signal and a coincident signal can be background. This kind of backgrounds are included as accidental background.

However, ^{12}B can also be correlated backgrounds. Two cases below are considered:

Case 1 Two or more ^{12}B are created from a muon, and if two of them decay within an IBD coincidence time window, the signal mimics the IBD signal.

Case 2 Combination of spallation neutron capture and ^{12}B decay within an IBD candidate time window mimics the IBD signal.

The rate of the ^{12}B background is estimated by time-off method, with different time intervals between the prompt and delayed windows. The result shows the rate is less than 0.03 events per day, which is negligible compared to the other background sources.

10.4 Cosmogenic background

Cosmogenic isotopes are produced from spallation interactions of cosmic muons inside the detector. Some of the cosmogenic isotopes such as ^{9}Li and ^{8}He emit neutron via β-n decay. The lifetime of the ^{9}Li and ^{8}He are 257.2 ms and 172 ms respectively, which are much longer than 1 ms of muon veto time. Therefore, muon veto technique does not work for the ^{9}Li and ^{8}He backgrounds. In Double Chooz, ^{9}Li is the dominant cosmogenic background.

The β-n decay for the ^{9}Li is written as below:

$$^{9}\mathrm{Li} \rightarrow 2^{4}\mathrm{He} + \mathrm{e}^{-} + \mathrm{n} \tag{10.3}$$

The Q-value for this decay is 11.941 MeV, and the branching ratio is 50.8 %. The β-n decay of ^{9}Li emits an electron and a neutron. After the β-n decay, ^{9}Li becomes ^{8}Be, and immediately after that, ^{8}Be decays to two ^{4}He (α particle). The emitted electron and α particles can be recognized as a prompt signal of the IBD reaction. Then, the neutron is captured in the same way as IBD reaction, so it is recognized as a delayed signal.

The β-n decay for the ^{8}He is written as below:

$$^{8}\mathrm{He} \rightarrow^{7} \mathrm{Li} + \mathrm{e}^{-} + \mathrm{n} \tag{10.4}$$

The Q-value for this decay is 8.618 MeV, and the branching ratio is 16 %. An electron and a neutron are produced when ^{8}He decays to ^{7}Li with β-n decay. Like the case for ^{9}Li, the decay product of the electron mimics the prompt signal, and neutron capture on gadolinium nuclei mimics the delayed signal of the IBD interaction.

10.4.1 Rate measurement

Lateral distribution profiles (LDP) method

The cosmogenic background rate is measured by fitting the curve of IBD candidate rate (not exactly the IBD candidate from the standard neutrino selection. The selection criteria will be described later in this section.) as a function of the time interval between the IBD candidate and previous muon (ΔT_{μ}). The name of the lateral distribution profiles (LDP) method comes from that the method uses the information of the distance. Muons within 20 seconds in ΔT_{μ} are tested to search for the pairs of muons and IBD candidates.

The candidate sample is divided into 7 sub-samples according to the observed energy of the parent muon, because the purity of samples is different for different observed energies. Purer sample can be obtained from the muons with higher energy deposit likely due to spallation interaction inside the detector. The major contamination in the samples is due to accidental coincidence of muon-IBD pairs. Additional distance cut is applied for less than 600 MeV* [1] muon energy sub-samples for improving the purity of ^{9}Li events, which is: $d < d_{\mathrm{max}}$, where d is the distance between the muon track and vertex of the prompt signal. d_{max} is changed between 0.5 m and 1.0 m for estimating systematic uncertainty. Table 10.1 shows how the samples are divided with muon energies in which the production rate of cosmogenic βn-emitters is evaluated for each muon energy. Figure 10.4 shows the distance of the muon track and vertex of the prompt signal (LDP). In the figure, the best fit of the lateral profile is shown. The fit function is determined using toy Monte-Carlo, which is a convolution of exponential function and Gaussian function. The length is characterized by a "decay length", $\lambda_{^{9}\mathrm{Li}}$, which represents the mean distance between the vertex position of the prompt signal and the muon track. The Gaussian is

[1] MeV* is a MeV equivalent energy scale. The energy scale is not accurate at such high energy due to flash-ADC saturation effects.

Table 10.1: Result of the ΔT_μ fitting. $N_{^9\mathrm{Li}}$ is the number of ^{9}Li events extracted by the fit from the samples after the distance cut (in this table, $d < 60$ cm) is applied. f_{LDP} is fraction of ^{9}Li events within $d < 0.6$ m calculated from the LDP. N_{Li} is the total number of ^{9}Li events which is calculated by $N_{^9\mathrm{Li}}/f_{\mathrm{LDP}}$.

E_μ [MeV]	N_{Li} (d < 0.6 m)	f_{LDP} (d < 0.6 m)	N_{Li} (total)
$50 - 100$	< 4.4	0.17	< 26
$100 - 200$	< 5.4	0.14	< 39
$200 - 300$	< 17	0.36	< 47
$300 - 400$	< 43	0.69	< 62
$400 - 500$	156 ± 76	0.82	190 ± 93
$500 - 600$	194 ± 32	0.83	234 ± 39
> 600			616 ± 44
Total			1040^{+143}_{-110}

included to take into account the resolution of the vertex position of the prompt signal: $\sigma_{^9\mathrm{Li}}$, and reconstructed muon track (σ_μ). The best fit values are $\lambda_{^9\mathrm{Li}} = 42 \pm 4$ cm and $\sigma_\mu = 15 \pm 4$ cm. The resolution of prompt signal is fixed in the fit to be 10 cm.

The inefficiency due to the distance cut is corrected by using the energy-specific LDP. The total number of the cosmogenic background is obtained as a sum of ^{9}Li events for all muon energies. The distance cut is changed between 0.5 m to 1.0 m to evaluate the systematic uncertainty. The total cosmogenic background is determined to be $2.20^{+0.35}_{-0.27}$ events per day before the ^{9}Li reduction is applied. The value is determined as an average among the different distance cuts.

MIN method

Lower limit of the cosmogenic background is separately given by the MIN method. In this method, the ^{9}Li enriched sample is selected by the following criteria A or B:

A. If there is more than or equal to one neutron candidates after the muon:

- $E_\mu > 300$ MeV

B. If there is no neutron candidate after the muon:

- $E_\mu > 500$ MeV
- $d < 0.75$ m

Where, neutron candidates are selected as:

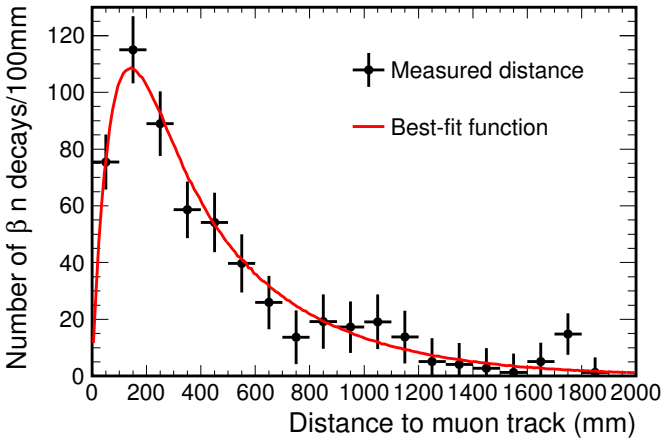

Figure 10.4: Lateral profile of the muon track and the prompt signal of ^{9}Li [37]. The distribution is derived from the samples with more than 600 MeV* muon. Red line is the best fit. The fit function is a convolution of an exponential function and a Gaussian. The Gaussian is included for accounting the resolution of vertex position of the prompt signal and the muon track.

- Within 1 msec after muon
- E_n is between 1.8 and 12.0 MeV.

Figure 10.5 shows the ΔT_μ distribution of the ^{9}Li enriched sample. The background rate in the sample is measured to be 2.05 ± 0.13 events/day.

Combined result of LDP and MIN methods

The cosmogenic background rate is estimated to be $2.08^{+0.41}_{-0.15}$ events/day including systematic uncertainties from a combination of two results, assuming Gaussian distribution of the uncertainties.

Following components are taken into account as the systematic uncertainty of the cosmogenic background.

1. The cut on the distance is varied between 0.5 and 1.0 m. The average value is taken as central value of the LDP rate estimate. Variance (RMS) of 6.5 % is considered as the systematic uncertainty on the rate from LDP method.

2. The average lateral distance λ_{Li} is varied between 39.2 cm and 47.6 cm. As a result, the Li count rate is changed by 0.5 %.

3. Binning of energy spectrum is varied. The rate changed by 0.9 %.

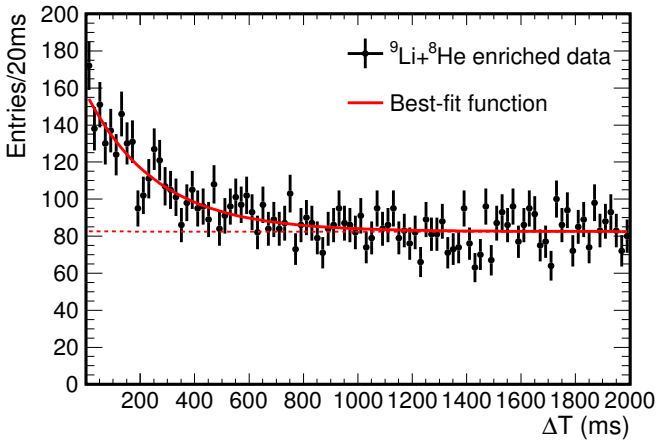

Figure 10.5: ΔT_μ distribution of the ^{9}Li enriched sample collected with the MIN method [37]. Red line shows the best fit with the exponential curve with an offset, which assumes the lifetime as 257 ms. From the fit, the rate is measured to be 2.05 ± 0.13 events/day.

4. The slope of the flat component in the ΔT_μ fit is freed. The variation of the fit result relative to the fixed slope is measured to be 1.3 %.

5. Impact of contribution from the ^{8}He is evaluated. The fraction of ^{8}He is estimated to be 1.5 ± 4.3 % from the measurement by KamLAND [83], then the impact on the rate is evaluated to be -0.2 ± 0.8 %.

10.4.2 ^{9}Li likelihood

^{9}Li likelihood is introduced for reducing the cosmogenic background in the IBD candidates. The ^{9}Li likelihood is calculated from the prompt and delayed event of IBD-like signal, and preceding muon. The distance between the vertex position of the prompt signal and the track of preceding muon is used by the likelihood method. Neutron candidates with energy between 4 and 10 MeV within 1 msec after muon is counted and also used. Instead of ^{9}Li, probability distribution function (PDF) for these two variables are generated by ^{12}B events for reducing statistical uncertainty with Li sample. The distribution using the ^{12}B is confirmed to be similar enough with that from the ^{9}Li. The cut value is calculated for all combinations with previous muons within 700 msec, and the highest likelihood value is taken for the cut.

The likelihood value for the ^{9}Li reduction is determined to be:

$$\mathcal{L}_{^9\mathrm{Li}} < 0.4 \tag{10.5}$$

Number of the ^{9}Li events rejected by the likelihood cut is estimated by a fit to the ΔT_μ

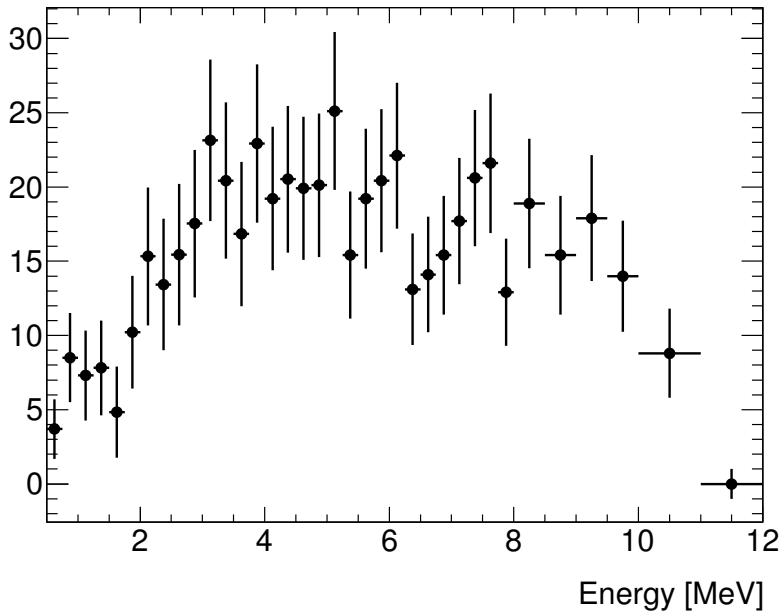

Figure 10.6: Energy spectrum of prompt events of the ^{9}Li candidates. Points show the data with statistical errors.

distribution from the ^{9}Li candidates. The measured value is 1.12 ± 0.05 events/day. Inefficiency of the IBD signal due to the ^{9}Li reduction is estimated to be $0.536 \pm 0.019\%$.

After the ^{9}Li likelihood cut is applied, the estimated rate of the ^{9}Li candidates is $0.98^{+0.41}_{-0.16}$ events/day. Systematic uncertainty is included in the error.

Shape measurement

Spectra shape of the cosmogenic background is estimated from background enriched samples using the ^{9}Li likelihood. The spectrum is obtained by samples which satisfy the following condition:

- Standard IBD selection without ^{9}Li reduction events.
- Select ^{9}Li candidates by applying $\mathcal{L}_{^9\mathrm{Li}} > 0.4$

The energy spectrum is shown in Figure 10.6.

Chapter 11

Measurement of neutrino oscillation

Neutrino oscillation parameter θ_{13} is measured from the neutrino count rate and shape of the measured energy spectrum. By comparing the data with the Monte-Carlo simulation, χ^2 is calculated and the allowed range of θ_{13} is obtained. The comparison is carried out by a multi-dimensional χ^2 test. In this chapter, the statistical analysis of the neutrino oscillation is described.

11.1 Binning

To account for the shape of the energy spectrum, the χ^2 is calculated from energy spectrum divided into 40 bins from 0.5 MeV to 20 MeV. The bin width is 0.25 MeV for low energies below 8 MeV and wider at higher energies, because of lower statistics. The binning configuration is shown in Table 11.1.

Table 11.1: Binning for the energy spectrum of the prompt events. Variable bin width with respect to the visible energy is adopted, because there are less events in the higher energy bins.

Range [MeV]	Bin width [MeV]	Number of bins
0.5 - 8	0.25	30
8 - 10	0.5	4
10 - 12	1	2
12 - 20	2	4

Table 11.2: Number of IBD candidates and prediction in 460.67 live-days.

Source	Number of events
IBD candidates	17351
Reactor neutrino	17530 ± 320
Cosmogenic ^{9}Li/^{8}He	447^{+189}_{-74}
Fast neutron and stopping muon	278 ± 23
Accidentals	32.3 ± 1.2
Total prediction	18290^{+370}_{-330}

Table 11.3: Summary of the uncertainties relative to the signal prediction.

Source	Uncertainty (%)
Reactor flux	1.7
Detection efficiency	0.6
^{9}Li/^{8}He background	$+1.1/-0.4$
Fast neutron and stopping muon	0.1
Statistics	0.8
Total	$+2.3/-2.0$

11.2 Summary of IBD candidates

The number of IBD candidates and the predicted number taken in live-days of 460.67 are summarized in Table 11.2. Also the energy spectrum is shown in Figure 11.1. The number of IBD candidates is 17351, whereas the predicted number of IBD candidates including background (without neutrino oscillation) is 18290^{+370}_{-330}.

Uncertainties relative to the signal prediction are summarized in Table 11.3. The statistical uncertainty is calculated as a square root of the number of predicted IBD candidates. Moreover, systematic uncertainty relative to the signal prediction on the energy scale is estimated using the data. The estimated value is 0.046%. Thus, uncertainty on the energy scale does not affect the number of the IBD events. However, the systematic uncertainty on energy scale affects shape of the spectrum of the IBD candidates. It has an impact to the measurement of the neutrino mixing angle (the impact is estimated in subsection 11.5.1).

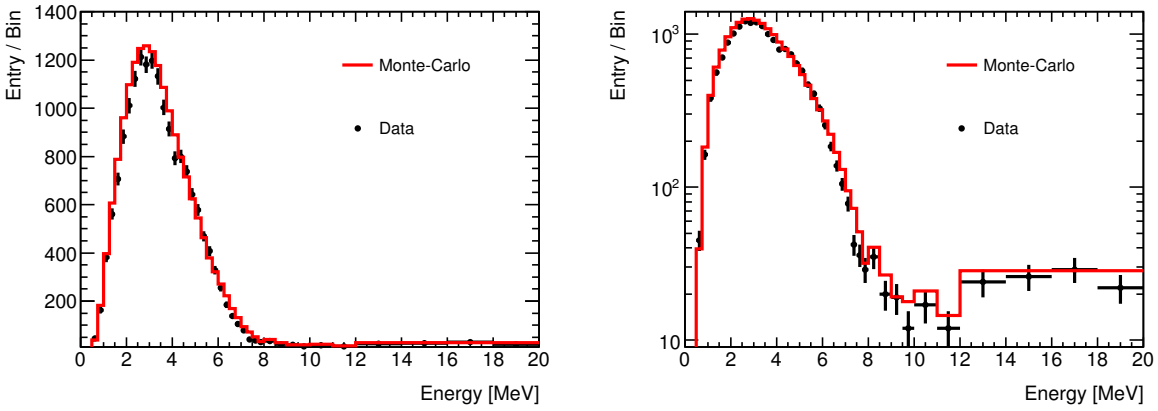

Figure 11.1: IBD spectrum for both the Monte-Carlo and the data. Left figure shows with linear scale, and right figure shows with log scale. Black points show the energy spectrum of the prompt events in the IBD candidates. Red line shows the spectrum by the Monte-Carlo simulation including the backgrounds. Non oscillation is assumed in the Monte-Carlo simulation.

11.3 χ^2 definition

The χ^2 is defined as follows:

$$\begin{aligned}\chi^2 &= \sum_{i=1}^{N_{\rm bins}}\sum_{j=1}^{N_{\rm bins}} \left(N_i^{\rm obs} - N_i^{\rm exp}\right) M_{ij}^{-1} \left(N_j^{\rm obs} - N_j^{\rm exp}\right) \\ &+ \frac{\left(\alpha_{\rm Li+He}-1\right)^2}{\left(\sigma^2_{\rm Li+He}\right)^2} + \frac{\left(\alpha_{\rm acc}-1\right)^2}{\left(\sigma_{\rm acc}\right)^2} + \frac{\left(\alpha_{\rm FN+SM}-1\right)^2}{\left(\sigma_{\rm FN+SM}\right)^2} \end{aligned} \tag{11.1}$$

where, $N_i^{\rm obs}$ and $N_i^{\rm exp}$ are the observed and expected number of IBD candidates (including estimated backgrounds) in the i-th energy bin, respectively. The expected number of IBD candidates is a function of θ_{13} as it is written by the formula below from the equation (2.13):

$$N_i^{\bar{\nu}_{\rm e}}\left(\theta_{13}\right) = N_i^{\bar{\nu}_{\rm e}}\left(\theta_{13}=0\right)\left[1-\sin^2 2\theta_{13}\sin^2\left(\frac{1.267\Delta^2 mL}{E}\right)\right] \tag{11.2}$$

Here, value of the mass difference $\Delta m^2 = 2.44^{+0.09}_{-0.10}\times 10^{-3}$ eV^2 is taken from the result of the MINOS experiment [84].

M_{ij} is a covariance matrix which represents statistical and systematic uncertainties for each bin as well as the bin-to-bin correlation. The matrix consists of several matrices which account for different sources of uncertainties (e.g. statistical uncertainties of IBD candidates, efficiency, and backgrounds). Detail of each matrix is explained in section 11.4.

The expected spectrum is created based on the Monte-Carlo simulation, with different values of θ_{13}. Also background rates are included in $N^{\bar{\nu}_e}$ with corrections optimized in the fit. Therefore the expected rate can be considered as a function of the parameters of θ_{13} and the correction factors.

$$\begin{aligned} N_i^{\rm exp} &= N_i^{\bar{\nu}_e}\left(\theta_{13}, \Delta m^2, a\right) \\ &+ N_i^{\rm Li+He}\left(\alpha_{\rm Li+He}\right) + N_i^{\rm FN+SM}\left(\alpha_{\rm FN+SM}\right) + N_i^{\rm acc}\left(\alpha_{\rm acc}\right) \\ &= f_i\left(\theta_{13}, \alpha_{\rm Li+He}, \alpha_{\rm acc}, \alpha_{\rm FN+SM}\right) \end{aligned} \tag{11.3}$$

where, a represents energy scale. Accordingly, also the χ^2 can be a function of these parameters as well. The θ_{13} is measured by varying each parameter to minimize the χ^2. In the analysis, rates of cosmogenic background, correlated background, and accidental background are allowed to float within their systematic errors. "Pull terms" are added to restrict the quantity of change which account for the systematic errors of the fluctuation. All terms besides the first term in Eq. 11.1 are pull terms.

11.4 Covariance matrix

The total covariance matrix M_{ij} is a sum of covariance matrices from different sources. Since the number of predicted events changes with the fit parameters such as $\sin^2 2\theta_{13}$, it is weighted for every combination of the parameters. In the analysis, statistical uncertainties of IBD candidates flux, efficiency, spectrum shape of ^{9}Li/^{8}He background, statistical uncertainty of accidental background, and uncertainty on energy scale is taken into account by the covariance matrix. Therefore, the total matrix M_{ij} is represented by following equation:

$$M_{ij} = M_{ij}^{\rm stat} + M_{ij}^{\rm flux} + M_{ij}^{\rm eff} + M_{ij}^{\rm Li/He(shape)} + M_{ij}^{\rm acc(stat)} + M_{ij}^{\rm E}. \tag{11.4}$$

$M_{ij}^{\rm stat}$ represents statistical error, which is calculated from the number of IBD candidates including backgrounds estimation. There is no bin-to-bin correlation, therefore the matrix is diagonal. It is denoted as:

$$M_{ij}^{\rm stat} = \delta_{ij}\sqrt{N_i^{\rm pred} N_j^{\rm pred}}. \tag{11.5}$$

Also statistical error of accidental background $M_{ij}^{\rm acc(stat)}$ has no bin-to-bin correlation. Thus, the covariance matrix is diagonal, which is given below:

$$M_{ij}^{\rm acc(stat)} = \delta_{ij}\sqrt{N_i^{\rm acc} N_j^{\rm acc}}. \tag{11.6}$$

$M_{ij}^{\rm flux}$ is an error matrix of the reactor $\bar{\nu}_e$ flux prediction. It is predicted using Monte-Carlo simulation taking the bin-to-bin correlations into account, which is described in section

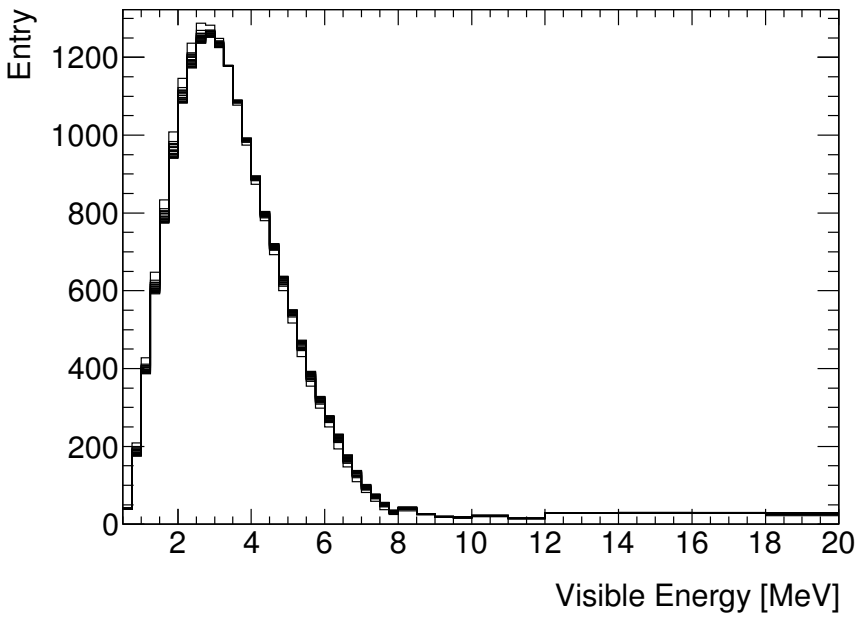

Figure 11.2: Histograms of the number of IBD candidates for each energy bin. Each histogram has different energy scale with a spread of 0.74%.

7.5. $M_{ij}^{\rm eff}$ is the efficiency covariance matrix, which is denoted by the number of neutrino events (without backgrounds):

$$M_{ij}^{\rm eff} = \sigma_{\rm eff}^2 N_i^{\rm exp} N_j^{\rm exp}. \tag{11.7}$$

Here, the uncertainty on the IBD detection efficiency $\sigma_{\rm eff}$ is measured to be 0.6 % (chapter 9). The normalization due to the neutron detection inefficiency, FV veto and IV veto inefficiencies, ^{9}Li likelihood, and number of proton uncertainties are included in the matrix. $M_{ij}^{\rm Li/He(shape)}$ represents the uncertainty on the shape of the cosmogenic background energy spectrum. The uncertainty is explained in section 10.4. Since the rate is included as a pull term in the definition of χ^2, only the shape part is included in the matrix. The mathematical method to decompose the shape part from the total matrix is explained in section 11.4.1. Finally, $M_{ij}^{\rm E}$ is an energy covariance matrix which accounts for the uncertainty on energy scale. The covariance matrix is calculated by spectra with containing energy scale variance like:

$$E' = (1 + a) \times E \tag{11.8}$$

where, a is assumed to follow a Gaussian distribution with mean of zero, and spread of 0.74%. Figure 11.2 shows the histograms of the number of IBD candidates for each energy bin overlaid the different energy scales. The element (i, j) of the covariance matrix is calculated by equation: $E[(X_i - \mu_i)(X_j - \mu_j)]$, where X_i is i-th bin of the histograms, and μ_i is the mean value of the i-th bin.

Covariance matrices are expressed as 2D histograms in figure 11.3.

11.4.1 Decomposition of shape part from a covariance matrix

A covariance matrix M_{ij} can be decomposed into normalization, shape, and "mixed" part [85, 86].

$$M_{ij}^{\rm norm} = \frac{N_i N_j}{N_T^2} \sum_k^n \sum_l^n M_{kl} \tag{11.9}$$

$$M_{ij}^{shape} = M_{ij} - \frac{N_k}{N_T} \sum_j^n M_{ik} - \frac{N_i}{N_T} \sum_k^n M_{kj} + \frac{N_i N_j}{N_T^2} \sum_k^n \sum_l^n M_{kl} \tag{11.10}$$

$$M_{ij}^{mixed} = \frac{N_i}{N_T} \sum_k^n M_{ik} + \frac{N_i}{N_T} \sum_k^n M_{kj} - 2\frac{N_i N_j}{N_T^2} \sum_k^n \sum_l^n M_{kl} \tag{11.11}$$

In these equations, N_i is the predicted number of events in the i-th bin. N_T is total number of events: $N_T = \sum_i N_i$.

For example, as it is explained, only the shape part is included as the covariance matrix in case of the ^{9}Li and ^{8}He background uncertainty, whereas the rate part is included as the pull term in the analysis. In this case, the matrix: $M^{\rm shape} + M^{\rm mixed}$ is used as the shape part (covariance matrix part in the χ^2 definition). It allows to move the rate part to the pull term, and the best fit is extracted from the fit.

11.5 Results

The minimization of χ^2 is performed with respect to $\sin^2 2\theta_{13}$, and pull terms using function minimization tool MINUIT [87]. The energy spectra for the data and Monte-Carlo prediction is shown in Figure 11.4.

The measured value of $\sin^2 2\theta_{13}$ is:

$$\sin^2 2\theta_{13} = 0.105 \pm 0.030. \tag{11.12}$$

where, the minimum χ^2 is calculated to be:

$$\chi^2_{\rm min}/d.o.f. = 50.35/40. \tag{11.13}$$

The error is given by the range where $\chi^2 - \chi^2_{\rm min} < 1.0$. Also, the best fit values for the neutrino oscillation parameter as well as the pull parameters: $\alpha_{\rm Li+He}$, $\alpha_{\rm acc}$, and $\alpha_{\rm FN+SM}$ are summarized in Table 11.4.

Figure 11.5 shows the ratio of the data, after the background is subtracted, to the Monte-Carlo simulation with no oscillation. Also, the ratio of the Monte-Carlo simulation with the best fit values to the Monte-Carlo simulation with no oscillation is shown. From

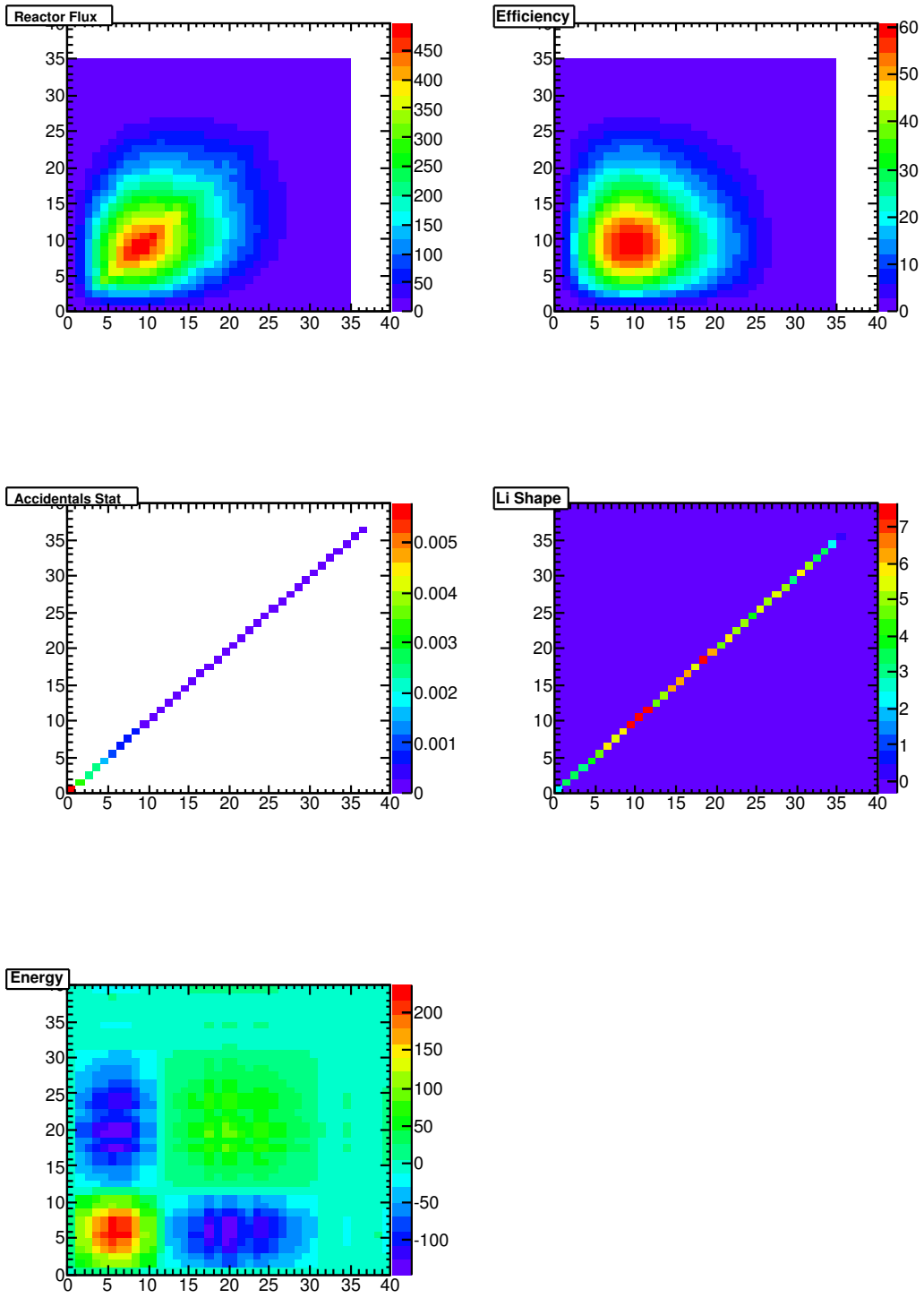

Figure 11.3: Covariance matrices expressed as 2D histograms. Each bin is the matrix element, and the color shows the value.

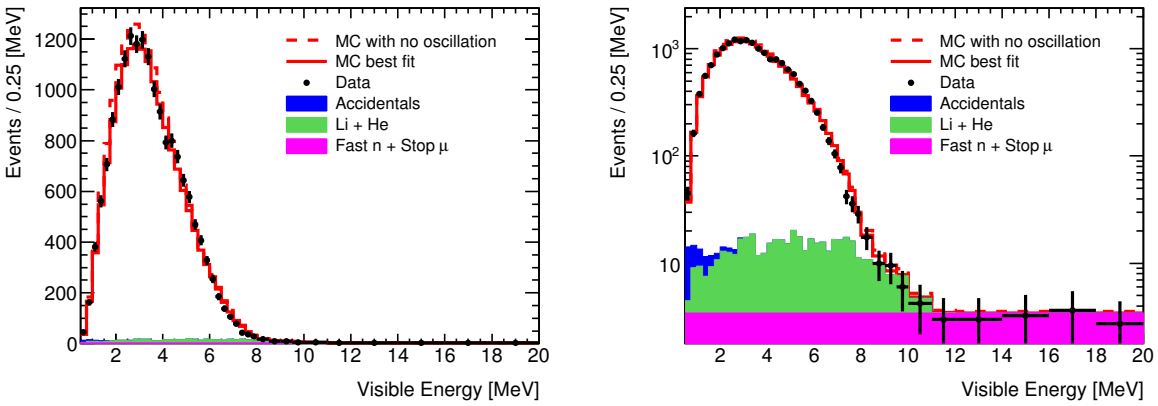

Figure 11.4: The energy spectrum of the prompt events. Left figure is linear scale, and right figure is log scale. The black points are the data, and red lines are Monte-Carlo including background prediction. The red dashed line has no oscillation assumed, and red solid line is the best fit. Background including the cosmogenic, fast neutron and stopping muon, and accidentals is shown with the slant-hatched histogram.

Table 11.4: Result of the oscillation fit.

Fit parameter	Input value	Best fit value
$\sin^2 2\theta_{13}$		0.105 ± 0.030
Li + He bkg.	$0.97^{+0.41}_{-0.16}$	0.79 ± 0.12
Fast-n + stop-μ bkg.	0.604 ± 0.051	0.58 ± 0.044
Accidental bkg.	0.0701 ± 0.0026	0.0701 ± 0.0026

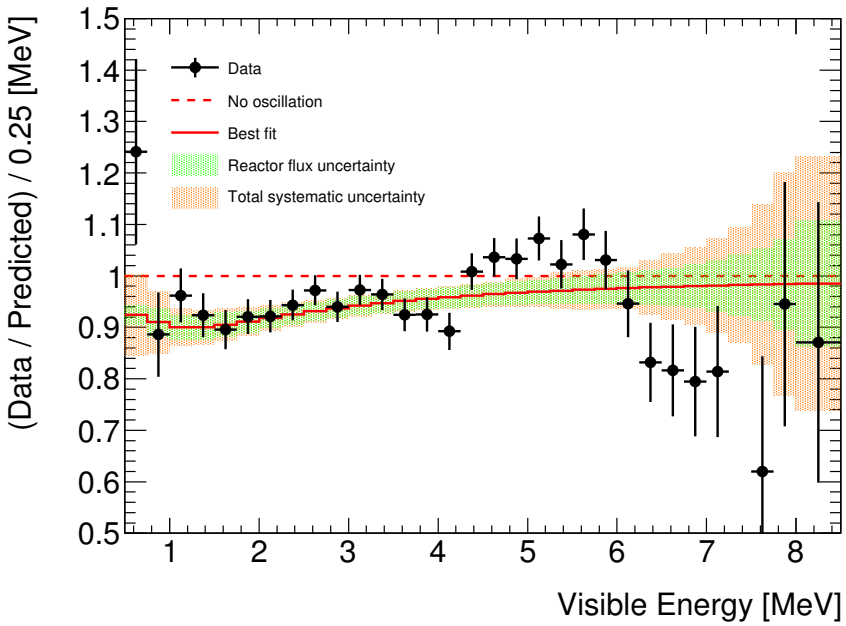

Figure 11.5: Black points show ratio of IBD candidates of the data to Monte-Carlo with no oscillation (background is subtracted from the data). The error bars show the statistical error. Red line shows the ratio of IBD candidates of the Monte-Carlo best fit to the Monte-Carlo with no oscillation. Systematic uncertainty on reactor flux as well as total systematic uncertainty are shown with the colored regions (green and orange, respectively).

the figure, the data and Monte-Carlo with the best fit values agree well in the region where the visible energy is less than 4 MeV. However, there is a bump in the visible energy is between 5 to 7 MeV. The trend can be confirmed from the past publications [6, 38, 88]. However, those measurements were not precise enough to assert the existence of the bump. The same bump between 5 and 7 MeV is reported later by other reactor neutrino experiments, RENO and Daya Bay.

A likely cause of the bump is the reactor flux prediction. The supportive observation is correlation between the excess and the reactor power (Figure 11.6). This plot indicates that any extra background hypothesis is not favored because the background rate should be independent of the reactor power.

11.5.1 Impact of the energy calibration

Impact of the energy calibration to the sensitivity to $\sin^2 2\theta_{13}$ has been evaluated using the Monte-Carlo. The evaluation has been carried out by calculating the sensitivity with different systematic errors on the energy scale. The energy covariance matrix M^{E}_{ij} has

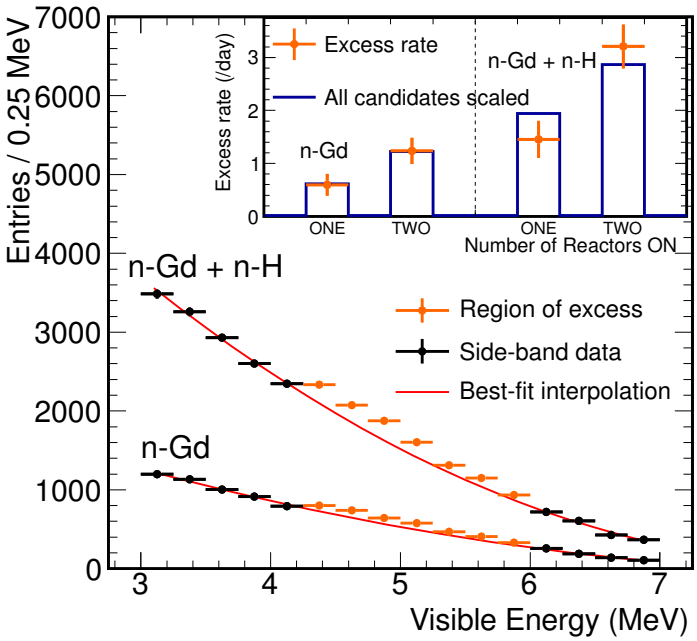

Figure 11.6: Energy spectrum of the prompt events [37]. In the plot, events with neutrons captured on gadolinium nuclei, and also neutrons captured on both gadolinium and hydrogen nuclei are shown. The best-fit interpolation shown with the red curve is a second order polynominal function that fits the data on side the bump region. The inserted figure shows the correlation between the reactor power and rate of excess. The excess is the difference of the data and interpolation in the bump region where the visible energy is between 4MeV and 6MeV. The excess rate was compared between periods when only one reactor was running and when two reactors was running.

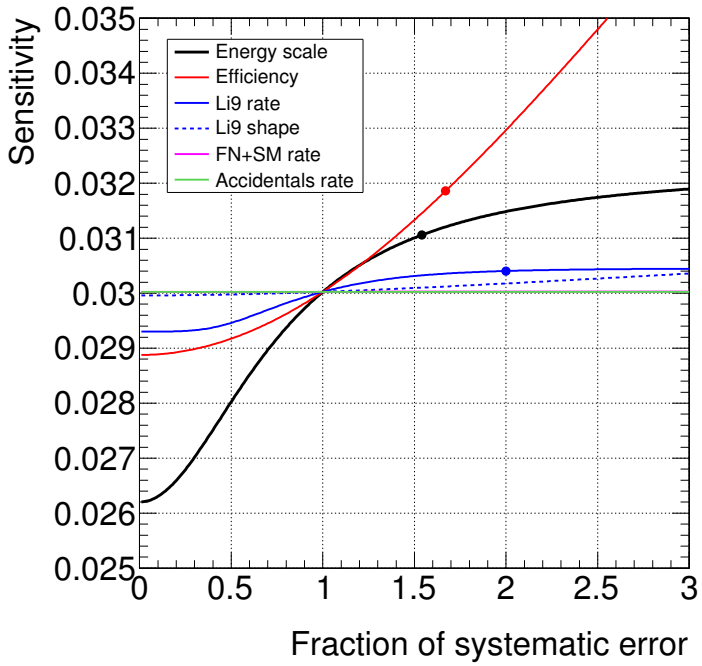

Figure 11.7: Sensitivity to $\sin^2 2\theta_{13}$ with with respect to different systematic uncertainties calculated with the Monte-Carlo. X-axis is the fraction of systematic uncertainties to the obtained. Y-axis is the sensitivity to $\sin^2 2\theta_{13}$. The systematic sensitivities of the past Double Chooz publication in 2012 [6] is shown with Points.

been re-generated with those energy scales. Figure 11.7 shows the sensitivity to $\sin^2 2\theta_{13}$ with respect to fraction of systematic uncertainties. The systematic uncertainty on the energy scale in the Double Chooz result [6] published in 2012 was 1.14 % which led to the $\sin^2 2\theta_{13}$ sensitivity of 0.031.

Furthermore, impact of the linearized-PE calibration is evaluated. In section 6.3.1, neutron capture peaks on hydrogen nuclei and gadolinium nuclei were compared with and without the linearized-PE calibration. The ratios of the neutron capture on gadolinium nuclei peak to the hydrogen nuclei peak were evaluated. From the result, it is expected that about 2.1% of the discrepancy is introduced at 8 MeV if the linearized-PE calibration is not applied (Since the absolute energy calibration uses neutron capture on hydrogen nuclei peak, so we assume there is no discrepancy at 2.2 MeV). To evaluate effect of the linearized-PE calibration to $\sin^2 2\theta_{13}$, the value is calculated by using the Monte-Carlo, and imposing the energy non-linearity as:

$$\frac{E'}{E} = \pm\frac{0.021}{8.0 - 2.2}(E - 2.2) + 1.0 \tag{11.14}$$

where, E' is the energy after the extra non-linearity is imposed, and E is the visible energy. From the analysis, additional systematic uncertainty to $\sin^2 2\theta_{13}$ introduced by the non-linearity is estimated to be 0.017. It is sizable comparing with the total uncertainty of 0.030. Thus, correction of the energy non-linearity is essential for the precise measurement of θ_{13}.

Chapter 12

Conclusion

The aim of Double Chooz experiment is to precisely measure the neutrino mixing angle θ_{13}. It had been unknown for long whether the θ_{13} has non-zero value, or not.

The precise measurement of the neutrino mixing angles has great importance for the future neutrino experiments such as measuring the CP violation in the lepton sector, and mass hierarchy.

Double Chooz first indicated the existence of the non-zero θ_{13} value, which was in 2012 [28]. After the publication, not only statistics, but also improvements. On the analysis, for example, energy calibration, background subtraction, and neutrino selection have been accomplished. As the deficit of reactor neutrinos due to neutrino oscillation is energy dependent, energy calibration and evaluation of the systematic uncertainties are essential in the precision measurement of the mixing angle. From the measurement of neutron capture on hydrogen and gadolinium peaks, the discrepancy of the ratio of the peaks to the truth value was 2.4 %, without the new calibration, while it was improved to be 0.28 % by the linearized-PE calibration.

Using only the far detector, for 460.67 days of live time, the neutrino mixing angle θ_{13} was measured to be $\sin^2 2\theta_{13} = 0.105 \pm 0.030$.

The near detector construction was finally finished in November 2014. The reactor flux uncertainty is expected to be reduced significantly. Double Chooz continues to take the data, and aims for further improvement of the measurement precision with the near detector.

Appendix A

Gain estimation from number of photoelectrons

The calculation method of a PMT gain is described here. Data for the gain estimation is taken by using the IDLI system which injects constant number of photons into the detector. Charge distribution for each readout channel is used for the gain estimation.

The gain is denoted by k, as defined by the following equation:

$$\mu = kN, \tag{A.1}$$

where μ is mean of charge distribution, and N is the number of photoelectrons. Gain k can be interpreted as a conversion factor of the number of photoelectrons to charge.

Variance σ^2 (or standard deviation σ) of the charge distribution is expressed as a sum of variances related to different sources of the spread:

$$\sigma^2 = \sigma^2_{\text{poisson}} + \sigma^2_{\text{spe}}, \tag{A.2}$$

where, σ_{poisson} is fluctuation due to number of photoelectrons in the PMT. It is considered to follow the Poisson distribution. σ_{spe} is a variance of charge due to resolution of each PMT which is assumed to follow the normal distribution. Therefore, $\sigma^2_{\text{poisson}}$ and σ^2_{spe} are written as:

$$\sigma^2_{\text{poisson}} = k^2 N, \tag{A.3}$$

and

$$\sigma^2_{\text{spe}} = a^2 k^2 N, \tag{A.4}$$

respectively. Where a is a constant which indicates the standard deviation of the entire single photoelectron distribution. Therefore, σ^2 is expressed by:

$$\sigma^2 = k^2 N \left(1 + a^2\right). \tag{A.5}$$

From the equations above, the gain k can be expressed by the formula below:

$$k = \frac{1}{(1+a^2)}\frac{\sigma^2}{\mu} \tag{A.6}$$

a is determined by the PMT multiplicity by assuming all PMTs have same value, as it is described in section 6.3.

Appendix B

Poisson corrected multiplicity

We consider a situation that n_{PE} of photoelectrons are observed by n_{PMT} of PMTs. For a PMT, probability to count zero photoelectrons is approximated by:

$$P(X = 0) = \frac{\lambda^0 e^{-\lambda}}{0!} = e^{-\lambda}, \tag{B.1}$$

where

$$\lambda = \frac{n_{\mathrm{PE}}}{n_{\mathrm{PMT}}}. \tag{B.2}$$

Hence, probability to count at least one photoelectrons is:

$$P(X \neq 0) = 1 - e^{-\lambda}. \tag{B.3}$$

Therefore, number of PMT hits is by n_{PMT} of PMTs is:

$$n_{\mathrm{hit}} = n_{\mathrm{PMT}} \times (1 - e^{-\lambda}). \tag{B.4}$$

The equation becomes:

$$-\lambda = \ln\left(1 - \frac{n_{\mathrm{hit}}}{n_{\mathrm{PMT}}}\right). \tag{B.5}$$

Finally, the equation:

$$n_{\mathrm{PE}} = -n_{\mathrm{PMT}} \ln\left(1 - \frac{n_{\mathrm{hit}}}{n_{\mathrm{PMT}}}\right) \tag{B.6}$$

is derived.

Acknowledgements

I would like to express my gratitude to everyone who gave me helps during my Ph.D course. Without the supports, it was not possible to accomplish my graduation.

First of all, I would like to appreciate to my supervisor, Prof. Masahiro Kuze. He guided me to study physics and gave me advices from many aspects. Also, I would like to thank for supporting my life at his group in a good atmosphere. It was lucky that I could study in his group for six years since I was a bachelor student. Next, I would like to appreciate to Dr. Masaki Ishitsuka, research associate in Kuze group. His ideas and suggestions in research always helped me. Not only physics, but also I was helped by his kind advices about my life and future.

During my Ph.D course, I could study at APC laboratory in Paris for ten months. I would like to express my appreciation to Dr. Anatael Cabrera. He recommended me to apply the Eiffel Excellence Scholarship Programme, and kindly accepted me to study at APC laboratory. He guided me the research, and kindly supported my life in France. The time that I studied in Paris was a great experience in my life. Also, I would like to appreciate to people in APC for many supports. Prof. Michel Obolensky was always helpful for teaching me about life at APC laboratory. Prof. Herve de Kerret pleasantly supported me to act outside of APC. Thanks to his support, I was possible to succeed the IDLI installation.

Next, I would like to appreciate people in Double Chooz Japan. Advices from Dr. Michiru Kaneda was helpful in my study, and programming. Especially, IDLI installation was a great work during my Ph.D course. I would like to thank people who worked together in Chooz. Dr. Emmanuel Chauveau was leading the installation work of the near detector, and supported me for the IDLI installation. Ms. Ralitsa Sharankova, was very helpful for the IDLI installation. It was a fun to spend life in Chooz village. Also, I would like to appreciate to Dr. Histaka Furuta for many supports during the installation.

And, I would like to appreciate Prof. Jeff Hartnell. I stayed at the Sussex University before the IDLI installation to learn about the procedure of the installation. He pleasantly taught me about the IDLI system, and took care of the installation work.

Also, I would like to thank everyone in Kuze group. Especially, it was fun to spend time with Mr. Takuya Nobe, as a friend from beginning of a life at Kuze group. Also, I would like to thank all my friends who encouraged me to study physics in Tokyo Tech.

And finally, I would like to thank my parents for always understanding and encouraging me as the best supporters of mine.

This work was financially supported from the Global Center of Excellence Program by MEXT, Japan through the "Nanoscience and Quantum Physics" Project of the Tokyo Institute of Technology, and the Eiffel Excellence Scholarship Programme by the French Ministry of Foreign Affairs and International Development.

Bibliography

[1] W. Pauli, "Dear radioactive ladies and gentlemen", Phys. Today, vol. 31N9, p. 27, 1978.

[2] C. L. Cowan Jr., F. Reines, F. B. Harrison, H. W. Kruse, and A. D.McGuire, "Detection of the Free Neutrino: a Confirmation", Science, 20 July 1956: 103-104.

[3] G. T. Danby et al., "Observation of high-energy neutrino reactions and the existence of two kinds of neutrinos", Phys. Rev. Lett. 9 (1962) 36.

[4] K. Kodama, et. al., (DONUT Collaboration), "Observation of tau neutrino interactions", Phys. Lett. B 504:218-224, 2001.

[5] ALEPH Collaboration, "Determination of the number of light neutrino species", Phys. Lett. B, vol 231, no. 4, pp. 519-529, 1989.

[6] Double Chooz collaboration, "Reactor $\bar{\nu}_e$ disappearance in the Double Chooz experiment", Phys. Rev. D 86, 052008, (2012).

[7] Z. Maki, M. Nakagawa, and S. Sakata, "Remarks on the Unified Model of Elementary Particles", Prog. Theo. Phys. 28: 870, 1962.

[8] K.A. Olive et al. (Particle Data Group), Chin. Phys. C, 38, 090001 (2014).

[9] R. Davis, et al., "Search for neutrinos from the sun", Phys. Rev. Lett. 20:1205-1209, 1968.

[10] Y. Fukuda et al., (Super-Kamiokande), "Evidence for Oscillation of Atmospheric Neutrinos", Phys. Rev. Lett. 81 (1998) 1562-1567.

[11] John N. Bahcall, Solar models: An historical overview, Nuclear Physics B - Proceedings Supplements, 118 (0): 77 - 86, 2003, Proceedings of the XXth International Conference on Neutrino Physics and Astrophysics.

[12] J. N. Bahcall, A. M. Serenelli, and S. Basu, "New Solar Opacities, Abundances, Helioseismology, and Neutrino Fluxes", Astrophys. J. 621, L85 (2005).

[13] B. T. Cleverland et al., "Measurement of the Solar Electron Neutrino Flux with the Homestake Chlorine Detector", AstroPhys. J. 495, 505 (1998).

[14] A. I. Abazov, et al., Search for neutrinos from the Sun using the reaction $^{71}\mathrm{Ga}(\nu_{\mathrm{e}}, \mathrm{e}^{-})^{71}\mathrm{Ge}$, Phys. Rev. Lett., 67: 3332 - 3335, 1991.

[15] W. Hampel, et al., GALLEX solar neutrino observations: Results for GALLEX IV. Phys. Lett., B447: 127 - 133, 1999.

[16] M. Altmann, et al., Complete results for five years of GNO solar neutrino observations, Physics Letters B, 616 (34): 174 - 190, 2005.

[17] J. Hosaka et al., Super-Kamiokande Collaboration, "Solar neutrino measurements in Super-Kamiokande-I", Phys. Rev. D73: 112001 (2006).

[18] Q. R. Ahmad et al., Direct Evidence for Neutrino Flavor Transformation from Neutral-Current Interactions in the Sudbury Neutrino Observatory, Phys. Rev. Lett. 89:011301, (2002).

[19] K. S. Hirata, et al., "Observation of a small atmospheric $\nu_{\mu}/\nu_{\mathrm{e}}$ ratio in Kamiokande", Physics Letters B, 280 (12): 146 - 152, 1992.

[20] G. Giacomelli, A. Margiotta, "Macro results on atmospheric neutrinos", Nucl. Phys. Proc. Suppl., 145: 116 - 119, 2005, hep-ex/0504029.

[21] D. Casper, et al., "Measurement of atmospheric neutrino composition with the IMB-3 detector", Phys. Rev. Lett. 66: 2561 - 2564, 1991.

[22] M. H. Ahn, et al., (K2K Collaboration), Measurement of Neutrino Oscillation by the K2K Experiment, Phys. Rev. D 74, 072003 (2006).

[23] P. Adamson, et al. (MINOS Collaboration), Measurement of the neutrino mass splitting and flavor mixing by MINOS, Phys. Rev. Lett. 106, 181801 (2011).

[24] K. Abe, et al., (T2K Collaboration), Indication of Electron Neutrino Appearance from an Accelerator-Produced Off-Axis Muon Neutrino Beam, Phys. Rev. Lett. 107, 041801 (2011).

[25] M. Apollonio et al., "Search for neutrino oscillations on a long base-line at the CHOOZ nuclear power station", Eur. Phys. J, C27, 331 (2003).

[26] F. P. An et l., (Daya Bay Collaboration), "Observation of Electron-Antineutrino Disappearance at Daya Bay", Phys. Rev. Lett. 108, 171803 (2012).

[27] J. K. Ahn, et al., (RENO Collaboration), "Observation of Reactor Electron Antineutrinos Disappearance in the RENO Experiment", Phys. Rev. Lett. 108, 191802 (2012).

[28] Y. Abe, et al., (Double Chooz Collaboration), "Indication of Reactor $\bar{\nu}_e$ Disappearance in the Double Chooz Experiment", Phys. Rev. Lett. 108, 131801 (2012).

[29] F. P. An, et al., "Spectral Measurement of Electron Antineutrino Oscillation Amplitude and Frequency at Daya Bay", Phys. Rev. Lett. 112, 061801 (2014).

[30] D. Ayres, et. al., "NOvA Proposal to Build a 30 Kiloton Off-Axis Detector to Study Neutrino Oscillations in the Farmilab NuMI Beamline", arXiv:hep-ex/0503053 (2005).

[31] K. Abe, et al., "Letter of Intent: The Hyper-Kamiokande Experiment — Detector Design and Physics Potential —", arXiv: hep-ex/1109.3262, 2011.

[32] H. Sugiyama, "Exploring leptonic CP violation with combined analysis of reactor and neutrino superbeam experiments", arXiv:hep-ph/0411209 (2004).

[33] A. Cucoanes, et al., "", arXiv: hep-ex/1501.00356 (2015).

[34] Y. Abe, et. al., "First Measurement of θ_{13} from Delayed Neutron Capture on Hydrogen in the Double Chooz Experiment", Phys. Lett. B723: 66-70, (2013).

[35] T.J.C. Bezerra, "Improvement of θ_{13} Measurement in the Double Chooz Experiment and the First Effective Δm^2_{31} Measurement from Reactor Neutrino Oscillation at Different Baselines", Ph.D. thesis (2013).

[36] T.J.C. Bezerra, et. al., "A Global Fit Determination of Effective Δm^2_{31}" from Baseline Dependence of Reactor $\bar{\nu}_e$ Disappearance", Phys. Lett. B 725 271-276 (2013).

[37] Double Chooz collaboration, "Improved measurements of the neutrino mixing angle θ_{13} with the Double Chooz detector", JHEP 1410, 86 (2014).

[38] Double Chooz collaboration, "First measurement of θ_{13} from delayed neutron capture on hydrogen in the Double Chooz experiment", Phys. Lett. B 723 (1), 66-70, 2013.

[39] K. Zbiri, "Note on Drexel tests of the IMB R1408 PMTs used in the inner veto of both far and near detectors of the Double Chooz experiment", arXiv:1104.4045 (2011).

[40] C. Aberle, et al., "Large scale Gd-beta-diketonate based organic liquid scintillator production for antineutrino detection", JINST. 7, P06008 (2012).

[41] "Double Chooz: A Search for the Neutrino Mixing Angle θ_{13}", arXiv: hep-ex/0606025, 2006.

[42] Hamamatsu Photonics K.K, LARGE PHOTOCATHODE AREA PHOTOMULTIPLIER TUBES.

[43] R. Abbasi, et al., Nucl. Instru. Meth., A 618 139-152 (2010).

[44] T. Matsubara et al., "Evaluation of 400 low background 10-in. photo-multiplier tubes for the Double Chooz experiment", Nucl. Inst. Meth. A 661, 16 (2012)

[45] R. Abbasi, et al., "Calibration and characterization of the IceCube photomultiplier tube", Nucl. Inst. Meth. A 618 (2010) 139152.

[46] CAEN Corporation, http://www.caen.it/.

[47] Fumitaka Sato et al., Physics Procedia 37 (2012), 1164, 1170.

[48] E. Caden, Double Chooz internal note, DC-doc-2345-v2 (2011).

[49] Y.Abe et al., "The Waveform Digitiser of the Double Chooz Experiment: Performance and Quantization Effects on PhotoMultiplier Tubes Signals", JINST 8 P08015 (2013).

[50] F. Beissel et al., "The Trigger and Timing System of the Double Chooz Experiment", JINST 8 T01003, 2013.

[51] Xilinx Inc. data sheet, "XC2V500 - Virtex-II Platform FPGAs: Complete Data Sheet", http://www.alldatasheet.com/datasheet-pdf/pdf/114255/XILINX/XC2V500.html (2003).

[52] J. Maeda (Double Chooz Collaboration), "Online data acquisition and the control system for the Double Chooz experiment", J. Phys.: Conf. Ser. 331, 022018 (2011).

[53] Lucotte A et al., "A front-end read out chip for the OPERA scintillator tracker", Nucl. Inst. Meth. A 521, 378-392 (2004).

[54] ROOT, http://root.cern.ch/drupal/

[55] MySQL, http://www.mysql.com/

[56] T. Konno et. al., IEEE Nucl. Sci. Symp. Conf.Rec. 622-628 (2009).

[57] P. Novella, et. al., Double Chooz internal note, DC-doc-649-v2 (2009).

[58] Y. Abe, et. al., Double Chooz collaboration, Precision muon reconstruction in Double Chooz, Nucl. Instrum. Meth. A 764 (2014) 330.

[59] P. Wahnon, final year undergraduate project report, University of Sussex (2010).

[60] C. Aberle et al., JINST 6, P11006 (2011).

[61] C. Aberle et al., Chem. Phys. Lett. 516, 257 (2011).

[62] K. Schreckenbach, G. Colvin and F. von Feilitzsch, Phys. Lett. B160, 325 (1985).

[63] F. von Feilitzsch and K. Schreckenbach, Phys. Lett. B118, 162 (1982).

[64] A. Hahn et al., Phys. Lett. B218, 365 (1989).

[65] N. Haag et al., Phys. Rev. Lett. 112, 122501 (2014).

[66] M. Fallot et al., Phys. Rev. C83, 054615, (2011).

[67] P. Huber, Phys. Rev. C 84 024617 (2011).

[68] O. Meplan et al., in ENC 2005: European Nuclear Conference; Nuclear power for the XXIst century: from basic research to high-tech industry (2005).

[69] NEA-1845/01, documentation for MURE (2009).

[70] G. Marleau et al., Report IGE-157 (1994).

[71] C. Jones, "Prediction of the Reactor Antineutrino Flux for the Double Chooz Experiment", Ph.D. thesis, MIT (2012).

[72] C. Jones et al., Phys. Rev. D 86 (2012) 012001.

[73] Y. Declais et al., Phys. Lett. B338, 383 (1994).

[74] P. Vogel and J. F. Beacom, Phys. Rev. D 60, 05003 (1999).

[75] K. Nakamura et. al., (Particle Data Group), The review of particle physics. Journal of Phys. G: 37 (075021), 2010.

[76] D. H. Wilkinson, "Analysis of neutron β-decay", Nucl. Phys. A, 377 (2 - 3): 474 - 504, 1982.

[77] Th. A. Mueller et. al., "Improved predictions of reactor antineutrino spectra", Phys. Rev. C, 83 054615, 2011.

[78] J. Allison et al., IEEE Trans. Nucl. Sci. 53 No. 1, 270 (2006).

[79] S. Agostinelli et al., Nucl. Instrum. Meth. A506, 250 (2003).

[80] J. R. Granada, Phys. Rev. B31, 4167 (1985).

[81] E. J. Axton and A. G. Bardell, Neutron yield from the spontaneous fission of ^{252}Cf($\bar{\nu}$), Metrologia 21 (1985) 59.

[82] TRIPOLI-4 version 8.1, 3D general purpose continuous energy Monte Carlo transport code, NEA-1716/07, http://www.oecd-nea.org/tools/abstract/detail/nea-1716, (2013).

[83] S. Abe, et al., (KamLAND collaboration), "Production of radioactive isotopes through cosmic muon spallation in KamLAND", Phys. Rev. C81 025807 (2010)

[84] P. Adamson, et al., (MINOS Collaboration), "Combined analysis of ν_μ disappearance and $\nu_\mu \rightarrow \nu_e$ appearance in MINOS using accelerator and atmospheric neutrinos", Phys. Rev. Lett. 112 191801 (2014).

[85] A. Franke, Searching for Reactor Antineutrino Flavor Oscillation with the Double Chooz Far Detector, PhD thesis, Columbia University, 2012.

[86] E. Conover, Muon-induced backgrounds in the Double Chooz neutrino oscillation experiment, PhD thesis, Chicago University, 2014.

[87] F. James, M. Roos, Computer Physics Communication 10 (1975) 343.

[88] CHOOZ collaboration, M. Apollonio et al., "Limits on neutrino oscillation from the CHOOZ experiment", Phys. Lett. B 466 (1999) 415.